VORTEX DYNAMICS AND MACHINE LEARNING ON OSCILLATING-FOIL TURBINES

by

Bernardo Luiz Rocha Ribeiro

A dissertation submitted in partial fulfillment of
the requirements for the degree of

Doctor of Philosophy

(Engineering Mechanics)

at the

UNIVERSITY OF WISCONSIN–MADISON

2023

Date of final oral examination: 05/25/2023

The dissertation is approved by the following members of the Final Oral Committee:

Jennifer A. Franck, Assistant Professor, UW–Madison, Mechanical Engineering
Riccardo Bonazza, Professor, UW–Madison, Mechanical Engineering
Wenxiao Pan, Associate Professor, UW–Madison, Mechanical Engineering
Nimish Pujara, Assistant Professor, UW–Madison, Civil & Environmental Engineering
Kenneth S. Breuer, Professor of Engineering, Brown University, College of Engineering

Acknowledgments

I would like to start thanking my family for their invaluable support throughout my Ph.D.. Their support and love since the first day I arrived in Providence, Rhode Island, helped me throughout this 6-year journey. I'm blessed and I feel extremely lucky to have them by my side regardless of the path I choose for my professional career. Thank you for your patience and for all the Zoom meetings we had religiously every week. You made the COVID pandemic much smoother to me when I had to stay at home on my own and if I reach this point of writing my Ph.D. thesis, it was because of you believing in me and pushing me to become the best version of myself.

My advisor, Prof. Jennifer Franck, has become a true mentor not only on research but also helped me grow as a person. There are countless things I would like to thank her for but first and foremost, her patience, guidance and support throughout all 8 years we have been together are things I will take with me wherever I will go after my Ph.D.. Her passion for research and hands-on support with her students made me enjoy the academic career as a whole and it is something I am planning to pursue. There was not a single moment during graduate school that I felt discomfort or insecure on what I had to do and that is because of you being always by my side assisting and giving advice to me on how to solve a particular problem. Lastly, thank you for replying to my email 8 years ago when I was just an undergrad during an international program at UC San Diego looking for a summer internship. I truly believe that single email completely changed my life and everything you taught helped me who I am today. I would like to thank my committee members for all the guidance throughout graduate school, all professors from the courses I have taken at UW-Madison and Brown University, and the support staff at the EP department, especially Dina Christenson, Katherine Wegner and Sara Hladilek, who made sure I never had any problems in terms of administration and academic aspects of my degree.

I am honored to have the best research group that any graduate student could ask for. I would like to give special thanks to Mukul Dave, who stayed with me since we were at Brown University before moving to UW-Madison. Your help not only with research but on whatever and whenever I needed made my Ph.D. journey much easier to handle. Kate Lyons, thank you for your support and for bringing so much energy to our group. Your drive towards our research brought even more light to our office space. Thank you for the current graduate students in our lab, Trevor Dunt, Sara Hartke, Soundarya Ramasubramanian, and Rithwik Kandukuri. Thank you for all the research and non-research related conversations we have in our office, the ideas you all had to decorate our office, your patience, and for the daily walks to Union South to get my "hot 2% medium latte". I will deeply miss you all.

Thank you to all my research collaborators and co-authors of my journal papers, especially Professor Kenny Breuer and his students Yunxing Su, Eric Handy-Cardenas, Howon Lee, and Yuanhang Zhu, for all the research discussions and ideas so I could make progress during graduate school. Thank you to the past members of our lab that were part or assisted the oscillating-foil turbine project, Sarah Frank, Isabel Scherl, Filip Simeski, Alejandro Calvet, David Burkhart. Thank you to the ORCA team that was established with colleagues at Brown University and Blusource Energy that introduced me to the project.

I am also grateful to have amazing friends outside the fluid mechanics field and want to thank everyone who is part of the Engineering Physics & Mechanics - Graduate Student Organization (EPM-GSO). Thank you for all the socials we had throughout the years and for the necessary breaks during research. Lastly, I acknowledge the award No. CBET-1921594 from the National Science Foundation, the award DE-AR0000318 from ARPA-E, and the Wisconsin Distinguished Graduate Fellowship (WDGF), for funding my Ph.D. research.

Abstract

Oscillating foils in a combined heave/pitch motion are an effective way to extract hydrokinetic energy and offer benefits of shallow water operation, scalability, and low cut-in speeds. In a flapping-foil turbine, power generation is a function of the foil kinematics, namely operating foil frequency, heave, and pitch amplitude. The efficiency and kinematics of a single foil in freestream conditions are well understood both numerically and experimentally, however foils in coordinated array configurations have not received as much attention. As observed in other wind and hydrokinetic turbines, the downstream foils of arrays suffer from reduced freestream velocity and wake disturbances. Thus, a major challenge within the industry is to accurately predict and model how the wake of one turbine affects the others downstream. Progress has been made in wind farm layouts, however due to the oscillatory, rather than rotational, kinematics the wake structure of oscillating foils is vastly different from that of traditional horizontal-axis turbines.

This thesis first revisits single-foil turbines and analyze the Reynolds number effects on the energy harvesting. It is found that comparing data between $Re = 50,000$ and $Re = 1000$, the high Reynolds number flows demonstrated a moderate 0.8 - 6.7% increase in power compared to the low Reynolds number flow.

Using data from experiments and simulations, an in-depth wake analysis is performed and the mean velocity and the turbulent kinetic energy are quantified in the wake. With the mean wake velocity, a predictive wake model is able to distinguish three regimes through analyzing trailing foil efficiency profiles. Using machine learning algorithms, further investigation is made on the wake from those three regimes of foil kinematics and wake patterns are distinguished with respect to the foil parameters.

Lastly, a power prediction model is developed based on the effects of vortex-foil interactions in two-foil arrays and can be used to predict array performance at different configurations only using single-foil data.

Contents

1 Introduction

1.1 Motivation

Wave and tidal energy are estimated to hold 1420 TWh/yr of extractable energy in the United States, about a third of the 4000 TWh/yr of energy that is used in the country [1]. Although this rich source of clean and renewable energy has a potential of generating power for remote communities where solar or wind energy is not feasible, there exist many engineering challenges in terms of the successful operation and maintenance of hydrokinetic turbines. Many devices designed for tidal energy extraction are in the form of rotational turbines, such as axial-flow and cross-flow devices [2], or in the form of oscillatory turbines.

Among the classes of hydrokinetic energy technologies, axial-flow turbines are the most common ones [3], whose rotational axis is parallel to the flow, as displayed in Figure 1.1a. The highlighted axial-flow turbine corresponds to one of the iterations developed by Verdant Power, known as the first company to commercially license arrays of tidal turbines in the world [3]. For cross-flow turbines, as the name suggests, the axis of rotation is perpendicular to the flow (Figure 1.1b), and currently the Ocean Renewable Power Company is the most active cross-flow turbine producer in the United States [3]. Finally, the oscillating-flow turbine is where the flow passes through the device's oscillatory motion, typically governed by flapping foils, as shown in a prototype developed by researchers at Brown University (Figure 1.1c) [4].

Comparing the oscillatory-flow turbines with the rotational turbines, the former offers many advantages over the latter, such as avoiding the high tip speeds that scale with radius on rotating blades. The design of oscillating-foil turbines can also fit in shallower waters than their rotating counterparts, and have the potential to be closely packed due to their simple geometry and more coherent wake structure [5]. These can be explained

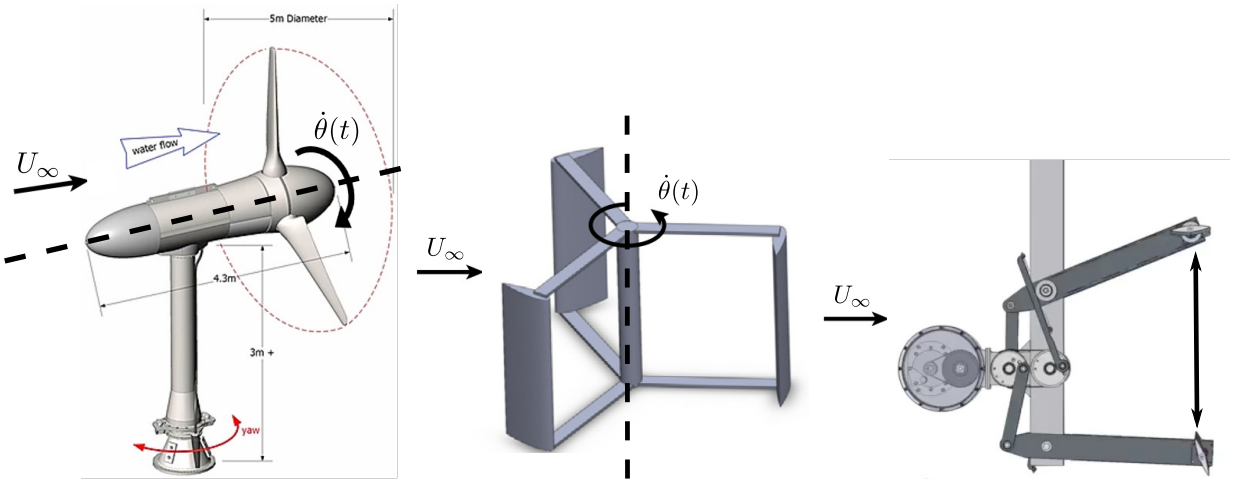

(a) Axial-flow (b) Cross-flow (c) Oscillatory-flow

Figure 1.1: Classification of hydrokinetic energy technologies. The freestream flow is given by U_∞ and rotational axis is highlighted in a dashed line and the blade's pitch velocity, $\dot{\theta}(t)$.

by observing the turbine's swept area between axial-flow and oscillating-foil turbines as displayed in Figure 1.2. The foil's swept area not only covers a larger area compared to axial-flow turbines but is also easily scalable in width since its tip speed is independent of foil's width.

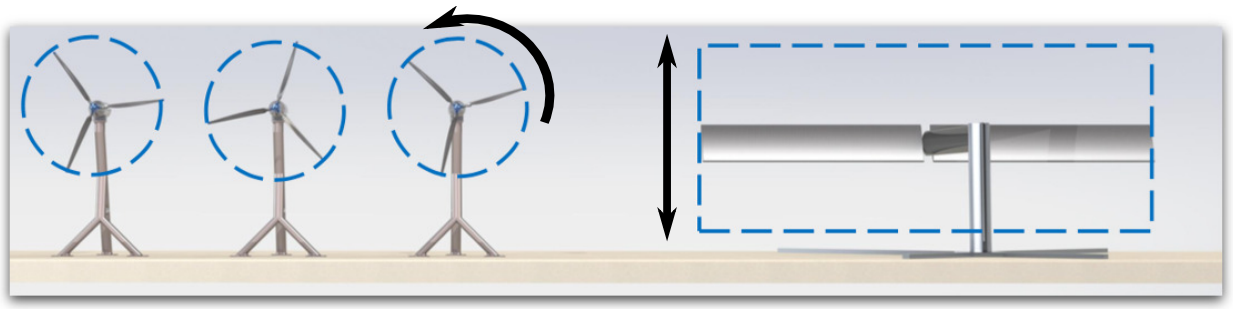

Figure 1.2: Comparison of swept areas between axial-flow and oscillatory-flow turbines.

1.2 Power Generation on a Single Oscillating-Foil Turbine

Another benefit is that the power generation on an oscillating-foil turbine is largely based on the kinematics of the foil. Thus a single foil can very easily be optimized for power output over various flow speeds by modulating the kinematics without changing the size

or overall design of the foil. The kinematic motion with respect to the freestream flow is summarized in Figure 1.3, with $h(t)$ denoting the heave position, $\theta(t)$ the pitch angle and the three foil parameters, frequency of oscillation, f, non-dimensionalized by the chord length c and freestream velocity U_∞, heave amplitude, h_o, and pitch amplitude, θ_o. To generate power during the upstroke, a foil heaves vertically with a positive angle of attack to produce a net positive lifting force and positive power. It then repeats the symmetric stoke on the downstroke, with a pitch reversal at the top and bottom of the stroke. The parameter Y_p corresponds to the foil's swept area and it defines the window of oncoming energy from the freestream flow.

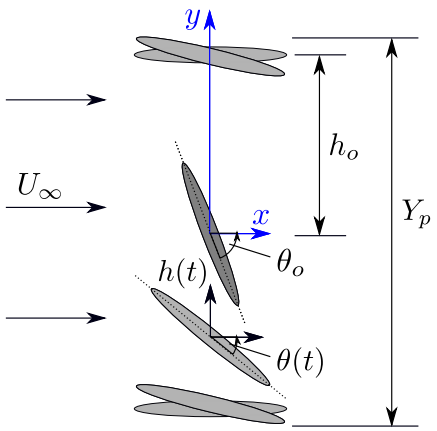

Figure 1.3: Kinematics of the elliptical hydrofoil's motion shown for the upstroke.

The first modern mention of oscillating foils for energy harvesting applications was by McKinney and DeLaurier in 1981 [6], but recently there has been renewed interest both experimentally and computationally in the form of various kinematic strokes, pitching axes, and flow conditions for optimal performance [7–9]. In the original exploration of oscillating hydrofoils, McKinney and DeLaurier defined the pitch and heave using sinusoidal functions, showing with both theory and experiments that the oscillating hydrofoil had the potential to perform at an efficiency comparable to rotating energy extraction devices [6]. Since then systems have been explored that completely drive the pitch and heave motion, or have at least one degree of freedom passively driven with a torsional or linear spring [10, 11]. In terms of completely driven systems, Simpson et al. performed experi-

mental measurements on a NACA 0012 foil in a tow tank, characterizing the performance for a range of kinematic parameters in pure sinusoidal motion [12]. An elliptic symmetric foil for easy tidal flow reversal was investigated experimentally by Kim et al. [13] in a recirculating flume. Water flume confinement effects on energy harvesting performance have also been studied [11,14]. Various prototypes have also been designed and/or tested to date, including a 2 kW prototype based on studies at Laval University [15] and a 1 kW prototype developed at Brown University [4,16].

Kinsey and Dumas carefully explored a wide range of parameters computationally on a NACA 0012 foil, and found a peak efficiency of approximately 34% [17]. The optimal range of kinematics, also documented by other researchers [18,19], has been found to be at a reduced frequency, fc/U_∞, of $0.10 - 0.15$, lower than that found in propulsive oscillating foils.The optimal phase difference between the pitch and heave cycles is approximately $90°$, with heave amplitudes, h_o/c, within the range of $0.5 - 2.0$, and pitch amplitudes, θ_o, within the range of $55°$ to $80°$. These optimal values have been demonstrated for a variety of slender foil shapes undergoing pure sinusoidal motion with pivot locations at or close to center chord.

A key component to the optimal power production is the formation and timing of a coherent leading edge vortex (LEV) which can enhance lift forces, and thus power, throughout the heave stroke depending on foil kinematics [13,20]. The LEV formation and shedding was shown to depend on the oscillating frequency and plunge amplitude of the foil by Baik et al. in their work on LEV dynamics and unsteady forces produced by pitching and plunging airfoils across different Reynolds numbers [21]. The large coherent vortices that are shed in the high-efficiency kinematic regime share a resemblance to bluff-body vortex-induced vibrations, which have also been applied towards hydrokinetic energy harvesting applications [22]. The trajectory of the highly coherent vortex structures are critical in placement of subsequent oscillating foils in array configurations [23].

1.3 Power Generation on Oscillating-Foil Arrays

Although the performance and kinematics of a single foil in freestream conditions are well understood both numerically [17, 19, 24–26] and experimentally [6, 13, 20, 27, 28], foils in coordinated array configurations as exemplified in Figure 1.4 have not received as much attention. As observed in other wind and hydrokinetic turbines, the downstream foils of arrays suffer from reduced freestream velocity and wake disturbances. Thus, a major challenge within the industry is to accurately predict and model how the wake of one turbine affects the others downstream. Progress has been made in wind farm layouts [29, 30], however due to the oscillatory, rather than rotational, kinematics the wake structure of oscillating foils is vastly different from that of traditional horizontal-axis turbines. Moreover, the wake structure is a strong yet nonlinear function of the precise kinematic motion of the foil.

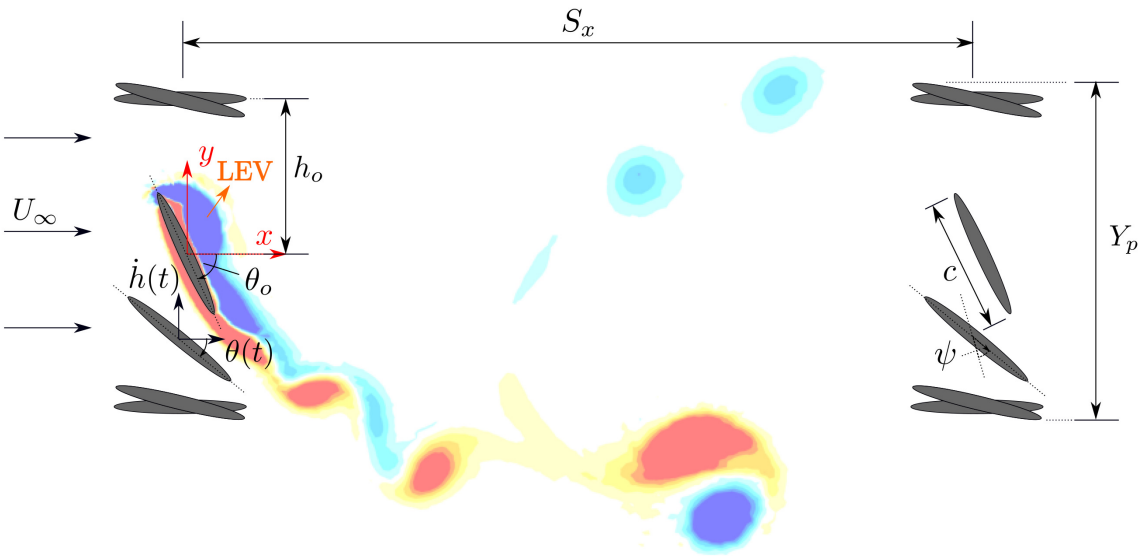

Figure 1.4: Two oscillating foils in a tandem arrangement configuration.

A distinguishing flow feature of the high-pitch and high-heave kinematics is the trail of coherent vortices formed in the wake. Throughout most of the energy harvesting kinematic parameter space one or more leading edge vortices (LEVs) are shed on each half-stroke, sometimes accompanied by a trailing edge vortex (TEV) [17, 25]. The structured

pattern of these relatively two-dimensional coherent vortices differs widely from the three-dimensional wake of horizontal-axis turbines [7,8,31]. The formation and wake dynamics of the shed vortices are strongly correlated with the specific kinematic parameters. However, for the optimal kinematics it has been shown that the boundary layer separates very close to the leading edge of the foil. Due to the leading edge separation the dynamics and energy harvesting performance are relatively insensitive to the blade geometry [13].

When foils are arranged in a tandem array the layout introduces two configuration parameters, the inter-foil distance, S_x, and inter-foil phase, ψ, as displayed in Figure 1.4. Inter-foil phase describes the phase difference between leading and trailing foils which are both undergoing the same kinematics. Through experiments in a water tunnel at $Re = 20,000$ and using fixed foil kinematics of $fc/U_\infty = 0.80;\ h_o/c = 1.05;\ \theta_o = 73°$, Platzer et al. [32] discovered that any slight change in the configuration parameters will affect the trailing foil's performance. Using the same flow conditions and kinematics as Platzer et al., Ashraf et al. [33] performed numerical simulations using two mesh zones, a dynamic mesh close to the foil and a stationary zone with a sliding interface in-between zones. They varied S_x from $2c$ to $6c$ demonstrating that the trailing foil efficiency increased when the inter-foil phase was nonzero. Subsequent simulations by Broering and Lian [34] and Broering et al. [35] at $Re = 10,000$ observed that both inter-foil phase and spacing had similar effects on power generation, however these were performed at lower pitch and heave amplitudes ($h_o/c = 0.50; \theta_o = 20°$), likely avoiding the flow separation and LEV generation characteristic of higher amplitudes. Karakas and Fenercioglu [36] experimentally investigated the inter-foil phase effects on power generation of a two-foil fixed set of kinematics and obtained an optimal inter-foil phase of $135°$ from the observation of wake-foil interactions through an inter-foil phase variation of $-180° - +180°$. Numerical work from Ma et al. [37] has coupled the motion of the leading and trailing foils in passive tandem arrays and noted how the inter-foil distance impact the system dynamics. Experimental work from Ramananarivo et al. [38] and Newbolt et al. [39] showed that

when two foils are arranged in a tandem array and are randomly perturbed, the flow interaction between the trailing foil and the wake generated by the leading foil promoted group cohesion, similar to those found in fish schooling and bird flocking. Their results show that foil kinematics and configuration parameters can be used to control locomotion within wakes.

1.4 Wake Characterization through Machine Learning

Machine learning techniques have received attention in fluid dynamics in terms of predicting, clustering and classifying complex flow physics. When utilizing oscillating foils to harvest hydrokinetic energy, it is critical to understand the intricate and nonlinear relationship between foil kinematics and the downstream vortex wake structure for optimal siting and operation of arrays.

Wakes of bluff bodies have been most commonly investigated for cylindrical geometries, such as the canonical work of Williamson and Roshko [40] who describe vortex wakes with a '$mS + nP$' notation, where m is the number of single vortices (S) shed per cycle, and n is the number of clockwise/counter-clockwise vortex pairs (P). This notation has been propagated to oscillating foils with some success [41], and others have thoroughly investigated wake structures behind both pitching [42] and plunging motions [43] primarily for propulsive applications. When used for energy harvesting, the foil kinematics are characterized by a lower non-dimensional frequency and higher pitch/heave amplitudes compared to oscillating foil propulsion. The high amplitudes result in rich wakes of multiple alternative sign vortices shed at each foil stroke that are often chaotic and not easily identified by the '$mS + nP$' notation [44].

In terms of characterizing wakes structures of bluff bodies, various machine learning techniques can be utilized. Particularly, convolutional neural networks (CNN) have received much interest due to the ability to process data from images for pattern recognition

and prediction [45]. For instance, this type of neural network helped develop a model to analyze unsteady flow over a circular cylinder at various Reynolds numbers and obtained accurate predictions [46]. Similarly, Bhatnagar et al. predicted flow fields around various airfoil shapes [47]. A CNN was also utilized to develop a vortex identification technique that could potentially replace existing identification methods such as the Q-criterion [48] or the λ_2 criterion [49], which typically require user-input for appropriate thresholds [50]. Calvet et al. developed a convolutional autoencoder (CAE) that extracted the most pertinent features of an oscillating foil in propulsion mode and used it to automatically cluster wake patterns from various foil kinematics through a k-means++ algorithm [51]. Using a semantic segmentation approach within a CNN, Kashir et al. [52] successfully applied feature extraction to a lid-driven cavity flow. CNNs have also been used to predict drag and lift coefficients on a flat plate and on two side-by-side cylinders [53].

When analyzing unsteady flows, the time evolution of structures is relevant in capturing the subtle differences between present and past timesteps. Recurrent neural networks and especially their improved version, the long short-term memory (LSTM) method [54], have been shown to predict flow structures based on past instances. The internal memory of a LSTM unit holds information on the recent context in an input sequence, and not simply from the current input to the neural network [55]. Using flow information from the past five timesteps, Nakamura et al. [56] predicted turbulent structures in a channel flow using a convolutional autoencoder combined with LSTM. LSTM was also used to develop a novel dynamic wind farm wake model that predicts the main features of unsteady wind turbine wakes almost as well as high-fidelity wake models [57]. Using convolutional layers and LSTM units, Han et al. [55] predicted unsteady flow fields behind bluff bodies such as a cylinder and a foil.

1.5 Thesis Manuscript Structure

Chapter 2: CFD Methods

The numerical methods implemented in this preliminary manuscript are outlined in this chapter. 2D DNS is utilized in all upcoming chapters and 3D LES is used for the Reynolds number dependence analysis (chapter 3).

Chapter 3: Vortex Dynamics and Reynolds Number Effects for a Single Foil

Power generation on oscillating foil turbines are highly dependent on vortex formation and shedding. Therefore, it is critical to capture the dynamic stall properties of the foil as it undergoes high angles of attack and to accurately investigate those properties, 3D large eddy simulations (LES) at $Re = 50,000$ are performed and further compared with direct numerical simulations (DNS) in 2D at $Re = 1000$ along with a vortex tracking analysis as it convects downstream.

Related presentations and published journal articles

1. *Ribeiro, B. L. R., Frank, S. L., & Franck, J. A. (2020), "Vortex dynamics and Reynolds number effects of an oscillating hydrofoil in energy harvesting mode," Journal of Fluids and Structures, vol. 94, p. 102888. https://doi.org/10.1016/j.jfluidstructs.2020.102888*

2. *Lee, H., Ribeiro, B. L. R., Simone, N., Su, Y., Zhu, Y., Franck, J. A., & Breuer, K. (2021). "Leading edge vortex formation and wake trajectory: Synthesising measurements, analysis, and machine learning,". Physical Review Fluids, vol. 7, Iss. 7, p. 074704. https://doi.org/10.1103/PhysRevFluids.7.074704*

3. *71st annual meeting of the APS Division of Fluid Dynamics, November 2018.*

4. *72nd annual meeting of the APS Division of Fluid Dynamics, November 2019.*

Chapter 4: Wake-Foil Interactions in Tandem Oscillating Foils

The effects of foil parameters on foil's performance in a two-tandem array are investigated in this chapter along with a wake analysis in terms of its steady and unsteady flow components. The goal of such wake analysis is to analyze how these flow components are correlated with the foil kinematics since, for instance, for highly detached flows, the unsteady wake component is expected to be more relevant than in a more attached flow due to stronger vortices being generated.

Related presentations and published journal articles

1. *Ribeiro, B. L. R., Su, Y., Guillaumin, Q., Breuer, K. S., & Franck, J. A. (2021), "Wake-foil interactions and energy harvesting efficiency in tandem oscillating foils," Physical Review Fluids, vol. 6, p. 074703. https://doi.org/10.1103/PhysRevFluids.6.074703*

2. *73rd annual meeting of the APS Division of Fluid Dynamics, November 2020.*

Chapter 5: Classification and Clustering of Vortex Wake Modes

To identify wake patterns based on the leading foil kinematics, a combination of two machine learning models is discussed in this chapter. The first model is a supervised algorithm that utilizes a combination of CNN and LSTM units to classify wake structures and the second model is an unsupervised algorithm that clusters images of the wake based on their similarity and through the use of a CAE and a k-means++ algorithm.

Related presentations and published journal articles

1. *Ribeiro, B. L. R., & Franck, J. A. (2021), "Machine Learning to Classify Vortex Wakes of Energy Harvesting Oscillating Foils". AIAA Journal, Vol 61 (3). https://doi.org/10.2514/1.J062091*

2. *AIAA Aviation Forum, August 2021.*

3. *74th annual meeting of the APS Division of Fluid Dynamics, November 2021.*

4. *1st Direct In-person Colloquium on Vortex Dominated Flows, May 2022.*

Chapter 6: Power Extraction and Prediction in a Dual Oscillating Foil System

To optimize foil-array performance, this chapter discusses a power prediction methodology in tandem two-foil arrays. Due to the numerous configurations between the position of wake vortices and the foil, this chapter estimates the power from the trailing foil using the wake velocity and power from a single oscillating foil. This prediction utilizes a physics-based approach from the mean flow and unsteady vortex-foil interactions which are captured through an effective angle of attack of the trailing foil.

Related presentations and in-preparation journal articles

1. *Ribeiro, B. L. R., & Franck, J. A. (2023), "Power Prediction in Oscillating Two-Foil Turbine Arrays". In-preparation.*

2. *AIAA Aviation Forum, August 2022.*

3. *75th annual meeting of the APS Division of Fluid Dynamics, November 2022.*

4. *2nd Direct In-person Colloquium on Vortex Dominated Flows, May 2023.*

2 CFD Methods

This chapter is divided in two sections: Direct numerical simulations (DNS) and large eddy simulations (LES). The DNS section describes the foil parameters investigated in the foil-array simulations along with the mesh sensitivity analysis in the wake and around the foil to fully capture the flow within the boundary layer. The LES section briefly summarizes the LES model implemented in chapter 3.

2.1 Direct Numerical Simulations (DNS)

Tandem-Foil Array Parameters and Performance Metrics

The kinematic motion of each foil is described below in lab-fixed coordinates as

$$h(t) = h_o \cos(2\pi f t + \psi) \tag{2.1}$$

and

$$\theta(t) = \theta_o \sin(2\pi f t + \psi) \tag{2.2}$$

where $h(t)$ and $\theta(t)$ are the prescribed heave and pitch kinematics, respectively, with a pitching motion about the center-chord. Using a fore-aft symmetric elliptical cross-section with a $c/2$ pivot location enables the design to be used in tidal flows that have regular flow reversal. Both the leading and trailing foil have the same kinematics except for an inter-foil phase (ψ) which is zero for the leading foil, and varies between -180° and 180° for the trailing foil. Modifying pitch and heave simultaneously generates a time-varying relative angle of attack with respect to the freestream flow, which is given by

$$\alpha_{rel}(t) = \tan^{-1}(-\dot{h}(t)/U_\infty) + \theta(t), \tag{2.3}$$

with $\dot{h}(t)$ representing the time derivative of the heave motion and $\alpha_{rel}(t)$ is in radians. A representative relative angle of attack is evaluated when the foil is at maximum θ and maximum heave velocity, which occurs at one quarter of the cycle period T, or

$$\alpha_{T/4} = \alpha_{rel}(t = 0.25T). \tag{2.4}$$

To evaluate the performance of different kinematic conditions, the foil's efficiency is defined as

$$\eta = \frac{\overline{P}}{\frac{1}{2}\rho U_\infty^3 Y_p} \tag{2.5}$$

which is the ratio of the average power extracted, $\overline{P}$, to the power available in the oncoming flow window defined by the swept area Y_p. Power generation on an oscillating foil is defined as

$$P(t) = F_y\dot{h} + M_z\dot{\theta} \tag{2.6}$$

that is comprised on a translational component from the vertical force F_y, and an angular component from the spanwise pitching moment M_z. Thus the power is comprised of a translational contribution, $F_y\dot{h}$, and an angular contribution, $M_z\dot{\theta}$.

The calculation of efficiency includes the total available power from the fluid and the total swept area of the device, Y_p, which increases with h_o/c. The swept area Y_p is often greater than twice the heave amplitude, since it takes into account the largest area swept. Another parameter of interest to the renewable energy community is the maximum power of the device regardless of the kinematic stroke. Here, this parameter is defined by the power coefficient, C_p,

$$C_p = \frac{\bar{P}}{\frac{1}{2}\rho U_\infty^3 Sc} \tag{2.7}$$

where the denominator is fixed to the chord and span of the foil, S, and does not change with varying kinematics. All quantities reported are non-dimensionalized by the freestream velocity, U_∞, and the chord length of a single foil, c. To remove small cycle-to-cycle variations, the efficiency, forces, and flow fields are all phase-averaged over the last two cycles of simulation and the experiments are phase-averaged over 10 cycles.

The array configuration parameters of inter-foil phase, ψ, and inter-foil distance, S_x, are varied between computations and experiments in order to cover a wider parameter space, but contain overlap for validation purposes.

The computations are performed with five heave amplitudes in the range of $h_o = 0.50 - 1.50$, six pitch amplitudes between $\theta_o = 55^\circ - 80^\circ$, and three reduced frequencies in the range of $fc/U_\infty = 0.10 - 0.15$ for a total of 46 unique kinematics. Many of these kinematics are performed at an inter-foil distance of $S_x = 6$ for 12 distinct inter-foil phases. To further explore separation distance, the kinematics of $fc/U_\infty = 0.12; h_o = 1.00; \theta_o = 65^\circ$ is also explored for separation distances of $S_x = 4$ and 5 at 12 inter-foil phases. To analyze the correlation between foil kinematics and $\alpha_{T/4}$, seven sets of foil kinematics are specified with the same $\alpha_{T/4}$ value. Table 2.1 summarizes the foil kinematics of all simulated cases, including the $\alpha_{T/4}$ values. The markers next to a few kinematics correspond to those simulated in a two-foil array configuration and are presented in chapter 4.

The experiments are performed with a fixed heave/pitch amplitudes of $h_o = 1.0$ and $\theta_o = 65^\circ$, with six reduced frequencies from $fc/U_\infty = 0.10 - 0.15$ for a total of the six unique kinematics. Experiments are performed at a single inter-foil distance of $S_x = 6$ with 36 different inter-foil phases. To explore separation distance, the same set of foil kinematics as the simulations is performed at $S_x = 8$ and 9, for 36 inter-foil phases. In experiments the inter-foil phase is varied from -180° to 180° in increments of 10° for each set of kinematics, whereas the simulations explore the same range of inter-foil phase sampled at every 30°.

Marker	Kinematics			$\alpha_{T/4}$	Marker	Kinematics			$\alpha_{T/4}$
	fc/U_∞	h_o/c	θ_o			fc/U_∞	h_o/c	θ_o	
-	0.15	1.25	55°	0.09	-	0.15	1.00	70°	0.47
◇	0.12	1.50	55°	0.11	◇	0.12	1.00	65°	0.49
-	0.15	1.00	50°	0.12	-	0.12	0.50	50°	0.51
▷	0.17	1.00	50°	0.14	-	0.10	0.75	55°	0.52
-	0.12	1.00	45°	0.14	▽	0.15	0.75	65°	0.52
-	0.10	1.00	40°	0.14	-	0.12	0.75	60°	0.53
◁	0.16	1.00	55°	0.17	○	0.11	1.00	65°	0.53
-	0.15	0.75	45°	0.17	▽	0.15	1.00	75°	0.55
-	0.12	0.75	40°	0.18	-	0.12	1.25	75°	0.55
▽	0.15	1.00	55°	0.20	-	0.10	0.50	50°	0.57
-	0.10	1.00	45°	0.22	△	0.10	1.00	65°	0.57
-	0.12	1.00	50°	0.23	-	0.12	0.50	55°	0.60
-	0.10	0.75	40°	0.26	-	0.10	0.75	60°	0.61
▽	0.15	1.25	65°	0.27	◇	0.12	0.75	65°	0.62
-	0.15	1.00	60°	0.29	-	0.15	1.00	80°	0.64
◇	0.12	1.00	55°	0.31	-	0.10	0.50	55°	0.66
-	0.10	0.75	45°	0.34	◇	0.12	1.00	75°	0.66
-	0.12	0.50	40°	0.34	△	0.10	0.75	65°	0.69
-	0.12	0.75	50°	0.36	-	0.12	0.50	60°	0.69
◇	0.12	1.25	65°	0.38	-	0.12	0.75	70°	0.71
▽	0.15	1.00	65°	0.38	-	0.10	1.25	80°	0.73
-	0.10	1.25	60°	0.38	△	0.10	1.00	75°	0.75
△	0.10	1.00	55°	0.40	-	0.12	1.00	80°	0.75
-	0.12	1.00	60°	0.40	-	0.10	0.75	70°	0.78
☆	0.14	1.00	65°	0.41	-	0.10	0.50	65°	0.83
-	0.12	0.50	45°	0.42	-	0.10	1.00	80°	0.84
-	0.15	1.25	75°	0.44	-	0.12	0.50	70°	0.86
☆	0.13	1.00	65°	0.45	-	0.12	0.75	80°	0.88
△	0.10	1.25	65°	0.47					

Table 2.1: Summary of all simulated kinematics with their computed $\alpha_{T/4}$ values.

Governing Equations and Numerical Techniques

The numerical simulations utilize a direct numerical simulation (DNS) to solve the incompressible Navier-Stokes equations,

$$\rho\left(\frac{\partial \mathbf{u}}{\partial t}+\mathbf{u}\cdot\nabla\mathbf{u}\right)+\nabla p=\nabla\cdot\mu\left(\nabla\mathbf{u}+\nabla\mathbf{u}^{T}\right) \tag{2.8}$$

$$\nabla\cdot\mathbf{u}=0 \tag{2.9}$$

where $\mathbf{u}$ is the velocity vector, p is the pressure, ρ is the fluid's density, and μ is the fluid's dynamic viscosity. All numerical simulations are performed using a second-order accurate finite volume, pressure-implicit split-operator (PISO) method [58] implemented in *OpenFOAM* [59] and under Reynolds number equal to 1000.

In order to impose motion on the foils, a dynamic meshing algorithm is implemented. The mesh motion is initiated by prescribing the position of the cells on the foil's boundary, which align with the desired foil kinematics. The location of all the mesh nodes in the domain are solved at every time step using a solid body rotation (SBR) mesh motion equation [60],

$$\nabla\cdot(\lambda\nabla\mathbf{x_m})+\nabla\left(\lambda\left(\nabla\mathbf{x_m}-\nabla\mathbf{x_m}^{T}\right)\right)-\nu Tr\left(\nabla\mathbf{x_m}\right)=0 \tag{2.10}$$

where ν is the Lamé constant, Tr represents the mathematical trace operation and $\lambda=1/r$ is a diffusion constant for the motion of mesh nodes relative to the boundary motion where r represents the distance from the foil (i.e. solid body). The mesh motion methodology has been previously validated for propulsive oscillating foils [61].

A schematic of the computational domain is shown in Figure 2.1. The domain is $51c$ in the vertical direction with $25c$ upstream of the first foil and $25c$ downstream of the second foil in the horizontal direction. Inlet boundary conditions are imposed on the left side, and outlet conditions on the top, bottom and right sides. A non-slip wall condition is imposed on the foil surface. The mesh motion is constrained to zero at all outer boundaries. The two foils are at rest position (no mesh deformation) at the bottom of the stroke when $\theta=0^{\circ}$, and positioned so the heave stroke is vertically centered in the domain.

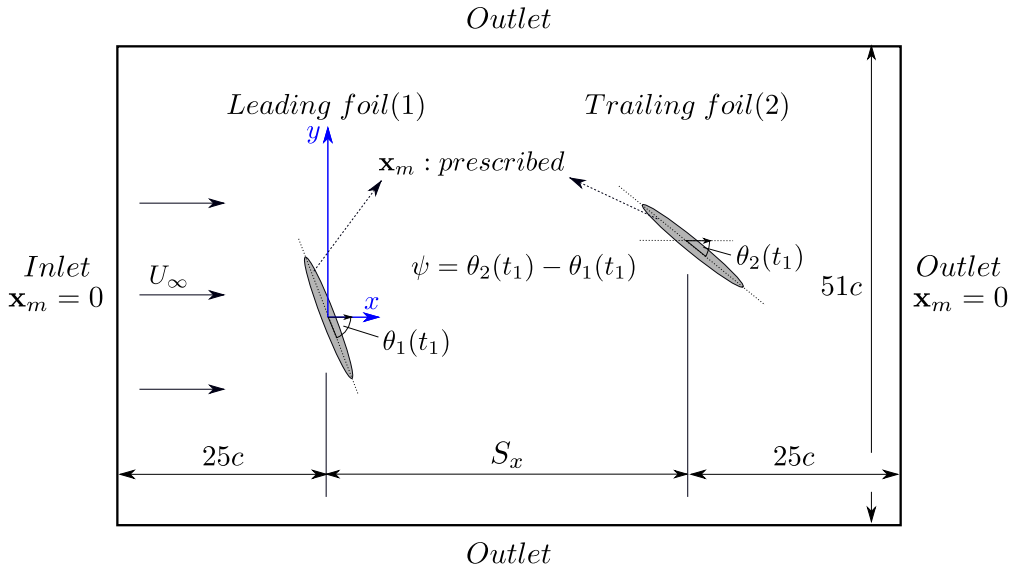

Figure 2.1: Two-foil schematic with boundary conditions and configuration parameters.

Mesh Details

A 2D unstructured mesh is generated using Gmsh [62] for each simulation as shown in Figure 2.2. To properly capture the boundary layer and separation phenomena there is a higher clustering of points around the foils compared to the outer domain, as well as a higher concentration of points within the region between the two foils. Mesh independence is analyzed on eight different meshes with varying resolution as measured in the boundary layer and in the wake between the two foils. Table 2.2 summarizes the characteristics for each of the eight meshes. Meshes 1 to 4 have decreasing Δx values in the wake and close to the foil, and the letters A and B denote the number of nodes along the foil circumference. Figure 2.3 illustrates the cell sizes in the wake and the number of nodes around the foil. For comparison, results from a DNS of a stationary mesh are also displayed in Table 2.2. The stationary mesh uses a non-inertial reference frame to prescribe motion and is only computed with a single foil [44].

Mesh sensitivity is evaluated by comparing the forces directly on the foil and the resolution of flow structures within the wake. Figure 2.4a shows the phase-averaged lift coefficient of the leading foil computed with meshes 1B, 2B, 3B, and 4B, each compared to the

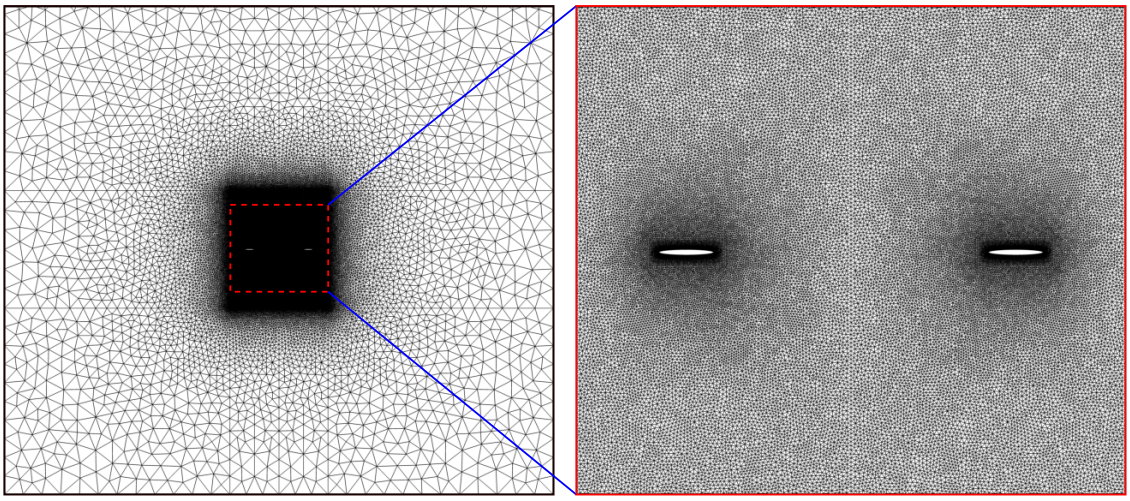

Figure 2.2: Mesh 3B; whole domain (left); immediate vicinity of the two foils (right).

Table 2.2: Mesh characteristics. N is the number of nodes. The wake Δx corresponds to the cell size at an equidistant position between foils. N_θ represents the number of nodes in the azimuthal direction on the foil's surface. The foil Δx corresponds to the cell size at around $0.20c$ from each foil.

		Wake		Foil
Mesh	N	Δx	N_θ	Δx
Mesh 1A	0.21×10^5	0.20	150	0.15
Mesh 2A	0.61×10^5	0.10	150	0.05
Mesh 3A	1.07×10^5	0.07	150	0.03
Mesh 4A	2.46×10^5	0.05	150	0.01
Mesh 1B	0.22×10^5	0.20	240	0.15
Mesh 2B	0.64×10^5	0.10	240	0.05
Mesh 3B	1.10×10^5	0.07	240	0.03
Mesh 4B	2.55×10^5	0.05	240	0.01
Stationary	1.08×10^5	-	240	0.02

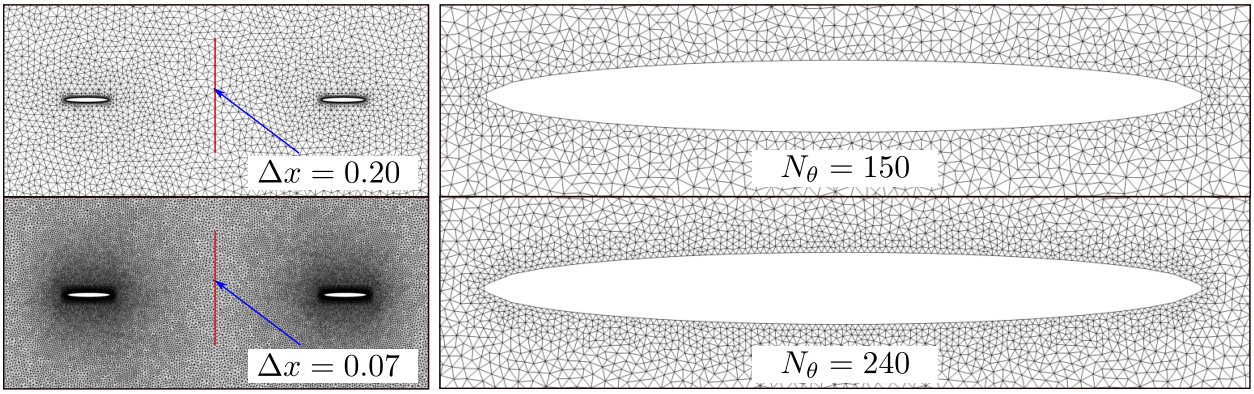

Figure 2.3: Cell sizes at an equidistant position between foils and number of nodes around foil. Top left: Mesh 1B. Top right: Mesh 3A. Bottom left: Mesh 3B. Bottom right: Mesh 3B.

stationary mesh. Since high heave and high pitch amplitudes increase mesh deformation, the forces are evaluated at a representative low ($\alpha_{T/4} = 0.38$) and high ($\alpha_{T/4} = 0.55$) relative angles of attack. As the number of mesh cells N increases, the solution converges to the stationary mesh solution, with minor differences between mesh 3B ($N \approx 1.1 \times 10^5$) and mesh 4B ($N \approx 2.55 \times 10^5$). Due to the high resolution and high deformation, mesh 4B does not work with the higher angle of attack. Figure 2.4b demonstrates the convergence of the solution with increasing resolution by comparing the L^2-norm of the difference between the stationary mesh and the dynamic mesh, computed as

$$||\Delta C_L|| = \sqrt{\frac{1}{n}\sum_{k=1}^{n}(C^k_{L,stationary} - C^k_{L,dynamic})^2}. \tag{2.11}$$

A similar analysis is performed comparing the 'A' and 'B' meshes, yielding small differences between 3A and 3B. Thus the final mesh is chosen to be mesh 3B.

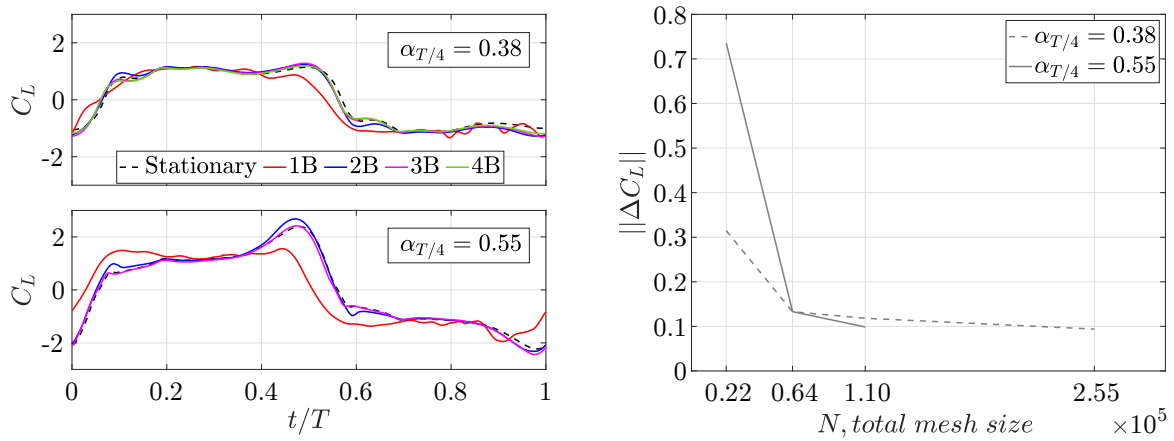

(a) (b)

Figure 2.4: (a) Phase-averaged lift coefficient, C_L, of the leading foil as a function of non-dimensional time, t/T, for each dynamic mesh 'B' compared to the stationary mesh; (b) L^2-norm of the difference between the dynamic mesh and the stationary mesh for increasing mesh size, N (Please refer to Table 2.2 for mesh characteristics).

Figure 2.5 shows the instantaneous spanwise vorticity field, ω_z, for all B meshes at $\alpha_{T/4} = 0.38$. For the chosen kinematics there are multiple vortices present within the wake. To ensure the mesh resolution between the two foils is adequate to capture the

vortices interacting with the trailing foil, a qualitative comparison is shown between the four resolutions. There is a significant difference in vorticity strength between mesh 1B and 2B, indicating that 1B is under-resolved. Meshes 2B, 3B, 4B show the same number of vortices in the wake, however some resolution effects are still detected in 2B, whereas 3B and 4B demonstrate very similar vorticity fields.

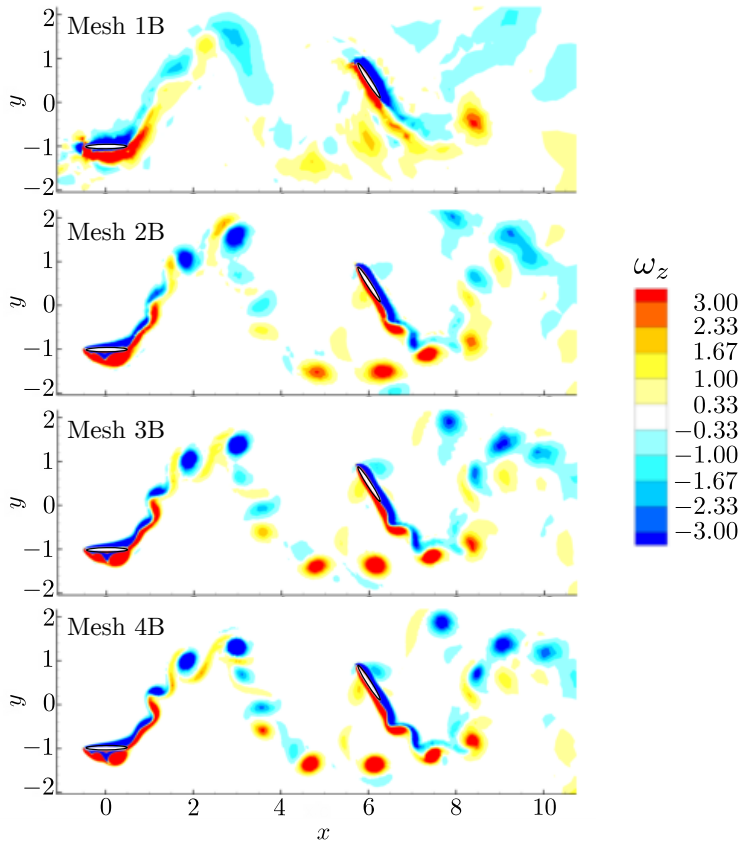

Figure 2.5: Instantaneous vorticity field in the z direction, ω_z. Kinematics: $f = 0.15; h_o = 1.00; \theta_o = 65°$

In summary, mesh 3 shows minimal force and flow-field differences with respect to mesh 4, and mesh 3B is only 6% more computationally expensive than mesh 3A. Thus, mesh 3B is selected for all simulations. With mesh 3B selected for all simulations, 8 cycles are simulated. As a benchmark for computational time, the simulations took 9 hours to run 10 convective time units on an Intel Scalable 2.6GHz processor for a serial run. Job arrays are used to automate the process of running the simulations.

2.2 Large Eddy Simulations (LES)

To evaluate and compare power extraction capabilities of an oscillating hydrofoil in different Reynolds numbers, a three-dimensional LES is performed at $Re = 50,000$ and further compared with the two-dimensional DNS at $Re = 1,000$. The wall-resolved LES is implemented with the spatially filtered incompressible Navier-Stokes equations,

$$\rho\left(\frac{\partial \hat{\mathbf{u}}}{\partial t} + \hat{\mathbf{u}} \cdot \nabla \hat{\mathbf{u}}\right) + \nabla \hat{p} = \nabla \cdot \mu\left(\nabla \hat{\mathbf{u}} + \nabla \hat{\mathbf{u}}^T\right) - \rho\left(\nabla \cdot \boldsymbol{\tau}\right) \tag{2.12}$$

$$\nabla \cdot \hat{\mathbf{u}} = 0 \tag{2.13}$$

where $\hat{}$ represents a low-pass spatially filtered quantity, and $\boldsymbol{\tau}$ is the deviatoric stress tensor. The sub-grid scale stresses are calculated with a constant Smagorinsky model, where

$$\nabla \cdot \boldsymbol{\tau} = -2C_s^2 \Delta^2 |\widehat{\boldsymbol{S}}| \widehat{\boldsymbol{S}} \tag{2.14}$$

and the filtered rate of strain is

$$\widehat{\boldsymbol{S}} = \frac{1}{2}\left(\nabla \hat{\mathbf{u}} + \nabla \hat{\mathbf{u}}^T\right). \tag{2.15}$$

For all LES simulations the Smagorinsky constant is $C_s = 0.1$.

The LES computations included in this document will include a parameter sweep through various heave amplitudes ($h_o/c = 0.5 - 2$) and pitch amplitudes ($\theta_o = 60^\circ - 95^\circ$) at two non-dimensional frequencies of $fc/U_\infty = 0.10$ and $fc/U_\infty = 0.15$. Based on previous data [7,8,17], the maximum efficiency, η, and maximum power coefficient, C_p, are believed to exist within the parameter space tested above.

3 Vortex Dynamics and Reynolds Number Effects for a Single Foil

3.1 Background and Motivation

This chapter, like many articles in the literature, is concerned with the fluid mechanics surrounding the oscillating foil when it is in an energy harvesting kinematics regime, which limits the range of oscillation frequencies and amplitudes explored. Although the overall efficiency of an energy harvesting device will be lower than predicted values due to mechanical losses, the general trends in prototype data have been well predicted by simulations and scaled-down flume experiments [4,16].

An important parameter besides the foil kinematics, especially in terms of informing the design of a large-scale prototype, is the Reynolds number. Direct numerical simulations (DNS) at low Reynolds number on the order of 1000 may not capture the complete flow physics of the experimental flume tests that are typically in the Reynolds number range of $30,000 - 50,000$ due to turbulent transition, or that of full-scale prototypes in a fully turbulent regime. A few groups have computationally explored higher Reynolds numbers, including Ashraf et al. [33] and Xiao et al. [63] who both explored non-sinusoidal effects at moderate Reynolds numbers of $10,000 - 20,000$ using a two-dimensional Navier-Stokes solver. At much higher Reynolds numbers, Kinsey and Dumas [64] used an unsteady Reynolds Averaged Navier-Stokes (RANS) model with a Spalart-Allmaras turbulence closure for two-dimensional and three-dimensional hydrofoils to investigate tip effects and found good comparison with experimental results from a 2 kW prototype with two-foils in a tandem configuration. Campobasso et al. [65] compared low ($Re = 1100$) and high ($Re = 1.5 \times 10^6$) Reynolds number results of a pitching and heaving foil using a compressible Navier-Stokes solver with a $k - \omega$ shear stress transport model, and found

that the two regimes offer different dynamics in terms of optimal parameters for energy harvesting.

This chapter continues to explore a sinusoidal heave and pitch stroke on an elliptical shaped foil, focusing on the effects of Reynolds number between 1000, solved using two-dimensional DNS, and $50,000$, solved using a three-dimensional large-eddy simulation (LES). Direct comparison between these two Reynolds numbers will demonstrate the accuracy and limitations of low Reynolds number flow models compared with a regime an order of magnitude higher coinciding with laboratory flume experiments. The LES methodology allows for a resolved boundary layer which has been shown to accurately capture boundary layer separation and reattachment in unsteady flows [66], compared to RANS models which often over-predict or do not fully capture unsteady vortex dynamics [67]. The three-dimensional LES will also capture spanwise fluctuations and momentum transport within the large-scale vortex structures that are impossible to discern with a two-dimensional DNS.

The computational results are compared against experimental data for validation by examining the forces and moments over the pitch/heave cycle, the efficiency of the stroke for optimal energy extraction, and the LEV formation and trajectory. Of particular interest in this chapter is how the LEV and other large scale structures are formed and convected downstream by the kinematic motion of the foil, and the differences between the two distinct Reynolds number regimes.

3.2 Results and Discussion

Leading Edge Vortex and Effect of Kinematics

Different kinematics from the simulations are directly compared with available flume data [13] in Figure 3.1, in which the efficiency for reduced frequencies $fc/U_\infty = 0.10$ and 0.15 are displayed as a function of pitch and heave amplitude.

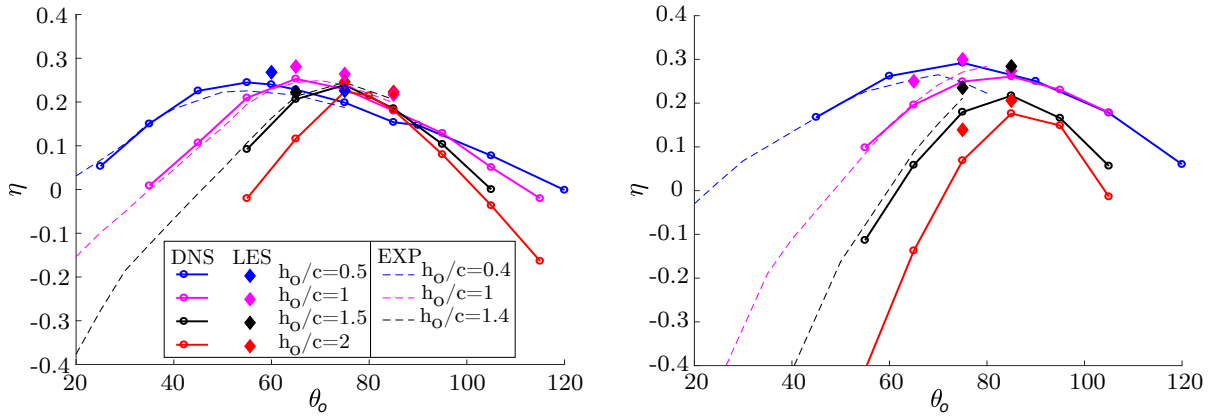

(a) $fc/U_\infty = 0.1$ (b) $fc/U_\infty = 0.15$

Figure 3.1: The efficiency, η, as a function of pitch amplitude, θ_o, for a series of heave amplitudes h_o/c. DNS (—) at $Re = 1000$ is directly compared to experimental flume data (- - -) at $Re = 50,000$ and LES data (diamonds) at $Re = 50,000$.

The LES data in Figure 3.1 closely matches the experimental flume conditions, which has an elliptical foil shape pitched about the center chord and a freestream Reynolds number of $Re = 50,000$ [13]. The DNS maintains the same flow conditions performed at a lower Reynolds number of $Re = 1000$.

The maximum efficiency in the heave range of $h_o/c = 0.5-2.0$ is 28.1% for $fc/U_\infty = 0.10$, and 30.0% for $fc/U_\infty = 0.15$, both at the higher Reynolds number. Both peaks occur at $h_o/c = 1.0$, with pitch amplitudes of $65°$ and $75°$, respectively. For both frequencies tested there is a sharp drop-off in efficiency with higher and lower pitch amplitudes (holding heave amplitude constant), and the optimal pitch amplitude shifts from approximately $60°$ with the lowest heave amplitude of $h_o/c = 0.5$, to approximately $80°$ with the highest heave amplitude of $h_o/c = 2.0$. These trends and peak efficiency values are consistent with the literature [4, 11, 13, 17, 18, 23, 33, 63–65].

Due to the interdependence of all kinematic parameters, the data from Figure 3.1 is plotted as a function of relative angle of attack at mid-upstroke in Figure 3.2. Across various frequencies and heave amplitudes, the efficiency data collapses for $\alpha_{T/4} < 22°$. In this regime the boundary layer is more or less attached to the foil with very little to no separation

and no distinct LEV. The prominent LEV that contributes to the high efficiency modes begins when $\alpha_{T/4} > 22°$. At each heave amplitude the maximum efficiency is achieved within this range where $\alpha_{T/4} > 22°$. Furthermore as the relative angle of attack increases beyond $22°$, the efficiency becomes a strong function of heave amplitude, with the lowest heave amplitudes maintaining the highest overall efficiency with increasing $\alpha_{T/4}$, and the highest heave amplitudes dropping off sharply towards zero efficiency as $\alpha_{T/4}$ increases. Of the kinematics explored the maximum efficiency occurs within the range $35° < \alpha_{T/4} < 50°$.

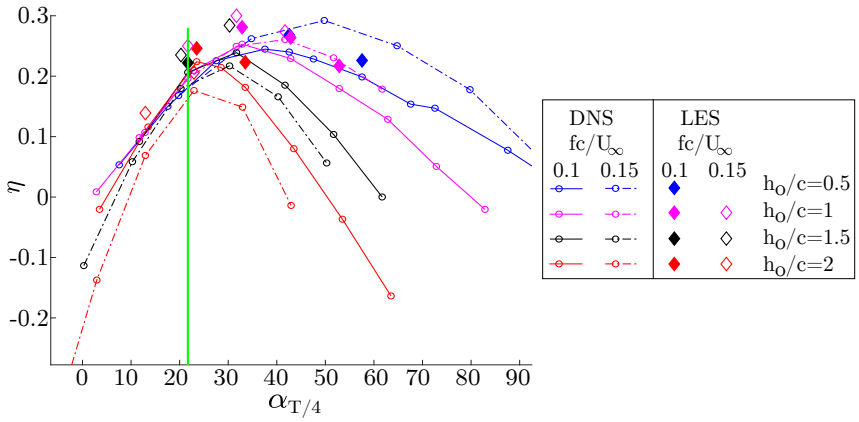

Figure 3.2: Efficiency data from DNS and LES in Figure 3.1 rescaled as a function of the relative angle of attack, $\alpha_{T/4}$ (in degrees).

Comparison with Experimental Data

Figure 3.1 demonstrates a strong agreement between experiments and simulations, and also no significant Reynolds number dependence within the range $Re = 1000 - 50,000$. The in-cycle forces and flow fields are also examined to better understand the similarities and differences between the LES, DNS, and experimental data. Figures 3.3 and 3.4 directly compare the kinematics of $fc/U_\infty = 0.15$, $h_o/c = 1.0$ and $\theta_o = 65°$ in terms of phase-averaged forces, moments, and vorticity fields. In these comparisons the experiments are performed at $Re = 30,000$ with a flat-plate geometry [11], and the conditions for the simulations are the same as Figure 3.1. Despite the slightly different experimental

configuration, the experiments and simulations still show very good agreement in time-dependent lift (C_L) and moment (C_M) coefficients.

In Figure 3.3, the bottom of the downstroke is at $t/T = 0$, and the upstroke occurs in $t/T = 0 - 0.5$. The moment and lift coefficients switch sign at the top of the stroke or just after the stroke reversal, respectively, and repeat the behavior on the downstroke with reversed signs. The green lines at mid-upstroke ($t/T = 0.25$) and the end of downstroke ($t/T = 1$) have their respective vorticity fields presented in Figure 3.4 directly comparing the flow fields for experiments and simulations.

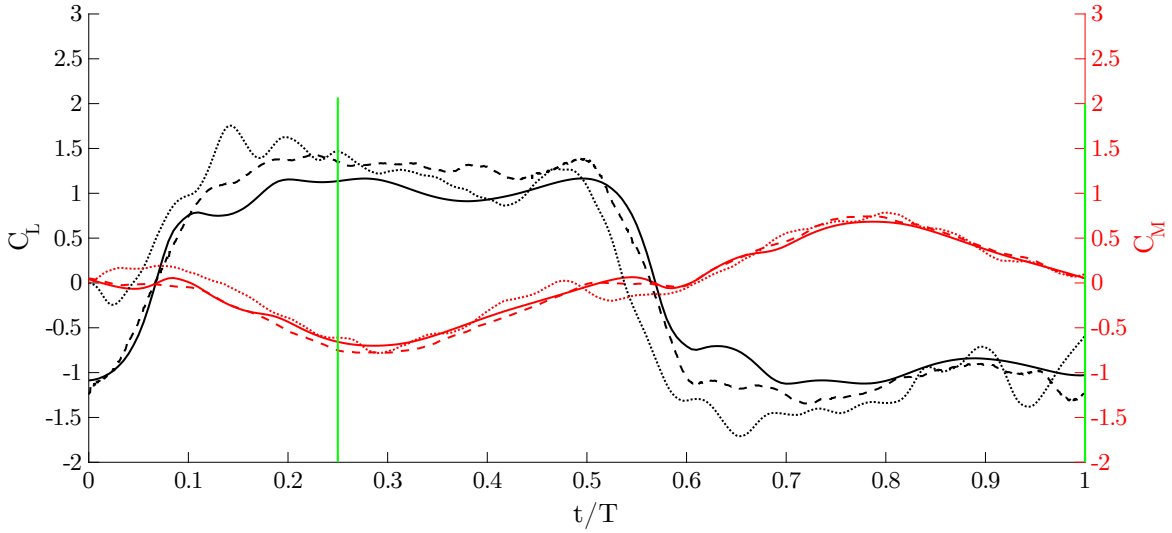

Figure 3.3: Time-dependent lift (C_L) and moment (C_M) coefficients for kinematics $fc/U_\infty = 0.15$, $h_o/c = 1$, $\theta_o = 65°$. LES at $Re = 50,000$ (- - -). DNS at $Re = 1000$ (—). EXP at $Re = 30,000$ (...). Cycle begins at bottom of stroke, upstroke from $t/T = 0 - 0.5$ and downstroke from $t/T = 0.5 - 1$. The vorticity fields represented by the green lines at mid-upstroke and end of downstroke can be seen in Figure 3.4.

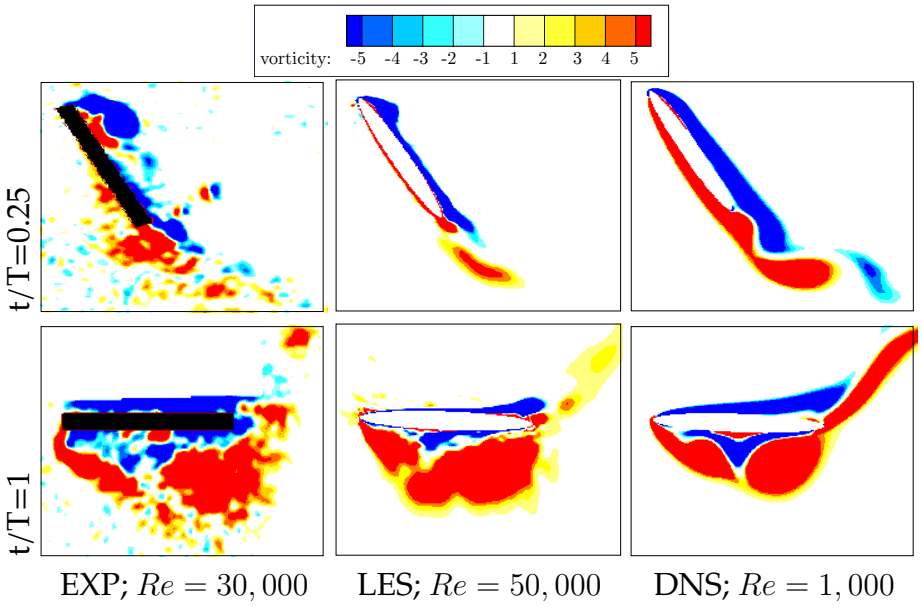

Figure 3.4: Phase-averaged and span-averaged vorticity comparing experimental PIV (EXP), LES and DNS for kinematics $fc/U_\infty = 0.15$, $h_o/c = 1$, $\theta_o = 65°$. Experiments are performed with a flat-plate foil geometry whereas the simulations utilize an elliptical foil. Times shown are represented by the green lines in Figure 3.3.

The top row of Figure 3.4 shows the high-lift configuration at $t/T = 0.25$, which consists of a clearly defined LEV in the LES and PIV vorticity fields. In the DNS the LEV is not yet formed but it does emerge at a slightly later time in the cycle. Due to this delay, the DNS has a lower lift coefficient in this portion of the cycle when compared with the higher Reynolds number LES and experimental results. This LEV persists along the suction surface of the foil until the stroke reversal, and it is present in all the high-efficiency kinematics explored in this chapter. A strong positive lift force during the upstroke, and a strong negative lift force during the downstroke are responsible for most of the power generation, and result in power extracted from the translational, or linear motion of the foil, $C_{p,lin}$. An opposite sign (counter-clockwise rotating) LEV is shown in the bottom row of Figure 3.4 just before it is shed at the bottom of the downstroke. It is found that the energy harvesting efficiency of the foil is very strongly correlated to the LEV formation and shedding time which is governed almost exclusively by the kinematics of the foil and only a weak function of the Reynolds number. Likewise, previous experiments have shown that the foil geometry has

only a minor effect on the efficiency so long as the leading edge is sharp enough to produce an LEV [13].

Contribution of Angular Power

In addition to supplementing the high-lift configuration, the LEV in the top row of Figure 3.4 creates a negative pitching moment. While the foil is increasing its pitch angle (positive angular velocity) the negative pitching moment contributes negative angular power extraction ($C_{p,ang} < 0$). As pitch angle decreases and the angular velocity sign becomes negative (from $t/T = 0.25 - 0.75$) the power due to angular motion is positive. Foil kinematics highly influence the LEV convection and time spent on the foil. At high frequency or high heave amplitude the LEV remains attached longer and has more influence on the vertical force and moment, both of which contribute to power. When the LEV convects past the pitching point at mid-chord, there is a strong negative pitching moment at $t/T = 0.25 - 0.50$ in the opposite direction of the angular velocity, thus creating a negative contribution to power. Thus, as noted in previous experimental studies [13, 20], the exact location and timing of the LEV has a strong influence on the angular power. However, due to the relatively small values of torque compared to lift, the angular power contribution is more often smaller than the power extracted from the translational motion.

In order to further investigate the role of the Reynolds number, and the effect of angular power contributions in high-efficiency configurations, Table 3.1 directly compares the LES and DNS simulations in terms of efficiency, and fraction of power derived from the angular motion of the foil ($C_{p,ang}/C_{p,tot}$) for 15 kinematics across two frequencies.

Although the general trends are consistent across the Reynolds number regimes investigated, results in Table 3.1 demonstrate that there is always a small to moderate increase in efficiency ($\Delta\eta$) with the higher Reynolds number. These ranged from $\Delta\eta = 1.4 - 3.6\%$ for kinematics at $fc/U_\infty = 0.1$ and $\Delta\eta = 0.8 - 6.7\%$ for kinematics at $fc/U_\infty = 0.15$.

Although the translational motion consistently contributed the majority of the power,

Table 3.1: Efficiency η of DNS simulations at $Re = 1000$ compared with LES at $Re = 50,000$. $\Delta\eta = \eta_{LES} - \eta_{DNS}$, and $C_{p,ang}/C_{p,tot}$ is the fraction of power derived from the angular motion of the foil.

Kinematics	$\boldsymbol{\eta}$ **DNS**	$\boldsymbol{\eta}$ **LES**	$\boldsymbol{\Delta\eta}$	$\mathbf{C}_{p,ang}/\mathbf{C}_{p,tot}$ **DNS**	$\mathbf{C}_{p,ang}/\mathbf{C}_{p,tot}$ **LES**
$\mathbf{fc/U_\infty = 0.1}$					
$h_o/c = 0.5$ θ_o=60 °	0.240	0.268	0.028	0.13	0.12
$h_o/c = 1$ θ_o=65 °	0.256	0.281	0.025	0.06	0.05
$h_o/c = 1.5$ θ_o=65 °	0.208	0.222	0.014	-0.02	-0.03
$h_o/c = 0.5$ θ_o=75 °	0.201	0.226	0.025	0.21	0.22
$h_o/c = 1$ θ_o=75 °	0.230	0.264	0.034	0.10	0.10
$h_o/c = 2$ θ_o=75 °	0.222	0.246	0.024	-0.01	-0.01
$h_o/c = 1$ θ_o=85 °	0.181	0.217	0.036	0.16	0.17
$h_o/c = 2$ θ_o=85 °	0.187	0.223	0.036	0.04	0.05
$\mathbf{fc/U_\infty = 0.15}$					
$h_o/c = 1$ θ_o=65 °	0.200	0.250	0.050	-0.18	-0.16
$h_o/c = 1$ θ_o=75 °	0.255	0.300	0.045	-0.10	-0.12
$h_o/c = 1.5$ θ_o=75 °	0.183	0.235	0.052	-0.23	-0.22
$h_o/c = 2$ θ_o=75 °	0.072	0.139	0.067	-0.58	-0.34
$h_o/c = 1$ θ_o=85 °	0.266	0.274	0.008	0.02	-0.08
$h_o/c = 1.5$ θ_o=85 °	0.222	0.284	0.062	-0.16	-0.11
$h_o/c = 2$ θ_o=85 °	0.179	0.206	0.027	-0.28	-0.22

the role of the angular power varies significantly among the high-efficiency kinematics explored in Table 3.1. For kinematics at $fc/U_\infty = 0.1$, the translational and angular power increase proportionally with an increase in Reynolds number, roughly maintaining the percent of total power that comes from angular power. Most of these cases have a negligible or positive contribution. As the frequency increases to $fc/U_\infty = 0.15$ the contribution is now negative for both Reynolds number regimes, but the ratio varies significantly from -0.58 to $+0.02$. The largest contributor of negative power at $C_{p,ang}/C_{p,tot} = -0.58$ is for $h_o/c = 2$ and $\theta_o = 75°$, in which the total efficiency is significantly impacted resulting in $\eta = 0.072$ for the DNS. The high Reynolds number simulation for these kinematics only slightly increased the efficiency ($\eta = 0.139$) due to less negative angular power contributions. The opposite extreme is when the angular power contributions are close to zero, for example

the kinematics of $fc/U_\infty = 0.15$, $h_o/c = 1$ and $\theta_o = 85°$, which have efficiency values of $\eta = 0.266$ and $\eta = 0.274$ for low and high Reynolds number respectively.

Vortex Dynamics and Trajectory

The location and strength of one or more LEVs can significantly modify the energy harvesting potential of a foil. Furthermore, once the LEV is shed, its trajectory can also impact the performance of downstream foils. To better understand the LEV formation and resulting trajectory, this section tracks the location of the primary LEV formation on the foil and in the near wake region for a subset of high-efficiency kinematics.

The tracking algorithm relies on a user input to select the LEV to be tracked shortly after it is formed. The primary LEV, or the first LEV that rolls up from the leading edge on the upstroke will be tracked. At every $tU_\infty/c = 0.1$ timesteps the position of the maximum value of vorticity for this specific vortex is tracked as it forms on the foil and then sheds downstream for approximately three chord lengths. In order to clearly identify the primary LEV the $fc/U_\infty = 0.1$ kinematics have $t/T = 0.25$ as an initial time and the $fc/U_\infty = 0.15$ kinematics start tracking at $t/T = 0.30$ due to the delayed LEV formation.

Figure 3.5 shows the vortex tracking from phase-averaged PIV [11], DNS and LES flow fields for the kinematics $fc/U_\infty = 0.1$, $h_o/c = 1$ and $\theta_o = 65°$. Overlaid with the primary LEV path is the foil motion during its upstroke and the vorticity fields from DNS to show the LEV size and position relative to the trajectory at $t/T = 0$, 0.25, 0.50, and 0.62. There is strong agreement between PIV, DNS and LES, in terms of vortex position and shedding time. The LEV decays faster with increasing Reynolds number, and the vortices become more difficult to track as shown by the PIV data at approximately $x/c = 2.5$ where the tracking algorithm has a larger discrepancy shown by the increased size of the PIV error bars in Figure 3.5. The PIV data is more difficult to accurately track far from the foil, which is likely due to the three-dimensional wingtip effects in the experiments compared with

the infinite-span model in the DNS and LES. Due to the similarity between the two sets of simulations and experiments, only DNS tracking is discussed in the following analysis.

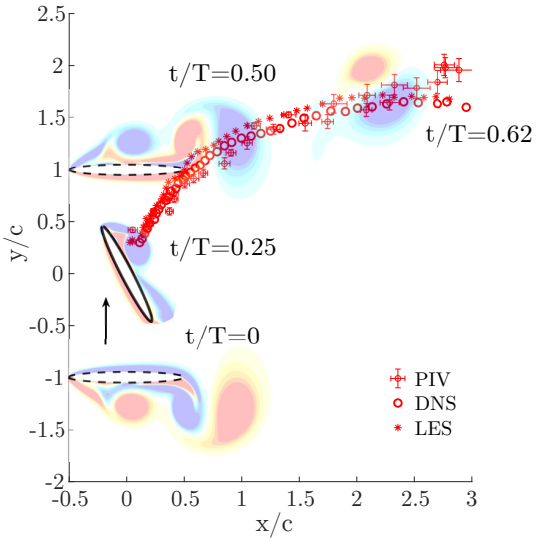

Figure 3.5: LEV trajectory from PIV, DNS and LES superimposed with contours from DNS to illustrate LEV size and position at t/T = 0, 0.25, 0.50 and 0.62. Kinematics: $fc/U_\infty = 0.1, h_o/c = 1, \theta_o = 65°$.

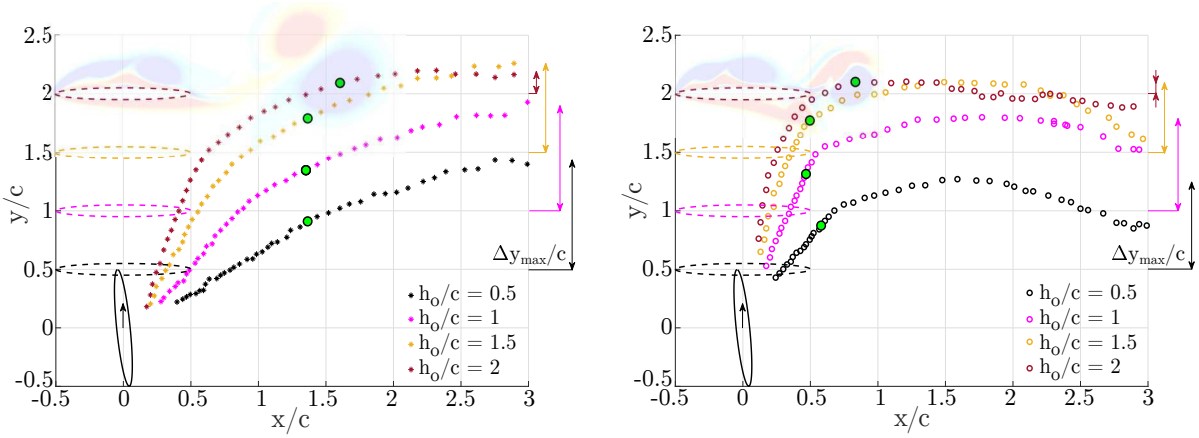

(a) $fc/U_\infty = 0.1$ and $\theta_o = 85°$ (b) $fc/U_\infty = 0.15$ and $\theta_o = 85°$

Figure 3.6: Effect of heave amplitude, h_o/c, on LEV trajectory. Contours at the top of upstroke for $h_o/c = 2$ illustrate differences of the LEV core location in two frequencies with fixed $\theta_o = 85°$.

The path of the LEV varies significantly with changing kinematics. Figure 3.6 shows the effect of heave amplitude on the LEV dynamics for fixed pitch amplitude $\theta_o = 85°$ and two reduced frequencies, $fc/U_\infty = 0.1$ and 0.15. The solid line is the foil position at

mid-upstroke, $t/T = 0.25$, and the path of the LEV corresponds to the four colored foils representing heave amplitudes $h_o/c = 0.5$, 1, 1.5, and 2. With increasing heave amplitude, the maximum vertical distance traveled by the LEV saturates. In Figure 3.6a, comparing the vertical distance with the top of the heave stroke, the value of $\Delta y_{max}/c$ is almost zero at $h_o/c = 2$, meaning the LEV maintains the same vertical position as the foil. In comparison at low heave of $h_o/c = 0.5$, the LEV travels approximately 1 chord length higher than the maximum position of the foil, or $\Delta y_{max}/c = 1$. This behavior is similar at $fc/U_\infty = 0.15$ in Figure 3.6b, except $\Delta y_{max}/c \approx 0.75$ at its maximum. Thus, a nonlinear dependence of $\Delta y_{max}/c$ with heave amplitude is found in these two frequencies.

In the background of Figures 3.6a and 3.6b the vorticity field at $t/T = 0.50$ shows the LEV location for the heave amplitude $h_o/c = 2$, and the LEV core position is given by the green marker. This marker of $t/T = 0.5$ is represented in the lower heave amplitudes as well. The horizontal position of the vortex is very similar for $h_o/c = 0.5 - 1.5$, however at $h_o/c = 2$ it has traveled further downstream. This is due to an earlier shedding time at this high amplitude, and the LEV separates from the foil prior to completion of the upstroke. This in turn allows the vortex to travel more horizontal distance but limits its vertical motion.

The frequency also significantly alters the path of the primary LEV between Figures 3.6a and 3.6b. At $fc/U_\infty = 0.15$ the trajectory is linear while the LEV is close to the foil then turns abruptly in a horizontal trajectory downstream. During the relatively fast heaving motion the LEV convects with the foil in a rigid body motion, hence limiting the LEV size and horizontal location. This also explains the near-foil location of the LEV at $t/T = 0.5$ indicated by the green markers in Figure 3.6b. At $fc/U_\infty = 0.1$ the stroke is relatively slower, the LEV grows larger and is shed earlier in the cycle, and travels further downstream by $t/T = 0.5$, as indicated by the green markers in Figure 3.6a.

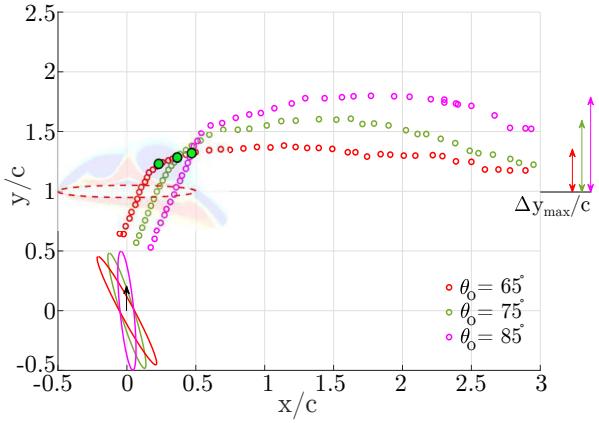

Figure 3.7: Effect of pitch amplitude, θ_o, on LEV trajectory with $fc/U_\infty = 0.15$ held constant. Contours at the top of upstroke for $h_o/c = 1$ illustrate the LEV core location for $\theta_o = 65°$.

In a similar analysis the frequency and heave are held constant ($fc/U_\infty = 0.15$ and $h_o/c = 1$) and the effect of pitch amplitude on the LEV trajectory is shown in Figure 3.7. As the pitch amplitude increases the LEV grows to a larger size and is located closer to the trailing edge at stroke reversal (green markers) due to the larger angular velocity within an equal heaving distance. Within the high-efficiency energy harvesting range that is explored between $\theta_o = 65°$ to $85°$, the LEV size and maximum height follow a linear dependence with pitch amplitude.

3.3 Conclusion

The energy harvesting mechanisms of an elliptical oscillating foil are explored for two non-dimensional frequencies, $fc/U_\infty = 0.10$ and 0.15 at $Re = 1000$ and $Re = 50,000$ with the goal of exploring the differences in power generation and vortex dynamics across the two Reynolds numbers. A sweep of pitch and heave amplitudes were performed at $Re = 1000$ and those kinematics that yielded the highest efficiency or power generation capability were repeated with LES at $Re = 50,000$, and compared with available experimental results. It is found that there were only minor variations in the energy extraction and vortex dynamics between these two Reynolds number regimes. For the lower frequency of $fc/U_\infty = 0.10$ the

maximum efficiency of 25.6% occurs at a heave amplitude of $h_o/c = 1.0$ and pitch amplitude $\theta_o = 65°$, and is increased to 28.1% for a Reynolds number of $50,000$. This modest increase in power production is seen with all the high Reynolds number cases at $fc/U_\infty = 0.10$. At the higher frequency of oscillation, $fc/U_\infty = 0.15$, the high and low Reynolds number results show more variability, with the $Re = 50,000$ flow extracting $0.8 - 6.7\%$ more energy than the same kinematics at $Re = 1000$.

A persistent feature of all high-efficiency kinematics is a coherent LEV that forms on the heave stroke, and sheds at or just after the heave stroke reversal. This occurs at high relative angles of attack, which is consistent with large heave and/or pitch amplitudes. Comparing all data in terms of relative angle of attack at mid-upstroke, or $\alpha_{T/4}$, it is shown that the maximum efficiency for each heave occurs when $\alpha_{T/4} > 22°$, or when the flow has clearly separated from the foil. As the flow separates at the leading edge it forms a LEV that persists throughout the upstroke, enhancing the lift, and thus the power extraction from the translational motion. When comparing the two Reynolds number regimes, the increase in efficiency with higher Reynolds number is from a slightly stronger LEV that forms earlier in the heave cycle, and enhances the power extraction from both lift and torque during critical portions of the cycle.

The details of this LEV formation, shedding, and trajectory are examined through tracking its core position through phase-averaged data. In comparing experiments with DNS and LES results, it is found that the primary LEV position downstream is relatively independent of Reynolds number, but that it is strongly influenced by its kinematics. The maximum vertical distance traveled by the primary LEV is reported, as well as its trajectory up to 3 chord lengths downstream. As the heave amplitude is increased to $2c$ the maximum vertical distance saturates because the LEV is shed earlier in the heave process, resulting in a relatively horizontal trajectory. At a reduced frequency of $fc/U_\infty = 0.1$ the primary LEV is almost one full chord length downstream by mid-stroke, and the vertical trajectory dependent on pitch and heave amplitude. As the reduced frequency is increased

to $fc/U_\infty = 0.15$ the LEV has less time to develop, resulting in the primary LEV very close to the trailing edge at mid-stroke.

The implications of the Reynolds number independence in terms of efficiency and vortex dynamics are important to understand how oscillating foil energy harvesting devices will scale with size and flow speed. Furthermore the impact of the coherent vortices in the wake is likely to be an important factor in array design and configuration.

4 Wake-Foil Interactions in Tandem Oscillating Foils

4.1 Background and Motivation

Understanding the wake dynamics is critical for developing a physics-based model of how the kinematics and array configuration parameters influence energy harvesting performance. The path of individual vortices within the wake is highly dependent on the leading foil kinematics [44] and affects how or if the trailing foil interacts with the vortices originating from the leading foil. Through experiments and simulations performed in a flow at $Re = 30,000$, Rival et al. [68] discovered two types of wake-foil interactions. The first type occurs when the LEV from the leading foil induces a leading edge suction region generating a thrust force on the trailing foil, hence decreasing power generation. The second type of interaction occurs when the trailing edge vortex (TEV) from the leading foil induces flow separation on the trailing foil's upper surface, increasing power generation. Their conclusions are obtained using a two-foil system placed in close proximity to one another ($S_x = 2c$) with small heave and pitch amplitudes ($h_o/c = 0.50;\ \theta_o = 8°$). Through two-dimensional simulations at $Re = 44,000$ and fixed kinematics and configuration parameters of $h_o/c = 1.00;\ \theta_o = 70°;\ \psi = 180°$ and $S_x = 5.4c$, Xu et al. [69] demonstrate that the array efficiency linearly increases with increasing frequency, reaching a maximum at $fc/U_\infty = 0.14$. As the frequency surpasses $fc/U_\infty = 0.14$ the trailing foil performance is heavily influenced by the TEV from the leading foil.

Using actuator disk theory, the optimal efficiency of a single turbine is up to 59.3%, as attributed to Betz [70]. This is expanded to inline turbine arrays by Newman, who demonstrates an optimal system efficiency of 64% [71], meaning that the sum of the power extracted by two devices is 64% of the freestream kinetic energy. These traditional actuator

disk models have been recently revisited by considering both the steady and unsteady components within the flow. Dabiri [72] has developed a theoretical framework that surpasses Betz's limit by relaxing the steady flow assumption, noting that this approach may be particularly useful in oscillating foil arrays to increase performance. From his framework, a theoretical time-averaged power coefficient of 76.4% was obtained, which is significantly higher than Betz's limit. Inspired by Dabiri's framework, Young et al. [73] analyzed the mean and unsteady flow around oscillating foils using a control volume analysis to compute efficiency in single and tandem arrangements. The unsteady terms that arose from the formation and shedding of vortices would entrain additional energy and momentum into the wake, which could be used to increase energy and hence efficiency on downstream foils. Young et al. validated their methodology through a numerical analysis on optimal kinematics obtained from Kinsey and Dumas [74] and achieved similar efficiencies with the control volume analysis as obtained via force computations. They estimated a theoretical maximum efficiency of 77.7% for the tandem foil arrangement, emphasizing the effect of the unsteady terms not previously incorporated by Newman's limit.

Through these recent investigations there is strong evidence that the structured wake, including the unsteadiness imposed by the coherent vortices in the wake, can be utilized beneficially in oscillating foil arrays. However, the generation of the vortices and wake dynamics are primarily governed by the kinematics, which in turn have a large parameter space within energy harvesting regime. Understanding how the leading foil kinematics change the wake structure and dynamics will lead to better wake-foil models, and development of optimal array configurations for energy harvesting. This can lay the foundation for models and control laws that govern the optimization of kinematics between foils within an array, and may also have implications in the bio-inspired propulsion field in terms of interactions between groups of swimmers or fliers.

This chapter focuses on quantifying the effects of foil kinematics within the wake

structure and dynamics. Simulations are performed with two-dimensional direct numerical simulation (DNS), and compared with experiments and Particle Image Velocimetry (PIV). A wide range of kinematics with varying reduced frequencies, heave and pitch amplitudes, inter-foil phase and spacing will be used in a two-foil (tandem) array configuration in order to quantify the effects of foil kinematics in the wake. The vortex structure is used to characterize the wake into three main regimes, that correlate strongly with foil kinematics, and are described by the steady and unsteady components within the flow. Furthermore, a modified efficiency is introduced that incorporates available energy from steady and unsteady regions within the wake.

4.2 Results and Discussion

Relative Angle of Attack as a Predictive Quantity

Given the large kinematic parameter space, it is convenient to reduce frequency, pitch and heave amplitude into a single parameter and utilize the relative angle of attack at maximum pitch ($\alpha_{T/4}$), as defined by Equation 2.3, as a representative of the sinusoidal kinematics [13, 17, 44]. Figure 4.1 shows the leading and trailing foil efficiency of most kinematics listed in Table 2.1. All points correspond to cases with the same inter-foil distance ($S_x = 6$) and each point for the trailing foil corresponds to the inter-foil phase that provides the highest efficiency.

As shown by Figure 4.1, $\alpha_{T/4}$ is strongly correlated with the foil's energy harvesting efficiency [13, 20, 44, 74], and strong agreement is observed between the experiments and simulations. The leading foil efficiency increases as $\alpha_{T/4}$ increases, until around $\alpha_{T/4} = 0.50$ where it reaches a maximum efficiency of approximately 25%. Surpassing $\alpha_{T/4} = 0.60$, leading foil efficiency decreases slightly, indicating the foil kinematics are receding from the optimal energy harvesting range. The trailing foil follows a similar trend at lower angles of attack, but due to less available kinetic energy in the wake between foils it plateaus at an

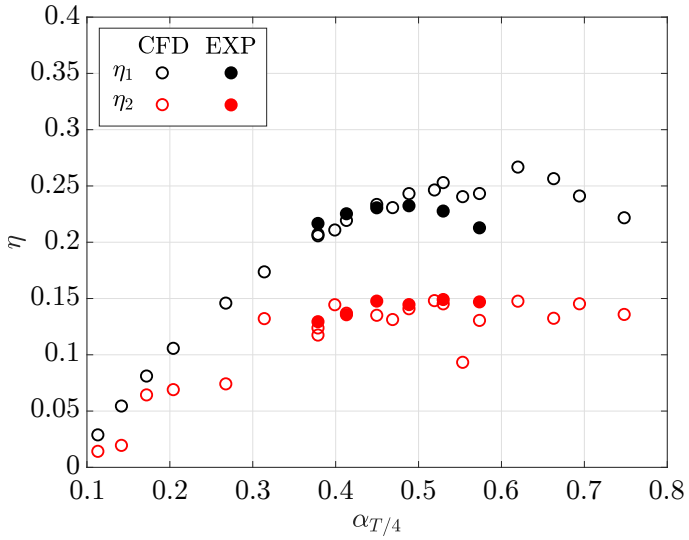

Figure 4.1: Leading and trailing foil efficiencies, η_1 and η_2 respectively, with respect to various $\alpha_{T/4}$ for both simulations and experimental data.

efficiency of 15% at $\alpha_{T/4} = 0.40$. However, after this angle of attack the efficiency remains constant with increasing $\alpha_{T/4}$ as opposed to the slight decay seen for the leading foil. The data for both experiments and simulations agree that $\alpha_{T/4}$ is a predictive kinematic quantity in terms of evaluating the energy harvesting efficiency over a range of diverse kinematics, but also that the trailing foil suffers from lower efficiency due to the reduced velocity in the immediate wake region.

Wake Velocity, Wake Width and the Relationship with Foil Kinematics

In Figure 4.1, both the leading and trailing foil efficiencies are computed as percent of power extracted from that available in the freestream within the swept area Y_p. However, an alternative definition for the trailing foil involves computing the available power immediately upstream, in the wake between the two foils; this can be performed with a more detailed analysis of the wake properties and characteristics.

First, the formation and strength of the leading edge vortices are analyzed. Depending on the specific kinematics, there are one or multiple vortices shed per half-stroke. To understand the wake's dependence on foil kinematics, the strength of the primary vortex is

computed as a function of $\alpha_{T/4}$ in Figure 4.2. The primary vortex is defined as the strongest vortex developed on the suction side of the foil during a half-stroke. The Q criterion, defined as $Q = \frac{1}{2}\left(\|\mathbf{\Omega}\|^2 - \|\mathbf{S}\|^2\right)$, is computed as a vortex identification method [48], with $\mathbf{\Omega}$ representing the vorticity tensor and $\mathbf{S}$ as the rate-of-strain tensor. Since the vortex strength generally decreases as it convects downstream, only the maximum strength is reported for each set of kinematics in both PIV and numerical data. Thus, Figure 4.2 displays the maximum non-dimensionalized Q (Q/U_∞^2) with respect to $\alpha_{T/4}$.

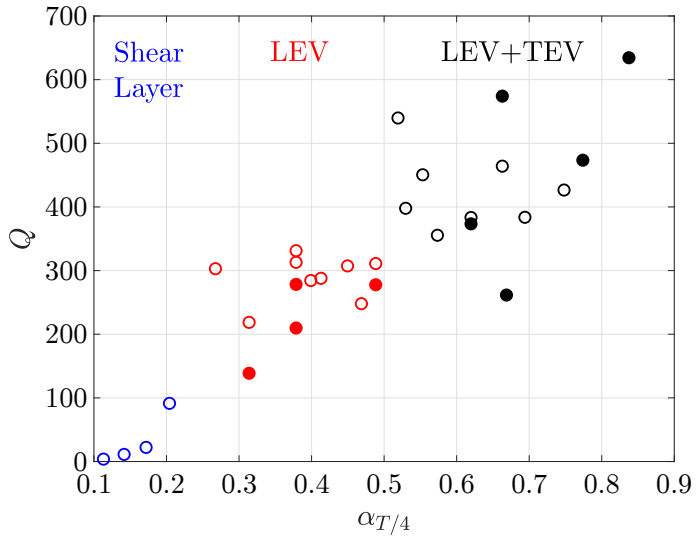

Figure 4.2: Maximum Q value of the primary vortex for each $\alpha_{T/4}$. Open symbols correspond to numerical data. Filled circles are PIV data.

In general, with increasing relative angle of attack the strength of the primary leading edge vortex increases, which is consistent throughout the PIV and simulation data with few exceptions. As $\alpha_{T/4}$ increases, there is more scatter in the maximum Q values between various kinematics, which is likely explained by the flow physics of the higher relative angles of attack described below.

Analyzing the maximum Q values and how they are correlated with $\alpha_{T/4}$, three regimes are identified and defined by low (shear layer regime), medium (LEV regime), and high (LEV+TEV regime) $\alpha_{T/4}$ values, as shown in Figure 4.2. To better understand how these

regimes are defined, Figure 4.3 shows the instantaneous vorticity and Q flow fields for three representative $\alpha_{T/4}$, one for each regime.

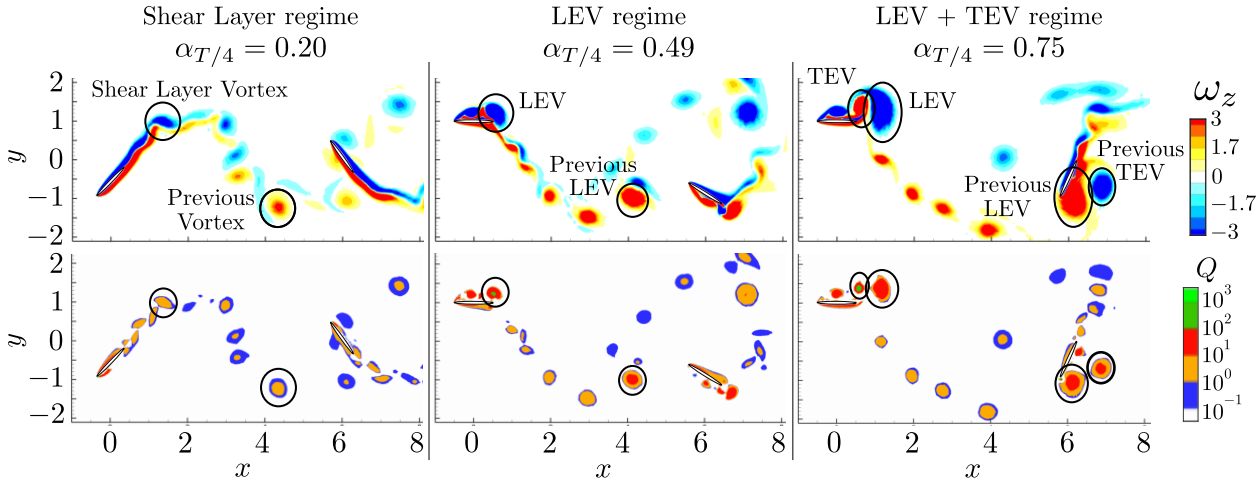

Figure 4.3: Instantaneous vorticity, ω_z, and Q flow fields for a representative $\alpha_{T/4}$ of each regime. The inter-foil phases selected are the cases of maximum trailing foil efficiency. The primary vortex is highlighted (whose path is shown in Figure 4.4), as well as the alternate signed primary vortices from the previous half-stroke. Axes are nondimensionalized by the chord length c.

The first regime is characterized by low relative angles of attack, within the approximate range of $0 < \alpha_{T/4} \leq 0.20$, and is labeled the 'shear layer regime'. For $\alpha_{T/4}$ lower than 0.20, the separation is dominated by a shear layer with very little vortex formation, indicated by Q values close to zero in Figures 4.2 and 4.3. At $\alpha_{T/4} = 0.20$, the shear layer shows a small degree of separation resulting in a relatively small vortex with respect to other kinematics in Figure 4.3, with Q less than or equal to 100. As $\alpha_{T/4}$ increases, Q also increases as the primary LEV grows in size and strength. The second regime, labeled as the 'LEV regime' is from approximately $0.20 < \alpha_{T/4} < 0.50$ and has an easily identifiable primary LEV, as highlighted on the second column in Figure 4.3, whose strength varies between $100 < Q < 350$. At $\alpha_{T/4} > 0.50$, the values of Q generally grow, but have a large range from 250 to 650. A distinguishing feature for this last regime is that the primary LEV is paired with a strong trailing edge vortex (TEV), thus labeled 'LEV+TEV regime'. Due to the addition of more vortices in the wake, the wake-foil interactions are more prevalent for

this final regime as demonstrated by the stronger vortices forming around the trailing foil on the third column of Figure 4.3.

Next, for each of the three regimes, the velocity in the wake is averaged over time and decomposed into its steady and unsteady components,

$$\mathbf{u}(x, y, t) = \overline{\mathbf{u}}(x, y) + \mathbf{u}'(x, y, t), \tag{4.1}$$

where the overline ($\bar{}$) represents a time-averaged quantity. The energy associated with the unsteady components is computed as a turbulent kinetic energy,

$$k(x, y) = \frac{1}{2}(\overline{u'u'} + \overline{v'v'}) \tag{4.2}$$

where $u'u'$ and $v'v'$, correspond to the diagonal terms of the 2D Reynolds stress tensor. It is important to emphasize that the Reynolds decomposition into unsteady components is used to characterize the unsteadiness induced by the large scale vortices in the wake, and not fluctuations due to turbulence. In analyzing the wake characteristics between tandem foils, the first question is whether the presence of the trailing foil modifies the wake dynamics. Figure 4.4 shows the time-averaged vorticity, $\bar{\omega}_z$, streamwise velocity, $\bar{u}$, and turbulent kinetic energy, k, for both single and two-foil simulations on three representative values of $\alpha_{T/4}$, one for each regime. The trajectory of the primary clockwise-rotating vortex (circled in Figure 4.3) is also displayed in each plot to check if the presence of a trailing foil changes the vortex trajectory from the leading foil. Similar from Figure 4.3, the inter-foil phases selected represent the cases of maximum trailing foil efficiency. The leading foil is at maximum pitch angle, or $t/T = 0.25$ for each case.

There is a strong similarity between the vortex path of single and two-foil simulations, indicating that the presence of the trailing foil does not significantly influence the vortices shed from the leading foil, except in the immediate upstream vicinity of the trailing foil. The flow fields are also very similar between configurations, with the major differences

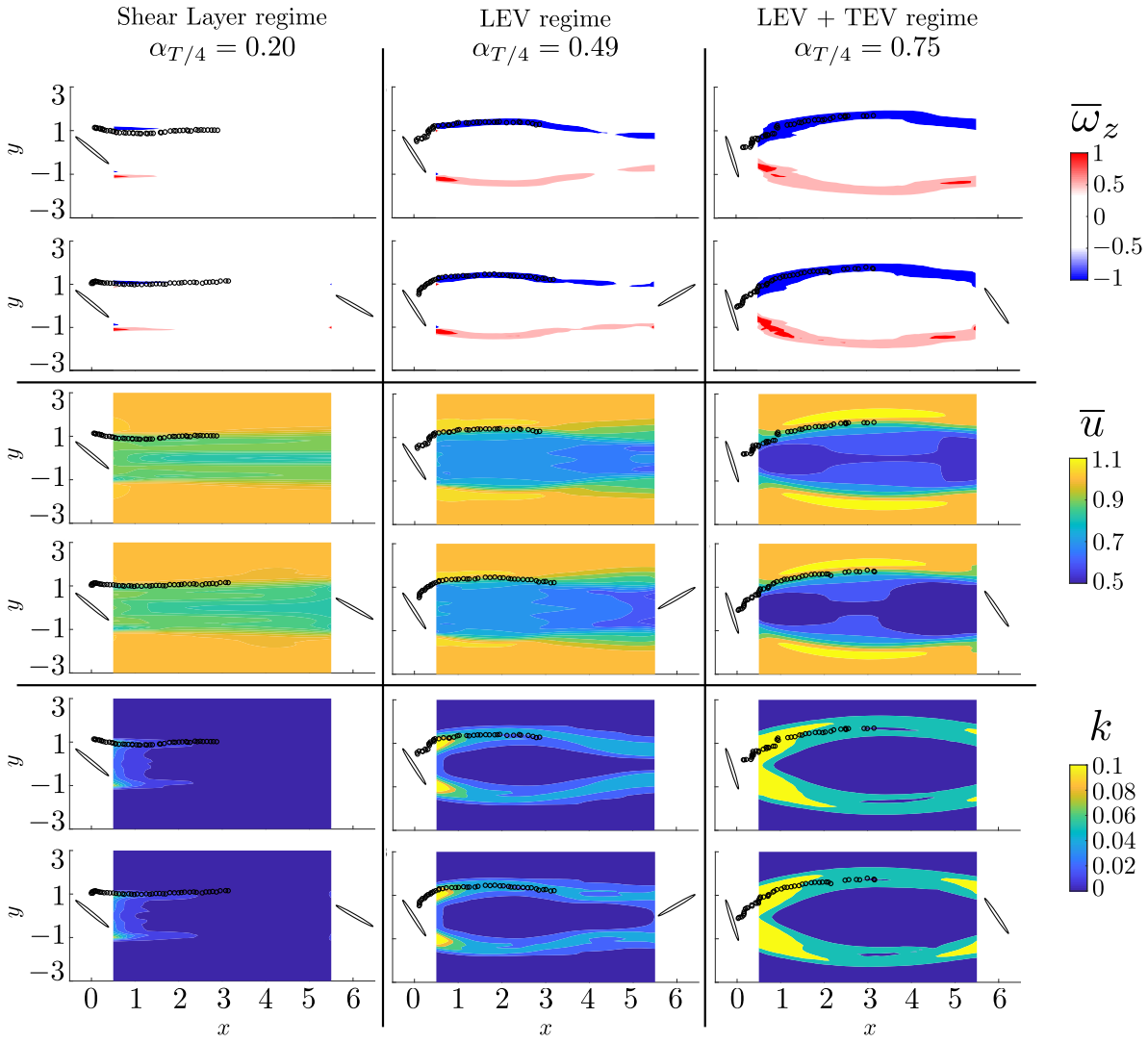

Figure 4.4: Time-averaged vorticity, $\overline{\omega}_z$, streamwise velocity, $\overline{u}$ and turbulent kinetic energy, k, for single and two-foil simulations with different $\alpha_{T/4}$ values for the three regimes. Black circles represent the path of the primary vortex shed during the foil's upstroke. Axes are nondimensionalized by the chord length c, and k by U_∞^2.

observed in regions after $x = 4$, which is within two chord lengths of the trailing foil. This impact that the trailing foil has on the wake is explained by the flow blockage and subsequent increase of pressure caused by the presence of the trailing foil.

Although the wake is similar between the single and two-foil simulations, the wake is significantly different among the three regimes. For the shear layer regime, the flow is more uniform in the x-direction compared to higher $\alpha_{T/4}$, which is a consequence of the low energy extraction of the leading foil, characteristic of foil kinematics of low $\alpha_{T/4}$. Consequently, the energy left in the wake is considerably higher compared to higher $\alpha_{T/4}$, which has a lower streamwise time-averaged velocity in Figure 4.4. The weak vortex formation at low $\alpha_{T/4}$ is consistent with the mean k field, which is negligible compared to that at higher $\alpha_{T/4}$. At higher $\alpha_{T/4}$, k concentrates in regions close to the leading foil, which correspond to the maximum strength of the vortices as they shed from the foil's surface. The vortices carve out a path of higher k compared to the bulk flow directly behind the foil, as also observed by Young et al. [73] at similar kinematics ($fc/U_\infty = 0.14; h_o = 1.00; \theta_o = 76.3°$). These streamwise time-averaged velocity and turbulent kinetic energy fields in the wake are used to quantify the energy available in the oncoming flow to the trailing foil.

In order to quantify the total kinetic energy in the wake, a wake width is defined. Figure 4.5 shows the non-dimensionalized wake deficit, defined as the difference between the freestream and the mean streamwise velocity downstream of the first foil, $1 - \overline{u}(x, y)$. The wake deficit is measured at $x = 1$ for the same three characteristic $\alpha_{T/4}$ values from Figure 4.4. The $y - z$ plane at $x = 1$ is chosen since it is close to the leading foil and assumed to be sufficiently far from any trailing foil interference. Data is interpolated from the simulations and discretized into 100 equally spaced points between $y = -2Y_p$ and $y = +2Y_p$.

Examining the profiles in Figure 4.5, three regions can be identified. Region '1' is defined as the wake deficit region as only positive wake deficit values ($U_\infty > \overline{u}$) are found. A stronger wake deficit is observed with increasing $\alpha_{T/4}$, in accordance with Figure 4.4. Region '2' shows negative wake deficit values ($\overline{u} > U_\infty$) at the same vertical location as

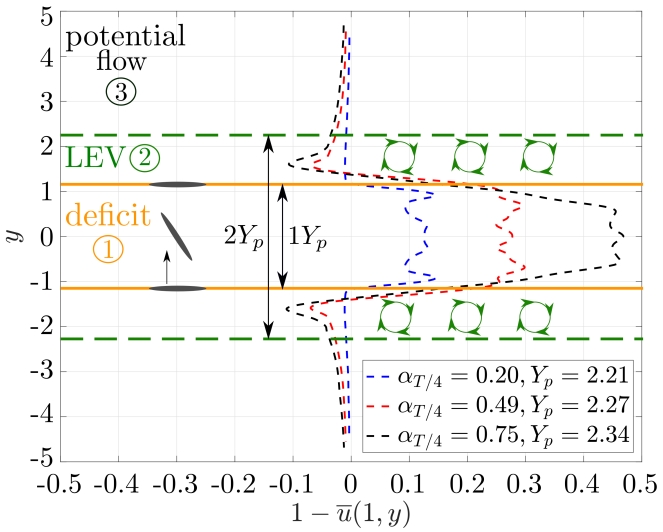

Figure 4.5: Wake deficit, $1 - \overline{u}(x, y)$, as measured at $x = 1$ for three different $\alpha_{T/4}$ values, representative of the shear layer, LEV and LEV+TEV regimes. The wake profile is divided into a pure deficit region, a LEV region, and a potential flow region. The orange lines roughly define the deficit region and represents $Y_p \approx 2.3$, close in value to the cases shown. A schematic of the foil motion in the $x - y$ plane is shown for reference. Chord length c is used to nondimensionalized the y-axis, and U_∞ is used to the x-axis.

the vortices shown by Figure 4.4. The stronger negative wake deficit corresponds with higher levels of k, likely indicating stronger vortices and increasing $\alpha_{T/4}$. Region '3' is characterized by the wake velocity approaching freestream velocity ($U_\infty \approx \overline{u}$). Since the freestream region is uniform, constant, and located far away from the foil, it can be approximated as irrotational and inviscid, and labelled as a potential flow region.

As highlighted in Figure 4.5, the width for regions '1' and '$1 + 2$' are approximately $1Y_p$ and $2Y_p$, respectively, where Y_p is the height of the swept area. The value of Y_p is highly correlated with the heave amplitude, but also slightly dependent on the pitch amplitude (see Figure 1.3). Based on this analysis, most of the energy in the wake is within an area defined by $y = -Y_p$ to $+Y_p$. Thus, an averaged wake velocity, $\overline{u}_p$, can be calculated at $x = 1$ by integrating the velocity deficit over this region,

$$\overline{u}_p = 1 - \frac{1}{2Y_p} \int_{-Y_p}^{+Y_p} 1 - \overline{u}(1, y)\, dy, \tag{4.3}$$

where $\overline{u}_p$ is nondimensionalized by U_∞. The mean turbulent kinetic energy over a specific $y-z$ plane, k_p, can be computed in the same manner,

$$k_p = \frac{1}{2Y_p}\int_{-Y_p}^{+Y_p} k(1,y)\ dy. \tag{4.4}$$

Applying Equations 4.3 and 4.4 to all kinematics for both experimental and numerical data, Figure 4.6 displays $\overline{u}_p$ and k_p with respect to $\alpha_{T/4}$. Similar to Figure 4.1, each point corresponds to the inter-foil phase with highest trailing foil performance.

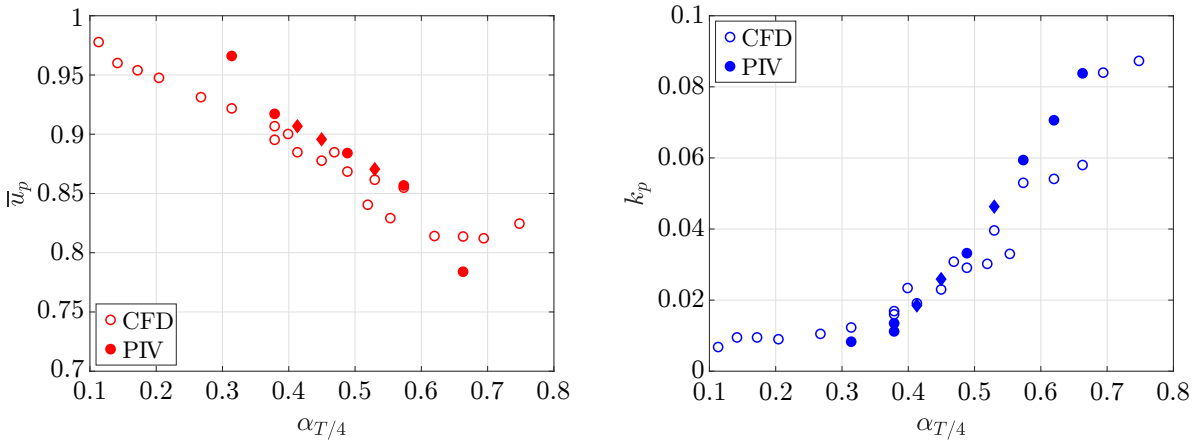

(a) $\overline{u}_p$ vs $\alpha_{T/4}$ (b) k_p vs $\alpha_{T/4}$

Figure 4.6: Mean wake velocity ($\overline{u}_p$) and turbulent kinetic energy (k_p) from numerical and PIV data. The diamond shape markers correspond to interpolated PIV data. The freestream velocity U_∞ is used to nondimensionalize $\overline{u}_p$ and k_p.

The wake velocity in Figure 4.6 has a roughly linear decay with respect to $\alpha_{T/4}$ until approximately $\alpha_{T/4} = 0.60$. Beyond this value, the wake velocity levels off around 0.82 for the available numerical data. The data from PIV is generally in agreement with CFD although its magnitude at the lowest and highest available $\alpha_{T/4}$ deviates from the CFD values by $+0.04$ and -0.03, respectively. The drop at $\alpha_{T/4} = 0.66$ can be partially explained by a limitation presented in the blockage correction method used on the experiments, which uses the measured C_d values from the experiments, which are very high at this angle of attack.

The turbulent kinetic energy also shows a strong agreement between numerical and PIV data. As opposed to the wake velocity, k_p remains constant at $k_p = 0.01$ and then increases with $\alpha_{T/4}$ until it appears to level off around $\alpha_{T/4} = 0.70$ at approximately $k_p = 0.09$. The increase of the turbulent kinetic energy as $\alpha_{T/4}$ increases is a consequence of the stronger wake vortices especially in the LEV+TEV regime ($\alpha_{T/4} > 0.50$). The higher efficiency of the leading foil in this regime compared to poor efficiency in the shear layer regime explains the decrease in wake velocity as more energy is extracted by the leading foil and hence the stronger wake deficit. This energy is mostly carried by the wake velocity since the energy per unit mass using the wake velocity ($\overline{u}_p^2$) is considerably higher than the turbulent kinetic energy. For instance, at $\alpha_{T/4} = 0.69$, $\overline{u}_p^2$ is approximately 7.5 times higher than the turbulent kinetic energy, k_p.

Combining foil kinematics and configuration parameters

In the previous section, Figure 4.6 demonstrated the steady and unsteady wake characteristics relative to the leading foil kinematics. Next, the relationship between the wake characteristics and the trailing foil performance is analyzed.

First, the trailing foil efficiency profiles are plotted with respect to the inter-foil phase for all cases, including all inter-foil distances. This information is split up into the three regimes, and shown in Figure 4.7. The curves with filled markers correspond to experimental data at equivalent foil kinematics with respect to the simulations. The light and dark green markers in Figure 4.7b correspond to simulations at $S_x = 4$ and $S_x = 5$, respectively. In contrast, the light and dark purple markers correspond to experiments at $S_x = 7$ and $S_x = 8$, respectively.

In Figure 4.7a, the maximum trailing foil efficiency achieved in the shear layer regime is approximately 7%, whereas for the other two regimes, the trailing foil reaches 15% at optimal inter-foil phase. For the two lowest $\alpha_{T/4}$ values in the shear layer regime, efficiency is close or lower than 0 at almost any inter-foil phase, which is explained by the kinematics

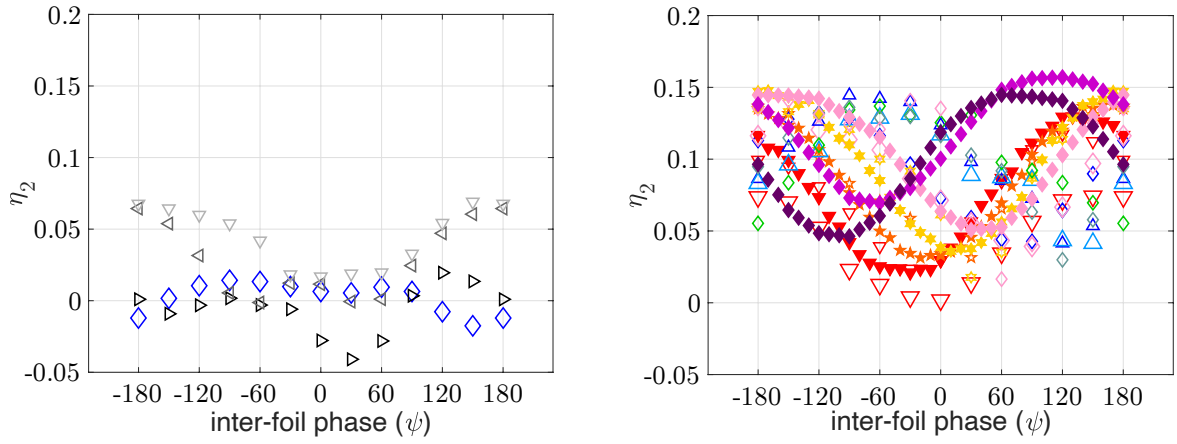

(a) Shear Layer regime

(b) LEV regime

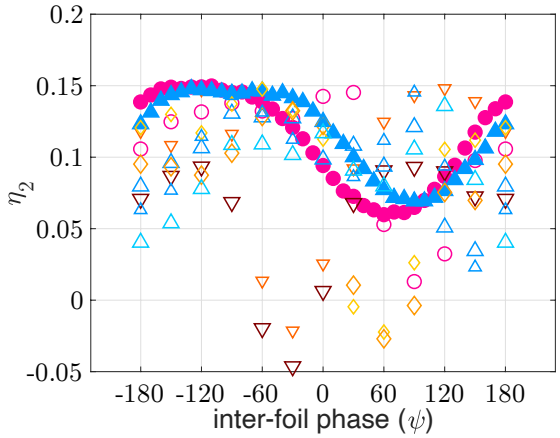

(c) LEV+TEV regime

Figure 4.7: Trailing foil efficiency, η_2, with respect to inter-foil phase, ψ. Open symbols represent the numerical data, whereas filled ones represent experimental data. Each curve represents a set of kinematics as defined in Table 2.1.

being far from optimal within the energy harvesting range. With the combination of high reduced frequency and low pitch there is very little flow separation and the vortices roll up along the trailing edge at stroke reversal.

At $\alpha_{T/4} = 0.20$, efficiency reaches 7% at the optimal inter-foil phase. Examination of the flow fields indicates that this is a consequence of the trailing foil avoiding the path of shear layer vortices emitted from each half-stroke of the leading foil, as highlighted in Figure 4.3. At this $\alpha_{T/4}$ value, three pairs of clockwise and counter-clockwise vortices shed per half-stroke, each with low strength compared with kinematics at higher $\alpha_{T/4}$. The small

and weak vortices follow a horizontal path as shown in Figure 4.4, and are convected in the same direction as the freestream velocity. Nonetheless, even for the small vortices in this regime, interactions between the primary vortices and trailing foil affects trailing foil's efficiency. The impact on trailing foil efficiency depends on the strength of the vortices and the timing, as a slight shift in inter-foil phase may cause a vortex to directly impinge upon the trailing foil or miss it completely. The timing between the interaction of primary vortices and trailing foil is also described in Kinsey and Dumas [74] and it is a key feature for the slightly higher efficiency at the optimal inter-foil phase for both $\alpha_{T/4} = 0.17$ and 0.20. For lower $\alpha_{T/4}$ within the shear layer regime, the flow separation is less dramatic and hence the trailing foil is less susceptible to increase or decrease in the energy extraction from the oncoming flow. Consequently, the efficiency is roughly constant throughout the inter-foil phases.

The LEV and LEV+TEV regimes both display a sinusoidal-like profile for the trailing foil efficiency as a function of phase angle. However, there is a significant difference between these two regimes. The LEV regime contains kinematics that generate stronger vortices compared to the shear layer regime (see Figure 4.3). As opposed to the lowest $\alpha_{T/4}$ cases, the path of the recently shed vortices start to separate from the previous half-stroke vortices of opposite sign. Another feature of the LEV regime is the vortex pattern of one pair and two single vortices that shed per half-stroke. The stronger vortices have a larger convective speed, which impact the interaction timing between the primary vortex and trailing foil. For instance, for the kinematics highlighted on the shear layer regime on Figure 4.3, the primary vortex reaches $x = 4$ at approximately $t/T = 1.00$. The primary vortex for the case shown in the LEV regime reaches same position at $t/T = 0.95$ and this values drops to $t/T = 0.75$ for the LEV+TEV regime. The result is that the efficiency variation is more dramatic, and appears very close to sinusoidal with respect to inter-foil phase.

In contrast, in Figure 4.3 the LEV+TEV regime shows a clear separation between the current half-stroke and the previous half-stroke of opposite signed vortices. The strength of

the primary vortex pair and the four single secondary vortices that shed per half-stroke are significantly higher for this final regime compared to the LEV regime, and hence creates a more chaotic relationship between efficiency and inter-foil phase as observed on regions close to $\psi = 0°$. In particular, there is a sharp efficiency drop around $\psi = 0°$, even briefly dropping below the energy harvesting threshold for some kinematics. This break in the sinusoidal trend is explained by the unpredictable interaction of trailing foil with the oncoming flow that includes stronger secondary vortices from the leading foil. The higher convective speed presented in this final regime also has a major role in the sharp efficiency drop. Thus, the LEV+TEV regime has a larger efficiency range from -5% to 15% compared to the $0\% - 15\%$ from the LEV regime.

Although information can be extracted from Figure 4.7, there is no clear efficiency trend with respect to the inter-foil phase especially in the range from $\psi = -120°$ to $\psi = 120°$, as it is compounded by the effect of kinematics and inter-foil distance. Instead of using inter-foil phase, a key variable to establish the relationship between the wake and trailing foil performance is the 'wake phase', Φ, defined as

$$\Phi = 2\pi \frac{S_x}{\overline{u}_p} f^* + \psi \tag{4.5}$$

with $f^* = \frac{fc}{U_\infty}$. The 'wake phase' is a modification from the originally implemented global phase model proposed by Kinsey and Dumas [74] and this model describes the phase shift between the wake trajectories of both foils considering both wakes being convected at the freestream velocity. The difference between the 'wake phase' and the 'global phase' parameters is the use of $\overline{u}_p$ instead of freestream velocity, which more accurately describes the mean flow speed between the two foils, especially for medium to high $\alpha_{T/4}$ cases, where the wake deficit is more apparent.

Kinsey and Dumas observed that their original global phase model does not provide any information on the relative angle of attack and the related occurrence of flow separation. However, the proposed wake phase model incorporates the streamwise velocity of the

wake which subsequently correlates with the leading foil kinematics, and $\alpha_{T/4}$, as shown in Figure 4.6. However, the highly variable vortex dynamics observed throughout the range of kinematics means that the interactions with the trailing foil can again be divided into three regimes. Figure 4.8 organizes the trailing foil efficiency with respect to the wake phase for all kinematics within each regime.

For the shear layer regime in Figure 4.8a, the wake phase model attempts to align the variation in efficiency across the various inter-foil phase angles for the four sets of kinematics tested numerically. By incorporating the reduced frequency and measured wake velocity in the model, the lowest efficiency is between $\Phi = 0^\circ$ and $\Phi = 60^\circ$. The two highest $\alpha_{T/4}$ cases of this regime have their minimum efficiency around $\Phi = 0^\circ$ and the maximum efficiency at approximately 7%.

The LEV regime in Figure 4.8b demonstrates a strong collapse of trailing foil efficiency with respect to the wake phase. A roughly sinusoidal trend is formed with the minimum around $\Phi = 0^\circ$, and the maximum around $\Phi = 120^\circ$. The maximum efficiency peaks between 10% to 15% with a single case with maximum efficiency around 7%, and generally increases as $\alpha_{T/4}$ increases. The experiments and simulations show strong agreement for this regime.

For the third regime in Figure 4.8c, representing the highest $\alpha_{T/4}$ values, the wake phase model also shows a minimum efficiency at approximately $\Phi = 0^\circ$. The efficiency range is from 7% to 15% on wake phases close to 180°, similar to the LEV regime, but efficiency is from -5% to 15% on wake phase near $\Phi = 0^\circ$. The two highest $\alpha_{T/4}$ show an efficiency increase around $\Phi = 0^\circ$. Compared to Figure 4.7c, the wake phase model in Figure 4.8c demonstrates a partial collapse of the efficiency profiles bringing the minimum efficiency of each case closer to $\Phi = 0^\circ$.

In contrast, the experimental data in Figure 4.8c still show a similar sinusoidal behavior to the LEV regime in Figure 4.8b, but with a plateau around the maximum efficiency between $\Phi = 70^\circ - 180^\circ$. The stark differences between various kinematics, and between

the experimental and numerical data, highlight the strong influence of the LEV and TEV within this regime. In particular, the strong TEV formation increases the wake disturbance and vortex dynamics more so than the other two regimes. Through analyzing the flow fields in each regime as exemplified in Figure 4.3, it is found that the numerical data have more concentrated vortices than the experiments of similar angles of attack. This is likely a result of different Reynolds numbers and the three-dimensional effects that are inevitable in experiments and are not captured in the simulations.

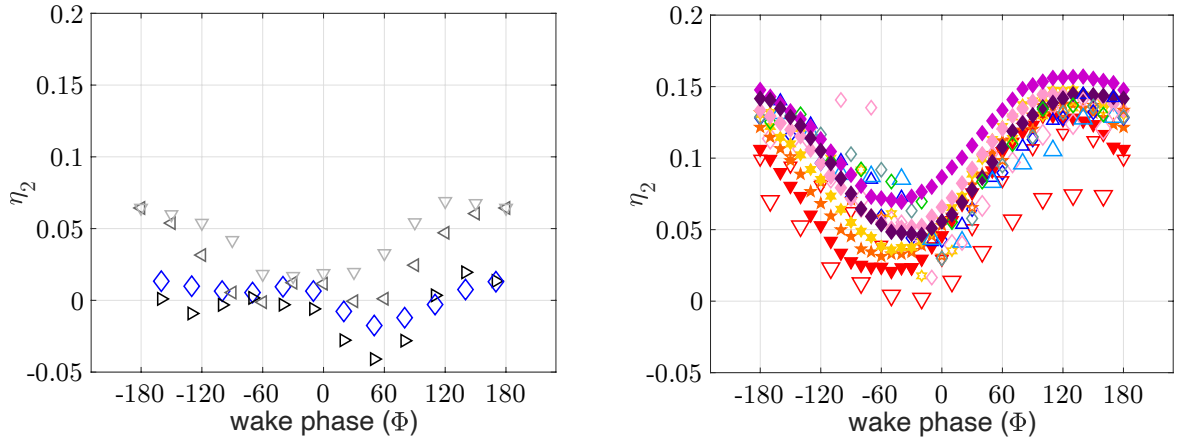

(a) Shear Layer regime

(b) LEV regime

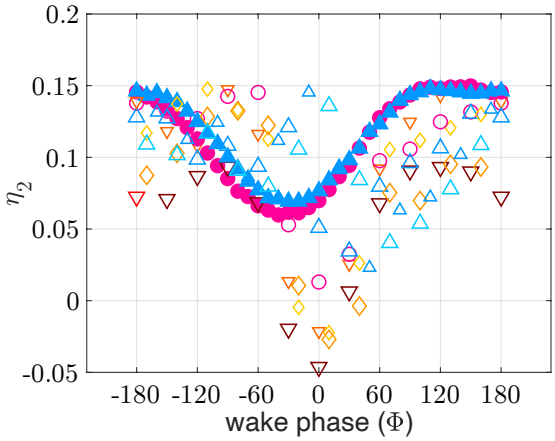

(c) LEV+TEV regime

Figure 4.8: Trailing foil efficiency (η_2) regimes using the wake phase model. Φ is in degrees. Open symbols stands for numerical data, whereas filled ones are experimental data. Each curve represents a set of kinematics as defined in Table 2.1.

In terms of the primary vortex position when it impinges on the trailing foil in an

upstroke motion, Kinsey and Dumas defined four configurations that affect the pressure field around the foil. Two configurations are favorable for power extraction and these occur when the counter-clockwise vortex impinges on the suction side of the foil or a clockwise vortex impinges on the pressure side of the foil. The two unfavorable conditions occur when vortices with signs opposite to each of the above mentioned configuration impinges on the trailing foil.

Kinsey and Dumas also found a strong interaction between the primary vortex and the trailing foil at kinematics of $fc/U_\infty = 0.14; h_o = 1.00; \theta_o = 70°$, which has a $\alpha_{T/4} = 0.50$, a borderline case between the LEV and LEV+TEV regimes. For this case at limited inter-foil phases, they obtained an optimal global phase of $90°$, which is different than the optimal wake phase of $120°$ obtained in the LEV regime. However, the foil kinematics and configurations from Kinsey and Dumas only explored two inter-foil phases, $-90°, -180°$, as well as small variations in the heave and pitch amplitudes compared to the current data.

With a considerably higher parameter variation, the original global phase model is applied to the current data (see Appendix B) to check its performance among regimes in terms of efficiency trends and optimal global phases. The predictions between models is particularly different within the LEV regime, with the global phase model not being able to present as clear of an efficiency trend as the wake phase model. This can be explained by the wake phase model incorporating the mean streamwise wake velocity.

With the sinusoidal efficiency profile in the LEV regime, the wake phase model can be used to predict the efficiency depending only on the leading foil kinematics. For instance, at $\alpha_{T/4} = 0.40$ and $\Phi = -60°$, the trailing foil efficiency should be within $1\% < \eta < 10\%$. This prediction is insightful to obtain optimal configurations for better energy harvesting. For example, a trailing foil efficiency of 15% is obtained for a wake phase of $-180°$ and a case with $\alpha_{T/4} = 0.49$. Therefore, the same efficiency could be obtained with any set of reduced frequency, heave and pitch amplitude as long as it provides the same $\alpha_{T/4}$ and wake phase. Kinsey and Dumas highlighted the prediction ability of their global phase model but they

found it reliable only between cases sharing the same wake profiles or similar $\alpha_{T/4}$. The approach of dividing the wake into regimes makes prediction more feasible across regimes.

4.3 Conclusion

The wake structure and dynamics on a two-foil array is explored in a wide range of kinematics and configurations, both computationally and experimentally. The goal of this chapter is to quantify the effects between foil kinematics and the wake behind the leading foil in terms of vortex structure and flow velocity, and use this information to model the trailing foil's performance.

Through an analysis of the primary vortex strength shed from the leading foil, three main regimes are defined and characterized based on their kinematics ($\alpha_{T/4}$), vortex strength, and wake structure. The 'shear layer' regime occurs at low $\alpha_{T/4}$ ($\alpha_{T/4} \leq 0.20$) and the wake region is dominated by a shear layer and contains very weak vortex formations. The 'LEV' regime ($0.20 < \alpha_{T/4} \leq 0.49$) contains a primary LEV that sheds at each half-stroke forming a path of shed vortices that are distanced from the previous half-stroke vortices of opposite sign. This is more dramatic in the third and final regime, 'LEV+TEV' ($0.49 < \alpha_{T/4} \leq 0.75$), in which the development of a large TEV further influences the wake structure.

The efficiency of the second foil is a function of the inter-foil distance and inter-foil phase angle, as well as the baseline kinematics of the foils. Within the LEV regime, the efficiency is roughly sinusoidal with respect to inter-foil phase angle. This sinusoidal behavior begins to develop in the shear layer regime but occurs to a lesser extent. At the high $\alpha_{T/4}$ of the 'LEV+TEV' regime, the sinusoidal trend is not sustainable for all kinematics due to the more unpredictable wake patterns from the TEV. When selecting the optimal inter-foil phase, the efficiency of the second foil gradually increases with $\alpha_{T/4}$, leveling off at approximately 15% in the LEV regime at approximately $\alpha_{T/4} = 0.40$.

Building off the global phase model proposed by Kinsey and Dumas [74], a wake phase model is introduced to better predict the trailing foil efficiency based on kinematics and inter-foil configurations. The model shows good agreement with the data for the LEV regime, when the wake structure is more predictable, and the experimental and numerical data collapse nicely. The wake phase model is less successful in predicting the efficiency for the shear layer regime in which the kinematics do not produce consistently strong vortices, or the LEV+TEV regime in which the number of vortices increases to the point where the wake is too chaotic. Although the results shown are for the same kinematics applied on both foils, the wake phase model can be used for distinct kinematics between foils since the model is independent of the trailing kinematics.

5 Classification and Clustering of Vortex Wake Modes

5.1 Background and motivation

Chapter 4 demonstrated the importance of considering the unsteady flow effects to more accurately represent the kinetic energy in the wake and therefore update trailing foil efficiency. However, a relationship between foil kinematics and the wake is still missing and by understanding how the kinematics are associated with wake structure, predictive models of array configurations, kinematics, and performance can be constructed. As introduced in section 1.4, convolutional autoencoders and LSTM have been successful in predicting unsteady flows. Rather than predicting structures, the purpose of this chapter is to combine these two techniques towards classification and clustering of flow fields and find wake patterns from different leading foil kinematics.

Classification models have been implemented in oscillating foil propulsion [75,76] and behind cylinders [77], which have shown to be successful on classifying wakes from point-measurements or from the foil's kinematics. In contrast, the goal of this chapter is to classify vortex wake structures solely based on images, or vorticity flow fields, and correlate the classes with oscillating foil kinematics for energy harvesting. Using two-dimensional direct numerical simulations (DNS), Ribeiro et al. [78] defined three modes for vortex wakes by measuring the strength of the first vortex shed from the suction side of the oscillating foil each half-stroke, as also discussed in chapter 4, but did not consider the entire wake structure.

In contrast from classification models, clustering algorithms reside in a larger group called unsupervised learning, which task implies the extraction of features from the data

by specifying certain global criteria, without the need for supervision or a ground-truth label for the results [45].

This chapter develops a classification model based on convolutional layers and LSTM units, which is applied on wake structures captured by the spanwise vorticity among a wide range of 46 foil kinematics for energy harvesting. Using visually labeled groups from Ribeiro et al. [78], the classification model assesses if these groups are correctly divided or need adjustment based on the prediction accuracy of the model. Furthermore, a clustering model originally developed and tuned by Calvet et al. [51] checks how foil kinematics are correlated with images of the wake and combining with the prediction accuracy of the classification model, an update on group boundaries in the classification model is performed.

5.2 Initial Class Selection

The kinematics outlined in Table 2.1 cover a large parameter space, which contributes to a range of energy harvesting modes, which range in efficiency from close to zero up to 30%. These results demonstrate that the optimal performance is not strongly correlated with a single set of foil kinematics. As displayed in Figure 5.1a high energy harvesting efficiency is found within the range $f^* = 0.12 - 0.15; \theta_o = 65^\circ - 80^\circ; h_o^* = 0.50 - 1.00$ with no clear correlation with a single kinematic parameter. Thus, it is convenient to reduce the parameter space into a single and representative variable, $\alpha_{T/4}$, the characteristic relative angle of attack as defined in Equation 2.4, which allows foil efficiency to be expressed as a simpler function of foil kinematics as shown in Figure 5.1b [17]. The efficiency increases monotonically until $\alpha_{T/4} \approx 28.0^\circ$ and then varies for higher $\alpha_{T/4}$ values due to a high degree of flow separation [44,78].

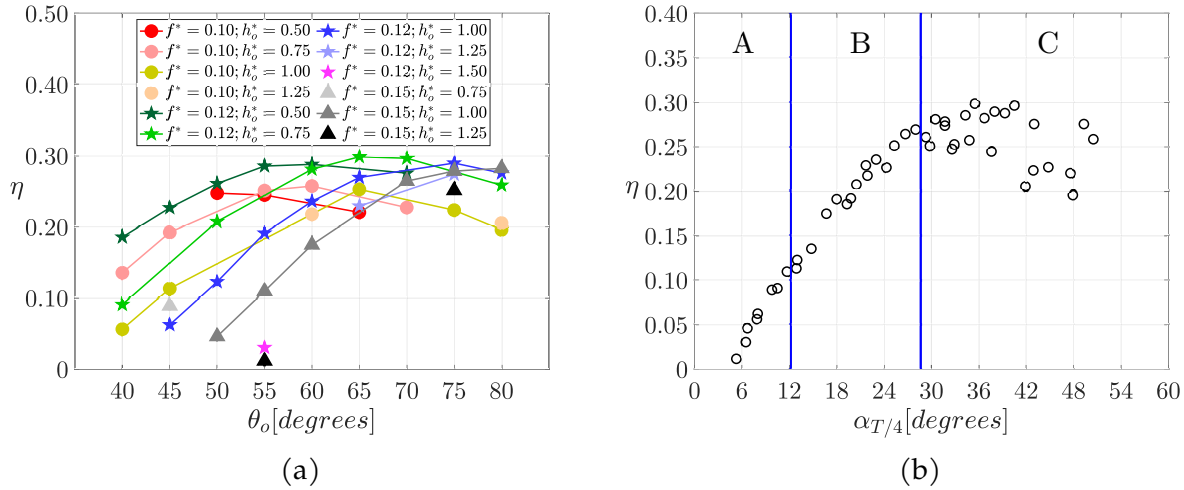

(a) (b)

Figure 5.1: (a) Energy harvesting efficiency, η, as a function of pitch amplitude, θ_o (in degrees) for various reduced frequency (f^*) and heave amplitude (h_o^*) pairs; (b) Efficiency with respect to $\alpha_{T/4}$. Vertical lines indicate initial grouping of vortex wake structures based on primary vortex strength analysis.

To correlate $\alpha_{T/4}$ with the flow structures that emanate from the foil, Ribeiro et al. [78] defined three classes labeled A ($5.3° \leq \alpha_{T/4} \leq 11.7°$), B ($11.7° < \alpha_{T/4} < 29.3°$) and C ($29.3° \leq \alpha_{T/4} \leq 50.5°$) using the maximum strength of the primary vortex formed for each kinematics (as demonstrated in Figure 5.1b). The wake structures that emerge from the three classes are displayed in Figure 5.2 within a $7.5c$ by $7.5c$ window located downstream, and general trends based on vortex strength are extracted from these wakes. Class A contains weak vortices as represented by a shear layer in the majority of images in this class. In contrast, class C displays the strongest and most coherent vortices compared with the other classes. Class B has a mix of kinematics with stronger vortices than class A but weaker than class C.

Observing the wake structures from Figure 5.2, trends are found within and between classes. With an increase in pitch amplitude, vortices shed from the foil increase in size and strength with frequency and heave amplitude $f^* = 0.12; h_o^* = 0.50$ (see kinematics highlighted in red). With an increase in reduced frequency, the wake wavelength is smaller as displayed by the kinematics with $h_o^* = 1.25, \theta_o = 75°$ (see kinematics in green).

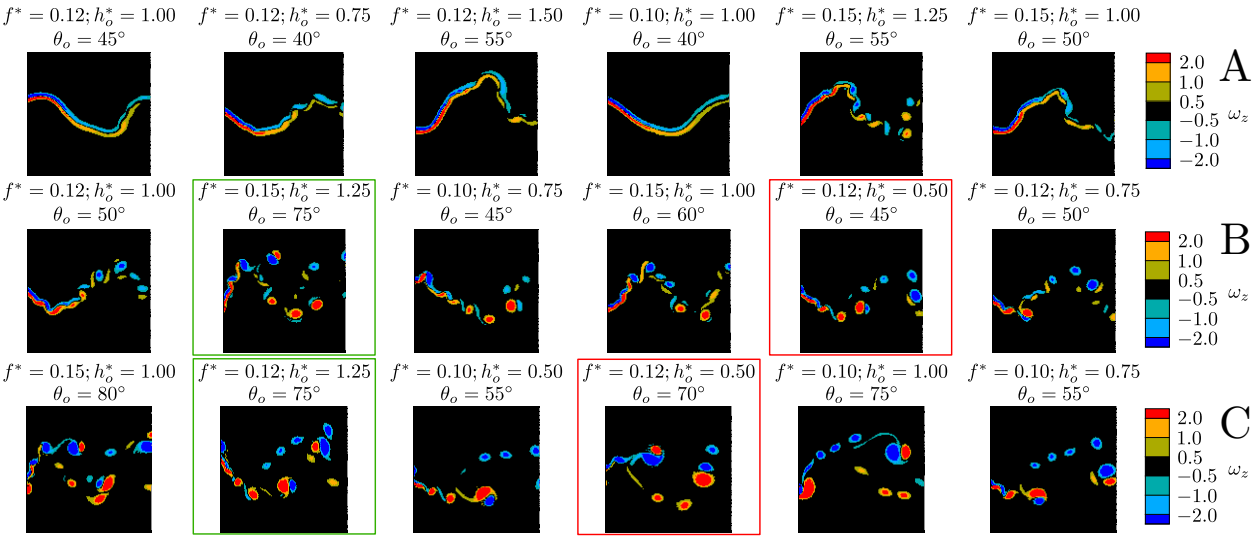

Figure 5.2: Randomly selected images of wake structures from each class highlighted in Figure 5.1b. The colored boxes outline wake features found when one foil parameter is varied while others remain constant.

5.3 Supervised Classification

In this Section, the wake is analyzed through an image-based supervised learning algorithm, where classes are defined based on the predetermined groupings motivated in Section 5.2.

Data Pre-Processing

The input to the classification model are images of 2D spanwise vorticity extracted from a $7.5c$ by $7.5c$ window located in the wake and interpolated onto a cartesian grid of 128 by 128 pixels as illustrated in Figure 5.3. The window size is selected such that it contains all vortices shed from the foil in the y-direction in all kinematics from Table 2.1 and $7.5c$ corresponds to a typical inter-foil spacing in foil-arrays under the energy harvesting regime. For each set of kinematics, three oscillation cycles within the steady state regime are used as input with data sampled at every $tU_\infty/c = 0.1$, for a total of $11,846$ samples. The fixed sampling rate is used in order to maintain the difference between consecutive wake images independent of the foil's reduced frequency, thus the number of samples differs for each

frequency. Contour levels of vorticity are chosen to display the wake structures in all kinematics, and six levels $(-2, -1, -0.5, 0.5, 1, 2)$ are consistently drawn for each wake image as shown in Figure 5.3.

Since the vortices shed from the foil may affect each other's trajectory [33,78,79], the time evolution is considered in the classification neural network through the use of LSTM units. A sequence of five images is given as the input data, which provided higher accuracy compared with a sequence of ten images. To avoid overfitting, a data augmentation technique is also implemented, which duplicated the number of samples from $11,846$ to $23,692$. This technique not only took an input sequence at consecutive $0.1tU_\infty/c$ units, but also with $0.1tU_\infty/c$ skipped between samples, i.e. $0.1, 0.3, 0.5, 0.7, 0.9tU_\infty/c$, following a similar strategy by Chong and Tay [80].

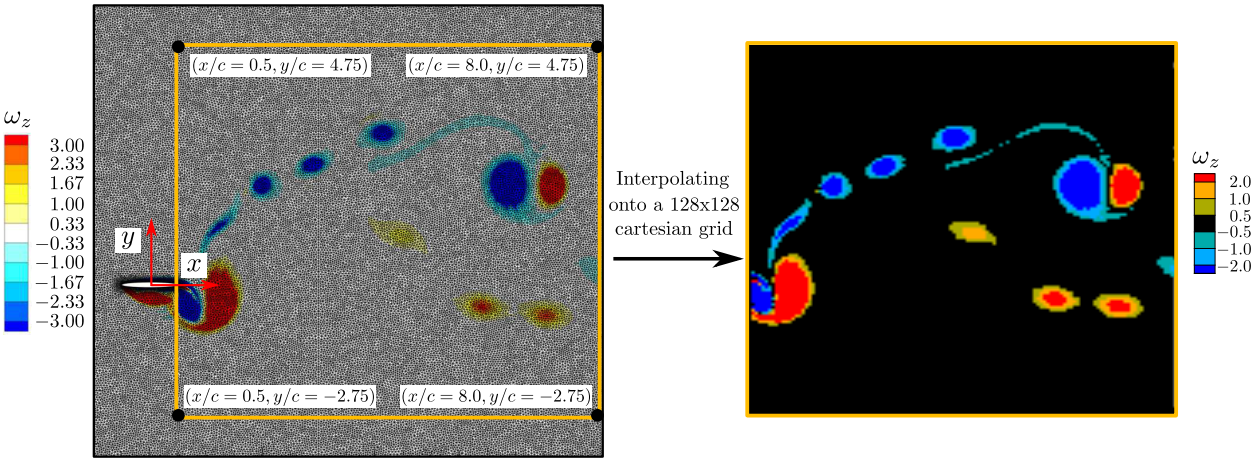

Figure 5.3: Data pre-processing for the classification model interpolates the spanwise vorticity computed with high resolution computational data onto a 128x128 grid for a fixed region behind the foil at every 0.1 convective time units.

Classification Model Architecture

Using the Python based libraries TensorFlow [81] and Keras [82], the classification model is built from a combination of convolutional layers, LSTM units and dense layers, as outlined in Figure 5.4. The 2D convolutional layers (*Conv2D*) are applied on each sample to extract the most significant features of the wake. These key features are detected with filters, which

create feature maps through a convolutional operation on the preceding layer [51]. Each convolutional layer uses a linear activation function with multiple filters of fixed kernel size, 3×3, that reduces the matrix dimensions while simultaneously keeping the most pertinent features. The number of feature maps define the depth of each convolutional layer and within each layer, a downsample operation is performed with a 2×2 stride, resulting in a reduction factor of 2 in each matrix dimension while the depth remains constant. Each input sequence passes through four convolutional layers, decreasing the dimension of each sample from $128 \times 128 \times 1$ to an 8×8 feature map with eight channels.

Each sample is then flattened into a 1D vector with 512 elements where 90 LSTM units analyze the correlation between each wake image within the input sequence, with the goal of detecting patterns between each wake structure and its time evolution behind each foil configuration. The final section of the model contains a dropout layer of rate equal to 0.1 that is placed between two dense layers in order to decrease overfitting. The dense layers classify each image according to the predetermined classes. The first layer contains 90 neurons and the second dense layer has three neurons corresponding to class A, B or C. Both dense layers use a sigmoid activation function to normalize the output from the previous layer into a $0 - 1$ range. To update the neural network weights, the Adam optimization algorithm [83] is implemented in the model. To prevent overfitting, the early stopping technique [84] with 100 training epochs is utilized.

The following hyperparameters in the classification model are tuned: number of filters in the convolutional layers, LSTM units, and number of neurons in the first dense layer. The sequences of $(64, 32, 16, 8)$, $(32, 16, 8, 4)$, $(128, 64, 32, 16)$ filters for the convolutional layers are tested and $(64, 32, 16, 8)$ obtained best performance. The LSTM units and number of neurons in the first dense layer are tuned using a range from $20 - 100$ units and neurons and it is found that 90 units and 90 neurons provided a higher model accuracy.

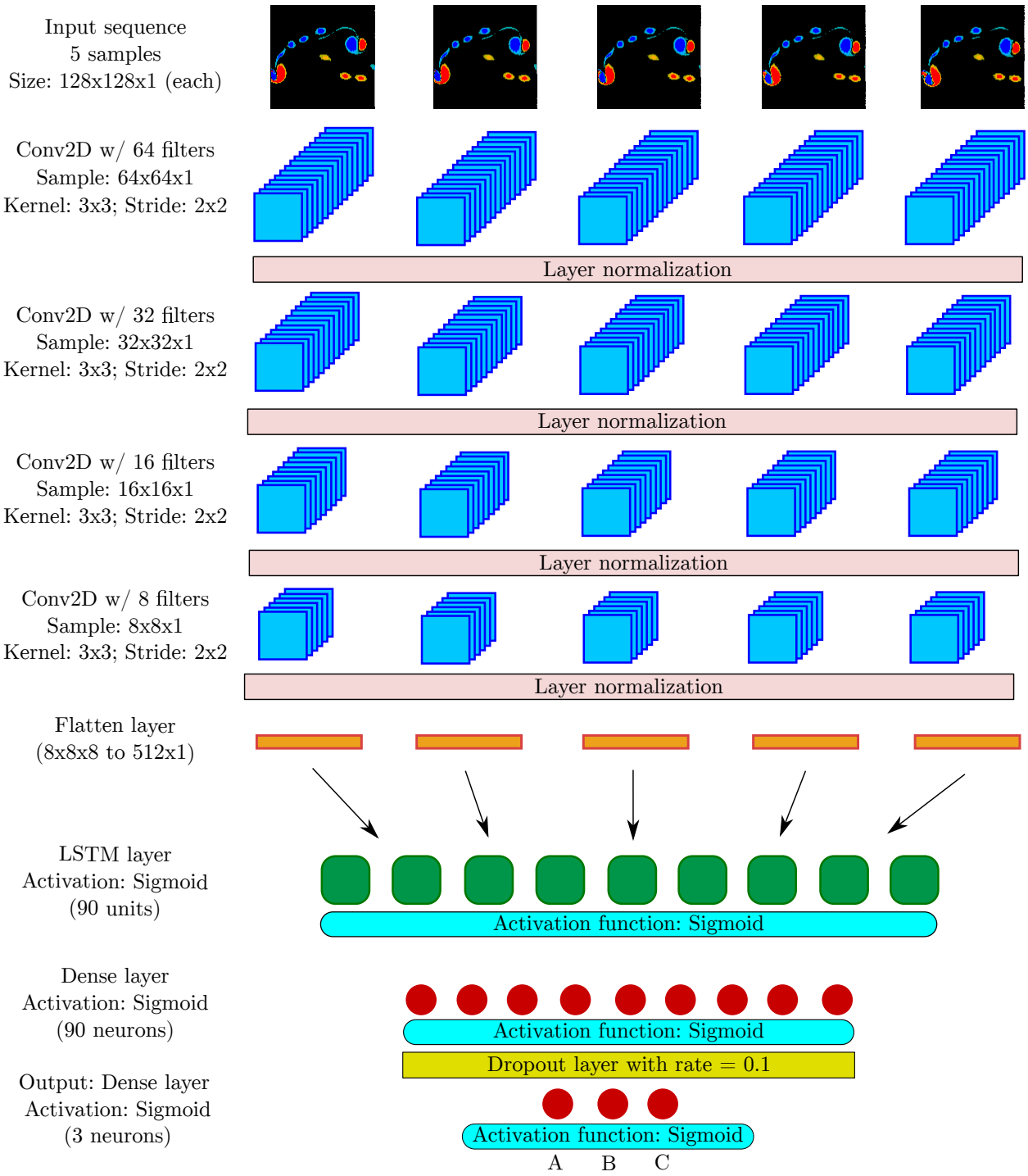

Figure 5.4: Classification model architecture.

5.4 Unsupervised Clustering Methodology

The classification model presented in section 5.3 divides the wake kinematics into three classes predetermined by the researcher (based on prior vortex analysis). In this section, an unsupervised algorithm is utilized to group similar wake kinematics, and the clusters are subsequently compared with the classes from the supervised model. The unsupervised clustering groups the vortex images, individually, without any prior knowledge or relationship between wake kinematics and the respective wake structures. Therefore, the clusters obtained through this method will assist in verifying the classification results and potentially modifying the class boundaries determined by the researcher.

The model architecture follows closely from the CAE clustering algorithm by Calvet et al. [51], including the same number of convolutional layers, filter and skip connections. The architecture consists of an autoencoder with five sequences of convolutional and max-pooling layers for the encoder portion. For the decoder portion, five sequences of convolutional and up sampling layers are used. The only hyperparameter retuned is the batch size, in which an online learning method (batch size equals to 1), is implemented within the autoencoder. With this algorithm there is no prelabeling of images, but the user must determine the number of clusters, which is explained below.

The input data is the same vorticity images described in section 5.3, except that there are no time sequences provided, and therefore each instantaneous wake image is treated independently. This results in $11,846$ unique samples from 46 simulations with the foil kinematics outlined in table 2.1.

A combination of the elbow and the silhouette score methods are utilized to determine the optimal number clusters for the provided samples, following the approach from Calvet et al. [51]. The elbow method [85] computes the total within-cluster sum of square error, known as distortion, and the number closer to the 'elbow' of the curve is the indicator of the approximate number of clusters that best separates the data. The silhouette score method [86] determines how well each image lies within its cluster by estimating cohesion

(intra-class) and separation (inter-class) as Euclidean distances. The score is a combination of both factors, and ranges from zero to one, where a higher score indicates better clustering. After using those score methods, the optimal number of clusters is found to be four.

Updating Class Boundaries Using the Clustering Results

The results of four clusters are displayed in Figure 5.5a. Every cluster is roughly defined within an $\alpha_{T/4}$ range, which is consistent with the results from the supervised model that also utilized $\alpha_{T/4}$ as the preferential kinematic parameter. The clustering division of four clusters, rather than three, naturally imposes a new boundary and introduces small shifts in the other two cluster boundaries. These new divisions are explored by utilizing the previously described classification algorithm in the following manner.

For instance, the cluster A groups foil kinematics in the range of $\alpha_{T/4} \leq 14.8^{\circ}$ (Figure 5.5a), whereas the previous class A included kinematics with $\alpha_{T/4} \leq 11.7^{\circ}$. The proposed clustering division is implemented within the classification algorithm previously described (with the five-fold cross-validation). The results were less accurate, indicating that the classification algorithm can more reliably group images when the boundary is closer to $\alpha_{T/4} \leq 11.7^{\circ}$.

Similar tests are performed on the remaining two cluster-informed divisions at $\alpha_{T/4} = 24.3^{\circ}$ and $\alpha_{T/4} = 31.7^{\circ}$. The results indicate that shifting both these boundaries to slightly lower $\alpha_{T/4}$ reveals more accurate classification of images. These results inform the update on the class boundaries as proposed by the orange solid lines in Figure 5.5b, which are contrasted with the original classifications from section 5.3 (dashed blue lines). The orange shaded regions next to each boundary represent the mismatch between the class and cluster boundaries.

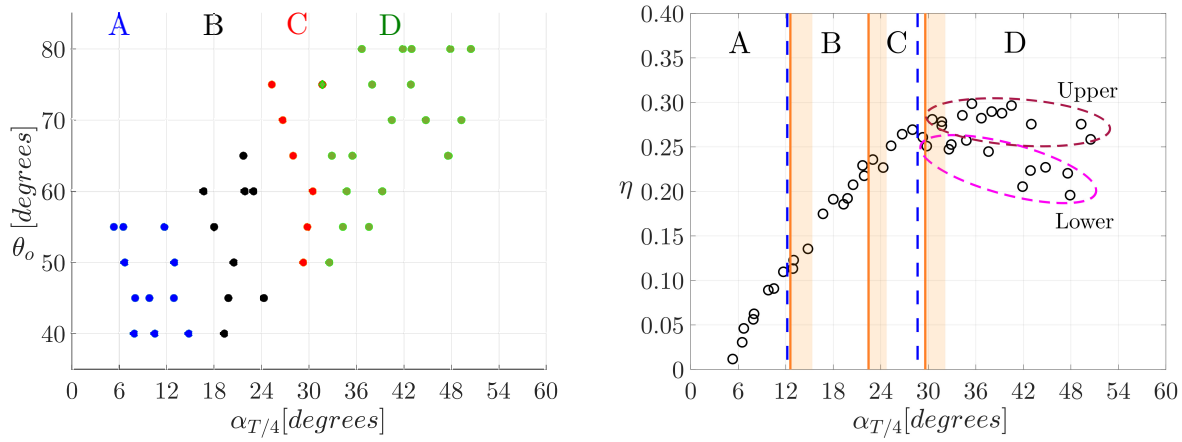

Figure 5.5: (a) Clustering results represented by each foil kinematics as a data point: two kinematics with $\alpha_{T/4} = 31.7°$ and $\theta_o = 75°$ represented by a red circle and a green diamond placed in clusters C and D, respectively; (b) Updated class divisions (orange solid lines) compared with original groupings (blue dashed lines) along with the mismatch between class and cluster boundaries (orange shaded regions).

To summarize, when four classes are defined, the highest classification accuracy is obtained when the class boundaries are placed at $\alpha_{T/4} = 11.7°$, $\alpha_{T/4} = 23.0°$ and $\alpha_{T/4} = 29.3°$ (orange lines from Figure 5.5b). The results of these tests reveal that the accuracy is just as good as the original three classes, with an average fold accuracy of 91%. Furthermore, mismatched labels only occur close to the boundary divisions. For instance, 100% of the samples from class A in Folds 1 and 2 have a label match between predicted and prelabelled, with the same occurring in Fold 4 for classes B and C. For Fold 1, only the foil kinematics with $\alpha_{T/4} = 28.0°$ is mislabelled between classes C and D, which can be explained by the proximity of this kinematics to its neighboring class. All other arrangements of class boundaries that are tested yield an average accuracy lower than 91%.

The four updated classes offer new physical insight on wake patterns, illustrated in Figure 5.6. Each row highlights wake images at different foil positions that are randomly selected from various kinematics within each class. In class A ($5.3° \leq \alpha_{T/4} \leq 11.7°$), the foil generates a shear layer wake pattern as noticed by the absence of coherent vortices in the wake, and as previously described in Section 5.2. Although classes B ($11.7° < \alpha_{T/4} < 23.0°$)

and C ($23.0° \leq \alpha_{T/4} \leq 29.3°$) contain stronger vortices, the wake path is considerably different, with class B showing a longer wavelength within the selected wake window compared to class C (see yellow and red lines), which is a feature not previously captured by the original class divisions. Class D ($29.3° < \alpha_{T/4} \leq 50.5°$) contains kinematics where the foil generates the largest number and strongest coherent vortices, as shown by the presence of a strong primary LEV in the majority of wake images (see green circle). These differences in the wavelength among wake patterns emphasize the criteria used in unsupervised clustering to differentiate each regime which are not captured by the initial classification approach.

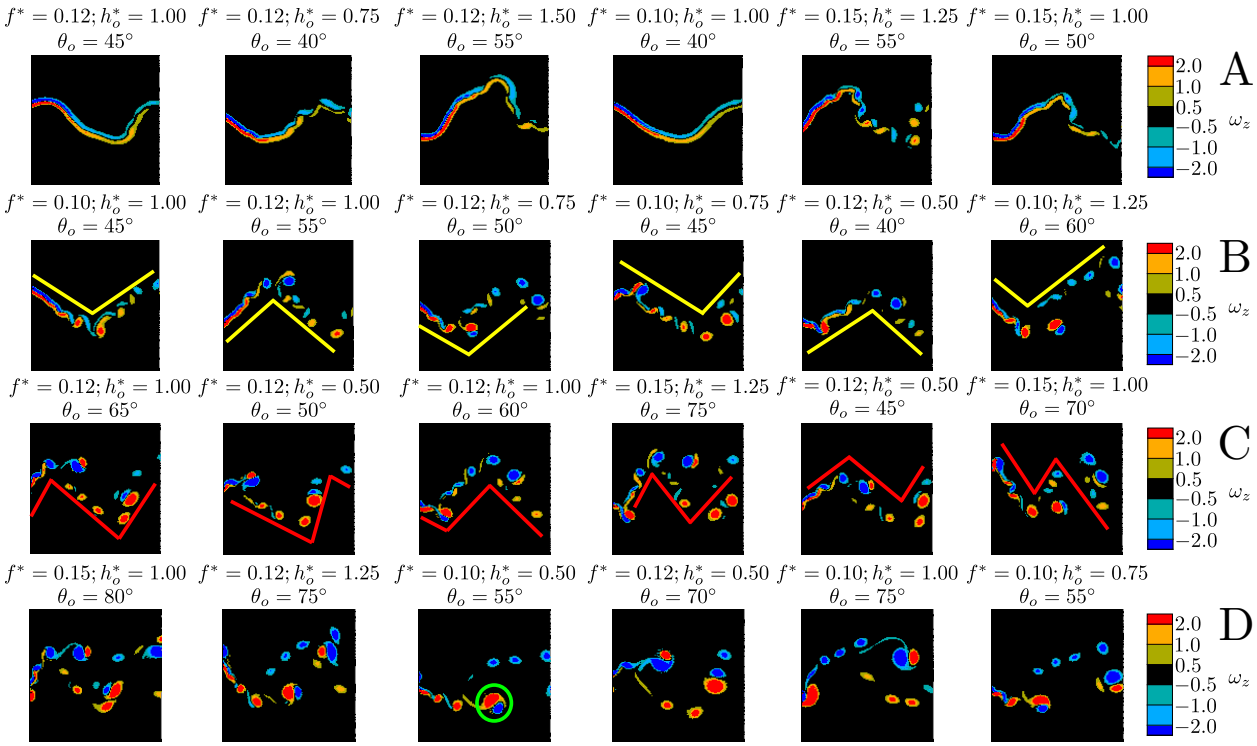

Figure 5.6: Wake structures colored by spanwise vorticity (ω_z) for each class displayed in Figure 5.5b. The wake images are randomly selected within each class and the foil kinematics corresponding to each wake is displayed at top of each image. The yellow, red lines and green circle correspond to each wake pattern.

The wake patterns obtained by the classification and clustering models are significantly different from those found in propulsive foils. Comparing with previous work by Calvet et al. [51], they obtained six different wake patterns that are correlated with two parameters,

$\alpha_{T/4}$ and Strouhal number $\left(St = \frac{2fh_o}{U_\infty}\right)$, which varied from $0° < \alpha_{T/4} < 40°$ and $0.2 < St < 1.2$. Due to the higher reduced frequency of propulsive foils, more wake structures are found closer to the foil and this contributes to a higher contrast of wake patterns across clusters compared with those in Figure 5.6. This contrast also contributes to the difference in the number of wake patterns between foil regimes. While the work by Calvet et al. obtained six wake patterns behind propulsive foils, the analysis performed here identified four distinct wakes under the energy harvesting regime.

Class D demonstrates high variation in efficiency within its kinematics. This is observed between $\alpha_{T/4} = 40.5°$ and $\alpha_{T/4} = 41.9°$ where efficiency drops by approximately 9% (see Figure 5.5b). This could be described as a bifurcation in the efficiency curve at $\alpha_{T/4} > 28.0°$ as illustrated by an upper and lower branches. However, neither the classification nor clustering models could discern differences in the wakes between the higher and lower branches of efficiency within class D. To further investigate these branches, the foil parameters corresponding to each kinematics are explored and it is noticed that all foil kinematics in the lower branch have a reduced frequency of $fc/U_\infty = 0.10$ and the upper branch, $fc/U_\infty = 0.12 - 0.15$.

The new updated classes also provide patterns in power extraction, as displayed in Figure 5.7. Each curve corresponds to the phase-averaged total power extracted in a half-cycle from a representative foil kinematics in each class. All classes display a power peak close to the mid-stroke position $(t/T = 0.25)$, which corresponds to the foil's maximum heave velocity and thus typically is where maximum power is reached. Class A shows a smooth power profile with a lower amplitude compared to the other classes as expected due to the absence of coherent vortices generated by the foil. With the formation of LEVs as $\alpha_{T/4}$ increases, class B still highlights a smooth profile and class C indicates a higher power magnitude and higher unsteadiness on $t/T = 0.3 - 0.5$. This unsteady behavior is most likely caused by secondary vortices formed on the foil due to a higher $\alpha_{T/4}$ in class C compared to class B. This unsteadiness is more apparent in the lower branch of class

D where large and strong vortices are formed and shed from the foil. The power profile in the representative kinematics of the upper branch is similar to the lower branch in the region $t/T = 0 - 0.3$ but it displays a second power peak in the remaining portion of the half-cycle. This peak is caused by the higher reduced frequency of the kinematics in the upper branch, which contributes to a delay in the vortex shedding and thus more power is extracted.

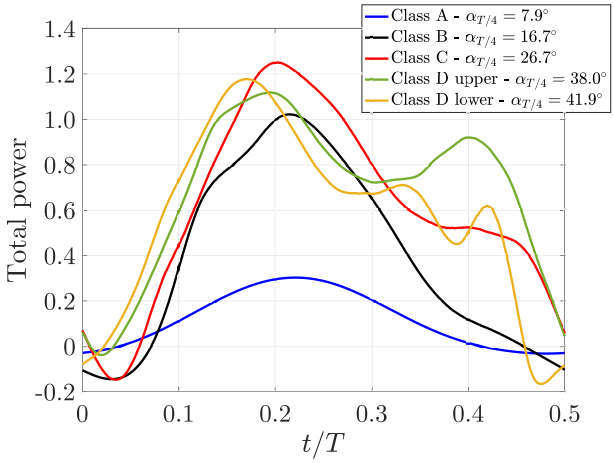

Figure 5.7: Phase-averaged total power extracted in a half-cycle from a representative foil kinematics within each class.

To visualize those vortex structures, the wakes from both upper and lower branches are illustrated in Figure 5.8. As observed in Section 5.2 and by Ribeiro et al. [44], a lower reduced frequency is correlated with vortex structures spending less time on foil surface, which decreases the pressure gradient around the foil. The wake structures between upper and lower branches are different with more vortices located within the wake window in the upper branch due to higher foil's reduced frequency but still no pattern can be visualized. Although neither the classification nor clustering models could discern the differences just described in these branches, a possible solution would be to provide additional information about the kinematics of each wake image to the convolutional neural network like the reduced frequency, similar to the method implemented by Morimoto et al. [53], but it is

not explored in this investigation. Another potential solution would be to have more foil kinematics and hence more data in class D.

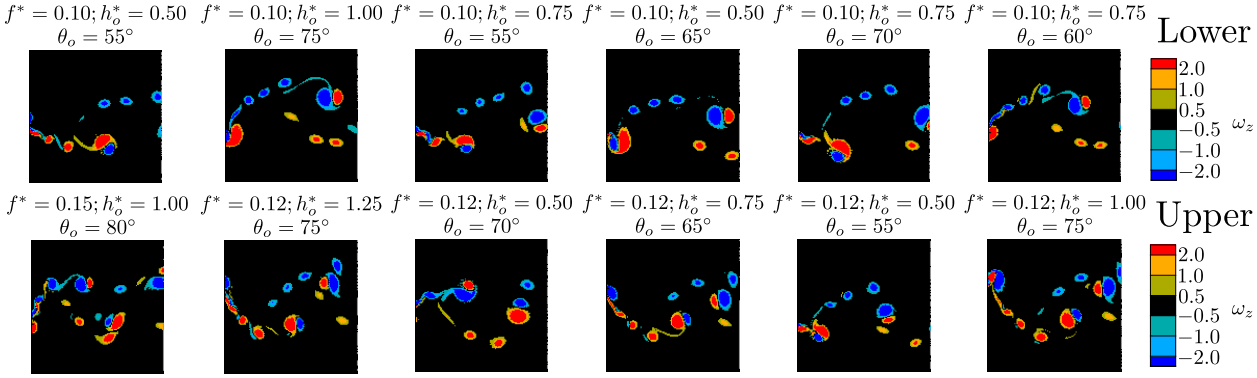

Figure 5.8: Wake structures colored by spanwise vorticity (ω_z) that emerge from foil kinematics within each branch in class D highlighted in Figure 5.5b. The wake images are randomly selected and the foil kinematics corresponding to each wake is displayed at top of each image.

The wake patterns obtained from the updated classes can also be used to predict the power extraction of foil-arrays. For instance, the wake pattern generated from a class with low $\alpha_{T/4}$ values ($5.3° \leq \alpha_{T/4} \leq 11.7°$) does not significantly impact energy extraction from foils placed downstream due to the absence of coherent vortices that disturbs the oncoming flow of trailing foils. The opposite is true for a class with high $\alpha_{T/4}$ values ($29.3° < \alpha_{T/4} \leq 50.5°$).

5.5 Conclusion

A machine learning model is developed to classify wake structures behind an oscillating foil in the energy harvesting regime of flapping foil kinematics. The goal of the paper is to utilize the machine learning algorithm to sort and classify wake modes using the vorticity fields downstream of the oscillating foil and correlate the kinematics with associated wake patterns. This model gives insight on wake similarity among various foil kinematics, which is important to build predictive models of oscillating foil arrays for energy harvesting.

Data is obtained through simulations of oscillating foils at 46 unique kinematics, and time-dependent vorticity flow fields are extracted at equal times across three simulation cycles to form a total of $23,692$ samples. Based on previous work [78], three initial classes are defined based on values of the relative angle of attack, $\alpha_{T/4}$. The classification model consists of four convolutional layers and 90 LSTM units applied on multiple input sequences of five samples each. The model's output consist of three neurons corresponding to the classes A, B, C. After the model is trained and tuned, the average test accuracy among all folds is 92% with the majority of foil kinematics showing a label mismatch percentage less than 50% between actual and predicted, demonstrating the model's ability to discern wakes among classes.

Although the classification model is successful in finding wake patterns the class divisions are predetermined by the researcher, and assumed to correlate with only one parameter, $\alpha_{T/4}$, thus biasing the relationship between wake structure and flapping kinematics. Therefore, an unsupervised approach is performed through a CAE clustering algorithm, which does not require any prelabelling or bias. The results indicate that there is still a strong correlation with $\alpha_{T/4}$, and that clusters naturally align with this kinematic parameter. Furthermore, analysis shows that four clusters are optimal instead of three that were originally proposed.

In summary, the clustering model provided validation that $\alpha_{T/4}$ was a predictive kinematic parameter for wake structure, and outlined an additional grouping previously undetected by the researcher. A final configuration of four new classes is proposed which results in an average fold accuracy of 91% using the classification algorithm. The four classes offer new physical insight on wake patterns within each range of foil kinematics based on vortex strength and oscillatory wake structure. Further analysis is performed in the class with the highest $\alpha_{T/4}$ values and additional wake patterns are obtained that could not be captured by either the classification or clustering algorithms. This research builds upon the knowledge of how wake patterns and kinematics are correlated, which

is instrumental in developing predictive models of oscillating foil arrays in which vortex wakes directly impact the energy harvesting of downstream foils.

6 Power Extraction and Prediction in a Dual Oscillating Foil System

6.1 Background and motivation

This chapter focuses on quantifying the contributions and developing an estimation of the power generation in a two-foil energy harvesting system.

In a flapping-foil turbine, total power is divided into the heave and pitch components. The heave power is composed of the lift force and the heave velocity, whereas the pitch power is defined by the torque on the foil and the pitch velocity. Both components are a function of the flapping foil frequency, heave and pitch amplitude [7–9,87]. For an optimal foil performance, heave power dominates the total power and the average pitch power is close to zero [17,18,88]. During the heave stroke, power is augmented by the formation and shedding of a coherent leading edge vortex (LEV) as the associated low pressure region causes an increase in the lift force [21,89]. Depending on the foil parameters, a trailing edge vortex (TEV) can also form, and/or more than one LEV, forming a two-dimensional structured wake intricately linked to the underlying flapping kinematics [90].

Many researchers have considered a tandem array configuration with the same kinematic motion for both foils, where two parameters dictate the configuration, the inter-foil phase, ψ, and inter-foil spacing, S_x. Numerical [33–35, 37, 69, 91] and experimental [32,36,92,93] work show these two parameters greatly affect array performance due to the different wake-foil interactions. To establish a relationship between the trailing foil motion and the oncoming wake, Kinsey and Dumas [74] defined a global phase parameter, Φ, combining inter-foil phase with the wake trajectory assuming it convects at the freestream velocity. More recently, as also shown in Chapter 4, by quantifying the mean wake velocity from various leading foil kinematics, Ribeiro et al. [94] replaced U_∞ in the global phase and

defined as a *wake phase* parameter. With this update, they noted that foil performance has a stronger relationship with wake phase where the phase that corresponds to a minimum or maximum power generation is independent of the foil kinematics. A wake phase of 0° corresponds to the trailing foil oscillating in-sync with the wake, or directly impinging on strong vortex structures whereas, a wake phase of 180° provides the highest trailing foil performance since it avoids destructive vortex-foil interactions.

The interaction between vortex gusts and foils are extensively analyzed in literature especially at stationary foils. Through analyzing the interactions between vortex gusts at different positions with respect to a stationary foil, Peng and Gregory [95] classified the vortex-foil proximity and the impacts on the foil performance into three categories in terms of vortex dynamics: close interaction, very close interaction, and collision. Focusing on the effect of vortex rotation, Barnes and Visbal [96,97] noted that counter-clockwise and clockwise vortices may trigger or hinder the leading edge vortex formation and shedding depending if the interaction occurs at the top or bottom foil surfaces.

To predict the effects of vortex-foil interactions on foil performance, researchers started characterizing vortex gusts and establishing relationships with the lift force on the foil. Biler et al. [98] experimentally investigated gust-foil interactions on a stationary foil and noted similar trends between a gust-induced angle of attack profile over time and the transient lift force. This approach is expanded to stationary foils interacting with von Karman vortex streets generated from oscillating foils and a close relationship between the effective angle of attack of and the lift force on the foil still persisted [99].

When considering a dynamic foil motion interacting with wake disturbances, Xu et al. [100] showed that vortex-foil interactions in a potential flow field translate to a unsteady lift and angle of attack deviation from reference profiles of a foil oscillating in a wake without disturbances. Using steady-state aerodynamic theory, Muscutt et al. [101] predicted thrust forces and although the effects of destructive vortex-foil interactions are captured by their

virtual foil methodology, alternative approaches are necessary to estimate the performance augmentation from constructive wake-foil interactions.

Therefore, with information from a single foil wake, this chapter proposes a physics-based approach from the mean flow and unsteady vortex-foil interactions to estimate the time-dependent power coefficient in a two-foil turbine array. The effective angle of attack is calculated to characterize the wake-foil interactions and correlate with the power generation from a trailing foil to provide a power estimate. The power prediction is then compared against two-foil simulations from Ribeiro et al. [94].

6.2 Numerical Methods

This section introduces the computational data utilized in the analysis, and defines the kinematic motion and power generation in tandem two-foil arrays. The wake velocity between foils is quantified, which is used to normalize the power from a trailing foil.

Computational data utilized in analysis

With the foil kinematic motion defined, the computational data utilized in this chapter numerically solves it at Reynolds number $Re = 1000$, simulated with second-order accurate finite volume, pressure-implicit split-operator (PISO) algorithm in *OpenFOAM* [59]. A two-dimensional unstructured dynamic mesh is utilized and the refinement analysis along with the validation of the dynamic mesh against a stationary mesh are presented in Ribeiro et al. [94].

Two data sets are considered in this chapter. The first set of simulations are single foils [90] which are used to extract information from the wake under various flapping kinematics and the foil motion is the same as shown in Equations 2.1 and 2.2. The second set of simulations are tandem two-foil arrays where the inter-foil phase, ψ, is utilized and the kinematic motion for the leading foil (foil 1) is

$$h_1(t) = -h_{o,1}\cos(2\pi ft) \qquad \theta_1(t) = -\theta_{o,1}\sin(2\pi ft), \tag{6.1}$$

and for the trailing foil (foil 2)

$$h_2(t) = -h_{o,2}\cos(2\pi ft + \psi) \qquad \theta_2(t) = -\theta_{o,2}\sin(2\pi ft + \psi). \tag{6.2}$$

To reduce the parameter space, the same foil parameters are applied to both foils ($h_{o,1} = h_{o,2} = h_o$; $\theta_{o,1} = \theta_{o,2} = \theta_o$). The inter-foil phase ranges from -180° to $+180^\circ$ with an increment of 30°. The range of foil kinematics investigated in this chapter includes $f = 0.10 - 0.15$, $h_o = 0.75 - 1.50$, and $\theta_o = 55^\circ - 75^\circ$ for a total of 16 sets of kinematics. The parameter range selected is ideal for oscillating foils in energy harvesting mode [8].

Quantifying wake velocity

To visualize the parameter space, the schematic in Figure 6.1 displays the foil parameters, the inter-foil spacing, S_x, and the swept area, Y_p of a tandem two-foil array where a trailing foil (foil 2) is placed in the leading foil (foil 1) wake. Due to the wake deficit, the wake velocity, $\mathbf{u_w}$, is lower than the freestream, and it is represented by

$$\mathbf{u_w}(y, t : x_w) = u\hat{\boldsymbol{\imath}}(y, t : x_w) + v\hat{\boldsymbol{\jmath}}(y, t : x_w), \tag{6.3}$$

where u and v correspond to the streamwise and cross-flow velocity components extracted at x_w downstream from foil 1, respectively. In this chapter the wake velocity extraction is performed at $5c$ since the spacing between foils is fixed at $6c$, and thus provides an accurate representation of the oncoming energy flux to foil 2.

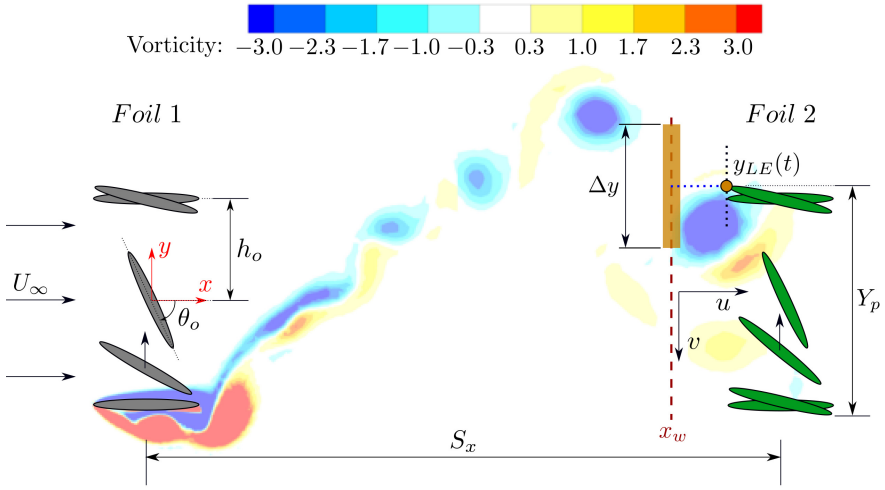

Figure 6.1: Leading foil (foil 1) parameters and placement of a trailing foil (foil 2) to form a two tandem foil-array. Vorticity flow field at time t is illustrated along with vortex window Δy at wake probe location x_w.

Figure 6.1 also shows the length Δy that corresponds to the size of a vortex window that captures the wake disturbances as the trailing foil oscillates and is centered at its leading edge, y_{LE}. The window size can be tuned however $\Delta y = 1.2c$ is sufficient to capture the primary wake vortex in all cases investigated.

With the vortex window defined, the mean wake velocity u_w measured at x_w can be quantified by the spatially and time-averaged magnitude of $\mathbf{u_w}$ as described as

$$u_w = \frac{1}{Y_p + \Delta y} \int_0^T \int_{-(Y_p+\Delta y)/2}^{+(Y_p+\Delta y)/2} \sqrt{u^2(y,t) + v^2(y,t)}\, dy\, dt, \tag{6.4}$$

where the reason to add the vortex window size, Δy with the swept area Y_p is to encompass the energy of the oncoming vortices as they convect over the trailing foil swept area.

Definition of normalized power generation

The freestream and the mean wake velocities are the oncoming flow velocities to the foil 1 and 2, respectively, and thus can be utilized to normalize the power generation from each foil.

The total power generation P in oscillating foil-arrays is defined as the sum of heave and pitch power. Although both components contribute to energy extraction, heave power dominates over pitch as for an optimal foil performance, the average pitch power is close to zero [17,18,88]. Thus, the power coefficient for the leading foil, $C_{p,1}$, can be approximated by using only the heave component

$$C_{p,1}(t) = \frac{P_{extraction}}{P_{available}} = \frac{\dot{h}_1 L_1(t)}{\frac{1}{2}\rho U_\infty^3 c}, \tag{6.5}$$

where L is the lift force on the foil and $\frac{1}{2}\rho U_\infty^3 c$ is the total power available from the freestream velocity per planform area of the foil.

For the trailing foil, the inter-foil phase and the wake deficit influence the power generation. Therefore, the power coefficient for the trailing foil, $C_{p,2}$, is given by

$$C_{p,2}(\Phi, t) = \frac{\dot{h}_2 L_2(\Phi, t)}{\frac{1}{2}\rho u_w^3 c}, \tag{6.6}$$

where Φ is the wake phase [94],

$$\Phi = 2\pi \frac{S_x f}{u_w} + \psi, \tag{6.7}$$

and it is obtained by adjusting the inter-foil phase, ψ, with a non-dimensional wake wavelength $2\pi \frac{S_x f}{u_w}$.

The wake phase encompasses the vortex-foil interactions that occur at different foil-array configurations. To illustrate the effects of wake-foil interactions on the foil performance, Figure 6.2 displays the instantaneous power coefficient profiles at wake phases 0° and 180° for the foil parameters $f = 0.10$, $h_o = 1.00$, and $\theta_o = 55^\circ$. The yellow and green shaded colors represent the portions during the cycle where wake-foil interactions are decreasing or increasing the foil performance, respectively.

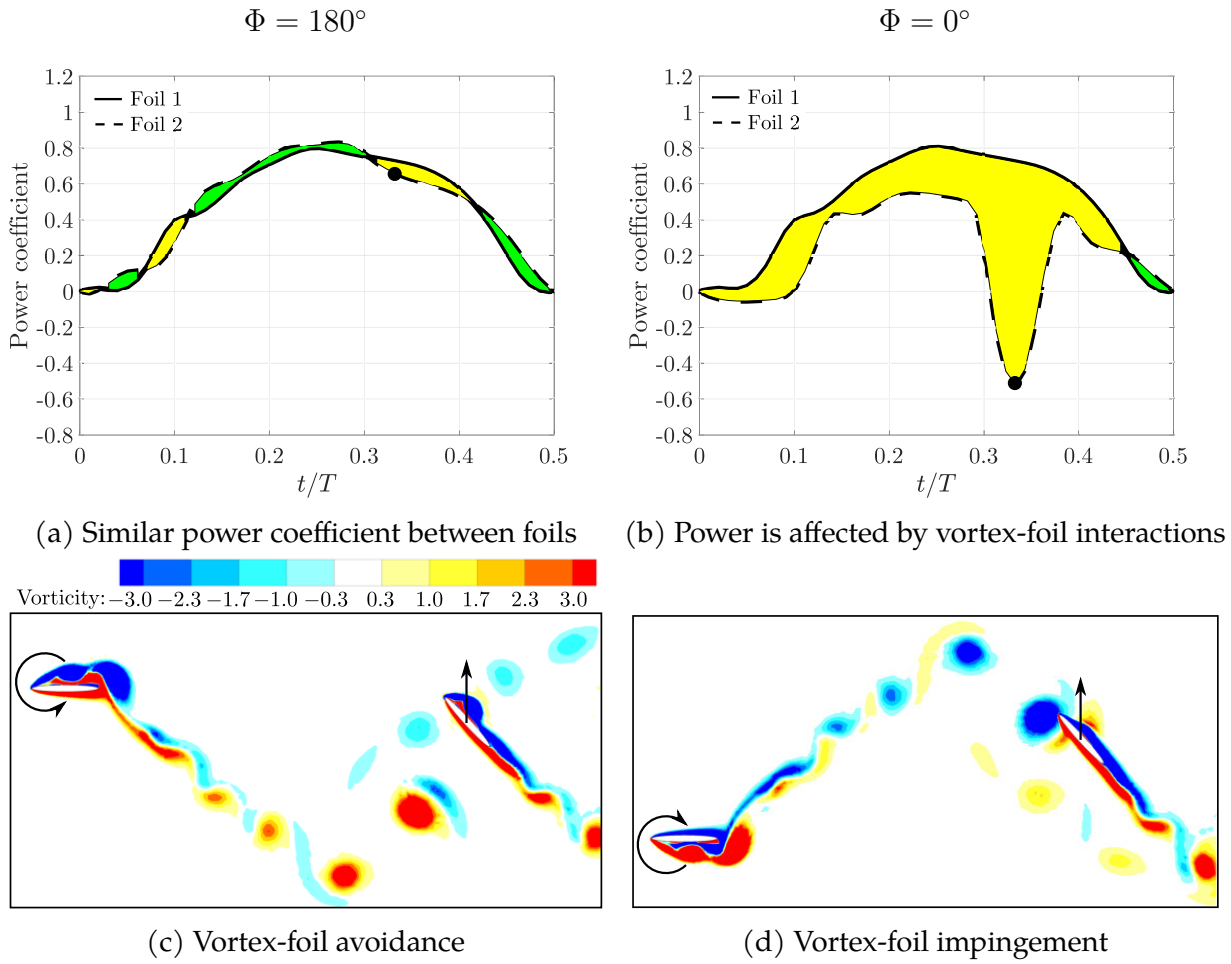

(a) Similar power coefficient between foils

(b) Power is affected by vortex-foil interactions

(c) Vortex-foil avoidance

(d) Vortex-foil impingement

Figure 6.2: Analysis of vortex-foil interactions at wake phases $\Phi = 180°$ and $\Phi = 0°$ and foil parameters: $f = 0.10; h_o = 1.00; \theta_o = 55°$. These phases illustrate the power contributions of the vortex gusts on the trailing foil when, for this case, there is a vortex-foil impingement ($\Phi = 0°$) or vortex avoidance ($\Phi = 180°$). The instantaneous vorticity flow fields are plotted at $t/T = 0.33$ (black markers).

The power from each foil is normalized according to its oncoming flow velocity. At $\Phi = 180°$ (Figures 6.2a and 6.2c), the trailing foil is avoiding strong unsteady vortex-foil interactions and thus, when the power from trailing foil is normalized with respect to the mean wake velocity, the power coefficient profiles from both foils overlap each other. In contrast, at $\Phi = 0°$ (Figures 6.2b and 6.2d), there is a vortex-foil impingement or destructive interactions at the time shown ($t/T = 0.33$), which translates to a significant drop of the trailing foil power coefficient (black marker). This shows that the difference between power curves are directly related to the unsteady interactions between foil and vortex gusts.

This analysis is extended by the work from Ribeiro et al. [88] to various tandem foil-array configurations and they noted that for foil kinematics with $6^\circ < \alpha_{T/4} < 43^\circ$, a wake phase close to $\Phi = 0^\circ$ produces stronger wake-foil interactions and thus larger deviations between $C_{p,1}$ and $C_{p,2}$ compared to wake phases closer to 180°.

6.3 Prediction Model

The unsteady vortex-foil interactions presented in Section 6.2 correspond to the power difference between foils normalized by their respective oncoming flow velocity. In this section, these vortex disturbances are associated with the change in the effective angle of attack of a trailing foil. This relationship, which is obtained solely from single foil simulations, will be used to develop a model that predicts the power generation from the trailing foil at different wake phases through separating the power into a mean and unsteady components.

Effective angle of attack in the presence of vortex disturbances

The vortex disturbances, indicated with superscript v, are characterized by quantifying the instantaneous wake velocity within the vortex window. The instantaneous velocity, $\mathbf{u^v}$, is the spatially averaged wake velocity over the window Δy with respect to the wake phase,

$$\mathbf{u^v}(\Phi, t) = \frac{1}{\Delta y} \int_{y_{LE}(t+t^v)-\Delta y/2}^{y_{LE}(t+t^v)+\Delta y/2} \mathbf{u_w}(y, \Phi, t)\, dy. \tag{6.8}$$

Time is shifted by t^v,

$$t^v = \frac{S_x - x_w}{u_w}, \tag{6.9}$$

to account for the convection time between the measured wake at $x = x_w$ and the trailing foil at $x = S_x$. The value of $y_{LE}(t+t^v)$ corresponds to the trailing foil's leading edge position at $t + t^v$ which is when the gust-foil interactions occur.

The velocity within the vortex window allows the calculation of the effective angle of attack of the trailing foil, α^v, illustrated in Figure 6.3.

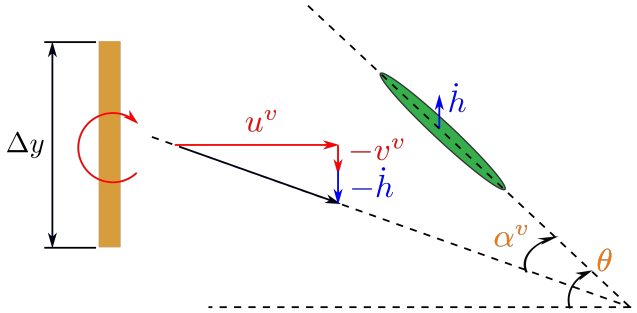

Figure 6.3: Effective angle of attack of the trailing foil in the presence of wake disturbances.

The effective angle of attack at $x = x_w$ is then given by

$$\alpha^v(\Phi, t) = \theta(t) - \tan^{-1}\left(\frac{-\dot{h}(t) - v^v(\Phi, t)}{u^v(\Phi, t)}\right), \tag{6.10}$$

and it is assumed it remains constant as the vortex gust convects from $x = x_w$ to $x = S_x$.

Introduction of a reference foil with an equivalent mean flow

To quantify the effects of the vortex gust on the trailing foil, an equivalent foil operating in a mean flow velocity u_w is introduced as a reference foil. The kinematic parameters are normalized by u_w, creating $\dot{h}^*$, θ^*, and f^*,

$$f^* = \frac{f}{u_w} \qquad h^*(t) = -h_o \cos(2\pi f^* t) \qquad \theta^*(t) = -\theta_o \sin(2\pi f^* t). \tag{6.11}$$

Figure 6.4 displays the effective angle of attack of the reference foil, α^*,

$$\alpha^*(t) = \theta^*(t) - \tan^{-1}\left(\frac{-\dot{h}^*(t)}{u_w}\right). \tag{6.12}$$

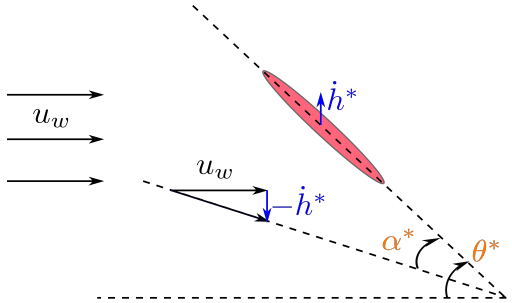

Figure 6.4: Effective angle of attack of the reference foil (no wake disturbances).

The difference of the effective angle of attack between reference and trailing foils, $\Delta\alpha$,

$$\Delta\alpha(\Phi, t) = \alpha^v(\Phi, t) - \alpha^*(t), \tag{6.13}$$

corresponds to the strength of the unsteady gust-foil interactions.

The power generation from the reference foil is also calculated using the normalized lift force L^* and $\dot{h}^*$ or

$$C_p^*(t) = \frac{\dot{h}^* L^*(t)}{\frac{1}{2}\rho u_w^3 c}, \tag{6.14}$$

and similar to the difference in the effective angle of attack between reference and trailing foils, the power difference, ΔC_p, between the gust-foil interaction and the equivalent reference foil is

$$\Delta C_p(\Phi, t) = C_{p,2}(\Phi, t) - C_p^*(t) = \frac{\dot{h}_2 L_2(\Phi, t)}{\frac{1}{2}\rho u_w^3 c} - \frac{\dot{h}^* L^*(t)}{\frac{1}{2}\rho u_w^3 c}. \tag{6.15}$$

To illustrate the relationship between these quantities, Figure 6.5 shows $\Delta\alpha$ and ΔC_p profiles within the upstroke foil motion ($t/T = 0 - 0.5$) for the wake phase $\Phi = 0°$ with foil parameters $f = 0.10$, $h_o = 1.00$, and $\theta_o = 55°$. There is a significant $\Delta\alpha$ drop at approximately $t/T = 0.33$, which translates to a vortex-foil interaction that is detrimental to the formation of vortices over the foil. This destructive interaction is also observed by a ΔC_p drop at approximately the same time.

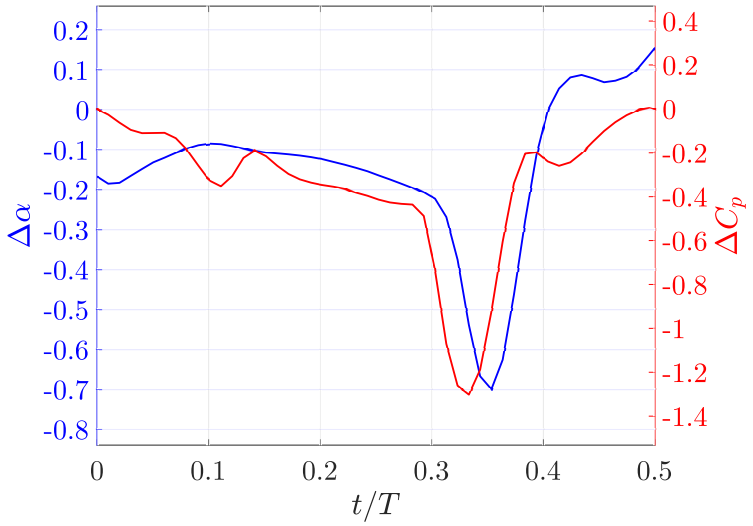

Figure 6.5: Comparison between the difference in effective angle of attack and power coefficient at $\Phi = 0^\circ$ for foil parameters of $f = 0.10$, $h_o = 1.00$, and $\theta_o = 55^\circ$.

Correlating difference in the effective angle of attack with the power difference between foils

This subsection develops a model describing the relationship between $\Delta\alpha$ and ΔC_p. First, Equation 6.15 shows that the power difference between foils corresponds to the lift difference multiplied by the respective heave velocity of each foil. Since the effective angle of attack is proportional to the lift force on foil, it is assumed that the difference of each quantity is also proportional to each other, creating a power difference with respect to the effective angle of attack, $\Delta\widetilde{C_p}$,

$$\Delta\widetilde{C_p}(\Phi, t) = \dot{h}_2\alpha^v(\Phi, t) - \dot{h}^*\alpha^*(t). \tag{6.16}$$

The quantity $\Delta\widetilde{C_p}$ is obtained from single foil simulations as it only depends on the wake velocity extraction within the vortex window. Therefore, using the power from the reference foil as a baseline, $\Delta\widetilde{C_p}$ allows for a prediction of the trailing foil power coefficient, C_p^v,

$$C_p^v(\Phi, t) = C_p^*(t) + \beta \Delta \widetilde{C_p}(\Phi, t), \tag{6.17}$$

where β is a fitting parameter between the power difference with respect to lift and effective angle of attack. This parameter is obtained after comparing the profiles of $\Delta \widetilde{C_p}$ with respect to time at different wake phases, where it is found that it self-similar decays and shifts in time from $\Phi = 0^\circ$ to the other wake phases. Labeling the time when $\Delta \widetilde{C_p}$ reaches its peak at $\Phi = 0^\circ$ as t^*, the fitting parameter is given by

$$\beta(t, t^*) = 5e^{-\left(\frac{t-t^*}{0.2}\right)^2}. \tag{6.18}$$

The parameter β is of a Gaussian form to indicate the decay of $\Delta \widetilde{C_p}$ as it deviates from $\Phi = 0^\circ$. The amplitude and width of the Gaussian modify the scaling and decay rate of $\Delta \widetilde{C_p}$, respectively. A higher decay rate or lower amplitude are translated to a prediction closer to the reference foil power, which is found in configurations with wake phases closer to 180°. The values of 5 and 0.2 are selected after tuning the predicted trailing foil power coefficient with the obtained from simulations. For simplicity, the same β profile is applied to all cases investigated.

To quantify the error between predicted power from trailing foil and simulation, the L^2-norm averaged over all 12 wake phases ($\Phi = -180^\circ : 30^\circ : 150^\circ$) is utilized,

$$\overline{C_{p,RMS}} = \frac{1}{12} \sum_{\Phi} \sqrt{\frac{1}{n} \sum_{k=1}^{n} \left(C_{p,2}^k(\Phi, t) - C_p^{v,k}(\Phi, t) \right)^2}. \tag{6.19}$$

6.4 Model Evaluation

In this section, the model is evaluated at different foil kinematics with respect to time and wake phase. The limitations of the model are also discussed.

Comparing instantaneous power profiles across reference, trailing foils, and prediction

The instantaneous power coefficient from the reference and trailing foils are displayed in Figure 6.6 at three wake phases from three sets of kinematics. Across the three wake phases and cases, the power trends are captured by the model as shown by the proximity between the solid and dashed green lines. The amplitude between model and simulation is remarkably close to each other with the exception of when a significant power variation in a short period of time occurs as seen at around $t/T = 0.33$ for the case $f = 0.10; h_o = 1.00; \theta_o = 55°; \Phi = 0°$ where in a span of $t/T = 0.03$, C_p^v decreased from approximately $+0.6$ to -0.6. For a higher $\alpha_{T/4}$ as in $f = 0.12; h_o = 1.00; \theta_o = 65°$, a prediction overshoot may occur due to stronger secondary vortices not captured by the vortex window as exemplified at $\Phi = -120°$. The deviation in power obtained from the model and simulation can also be explained by the model considering a unique amplitude decay profile for all cases. With stronger vortices in the wake, the strength of vortex-foil interactions are also stronger and thus, the decay rate may be slower with respect to wake phase if compared with cases of lower $\alpha_{T/4}$.

According to the wake phase, the trailing foil power variations are in agreement with what Xu et al. [100] noted in their analysis of a two-foil propulsion array even though the kinematics used in their work have a different range of frequency, heave and pitch amplitudes. The similarity between the prediction of the trailing foil power and the result from the simulations reinforces using the effective angle of attack as a parameter that has a relationship with the foil power generation as shown by Biler et al. [98].

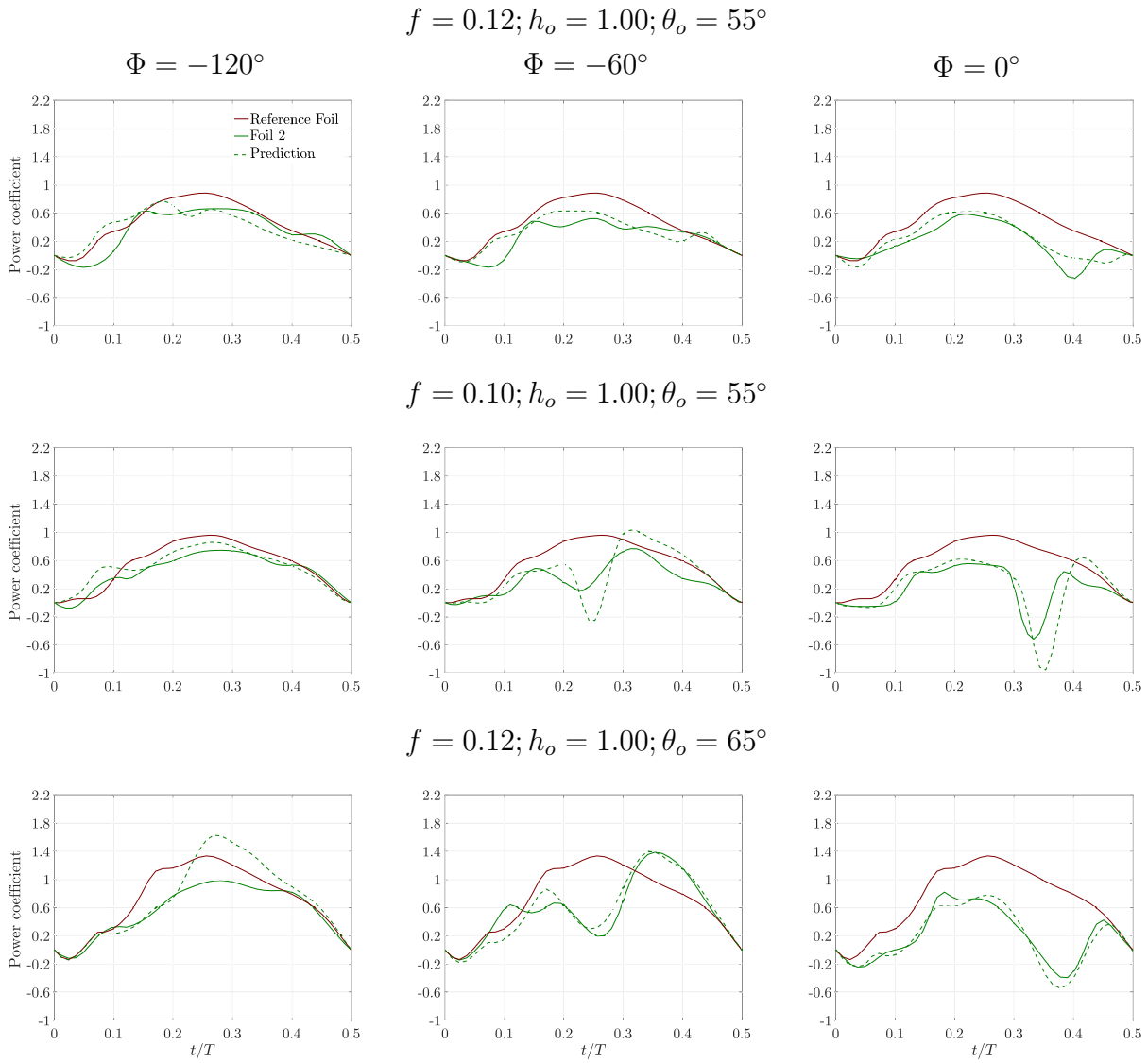

Figure 6.6: Comparison between power prediction (C_p^v), trailing foil ($C_{p,2}$) and reference foil (C_p^*) at three wake phases and configurations.

Evaluation with respect to wake phase

When considering all wake phases, the mean power coefficient over time is taken at each phase for the same three cases as displayed in Figure 6.7. The dark red lines are the mean power coefficient from the reference foil which is independent of the wake phase. The cases from Figure 6.7a to 6.7c increase in $\alpha_{T/4}$ and in the strength of vortex-foil interactions which explains the power increase from the reference foil and its higher variation with respect to wake phase for the trailing foil, respectively [94]. This variation goes from a smooth

sinusoidal trend to non-sinusoidal and the prediction model is still able to appropriately describe the trailing foil power dependency on the wake phase as noted by the similarity between the green solid and dashed lines.

Although the mean power profile trends are captured by the model, at high wake phases ($\Phi > 60°$), the mismatch between simulation and model is apparent especially in Figures 6.7b and 6.7c. A potential reason for this deviation is an inaccurate vortex-foil interaction timing captured by the vortex window as the foil may interact with the oncoming vortices in a faster rate than the vortex convection time considered.

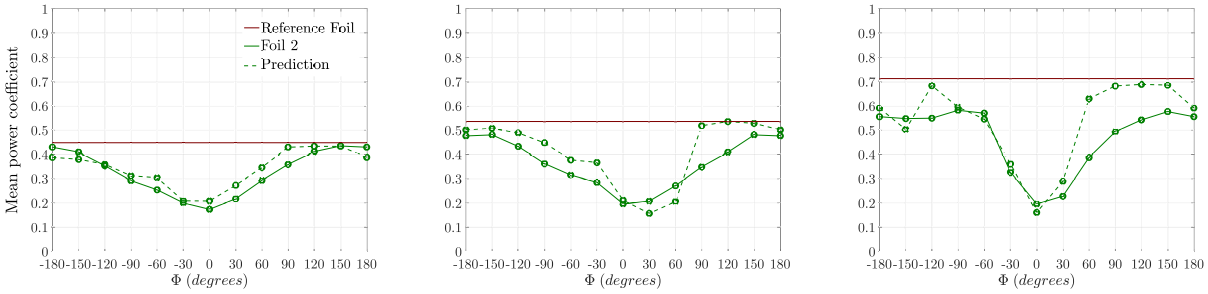

(a) $f = 0.12; h_o = 1.00; \theta_o = 55°$ (b) $f = 0.10; h_o = 1.00; \theta_o = 55°$ (c) $f = 0.12; h_o = 1.00; \theta_o = 65°$

Figure 6.7: Time-averaged trailing foil power comparison between simulation and prediction model with respect to wake phase for three sets of foil kinematics. The dark red line corresponds to the mean power from the reference foil.

Since the model presented in this chapter only requires quantifying the trailing foil effective angle of attack and the power from a reference foil, a prediction can be obtained in other foil-array configurations such as a staggered arrangement with different kinematics applied to both foils. The primary difference in this configuration is that the foil may interact with the oncoming vortices in opposite strokes from a in-line two-foil array. For instance, as shown in Figure 6.6, the trailing foil interacts with the primary vortex during the upstroke motion ($t/T = 0 - 0.5$). In a two-foil staggered array, the trailing foil may interact with the same vortex during downstroke.

Model limitations

Although the model still captures the power trends and provides a similar magnitude to simulations, for stronger vortex wakes generated by flapping kinematics at high $\alpha_{T/4}$, the vortex window used in the model may not be sufficient to represent the interactions that occur from the secondary vortices in the near field from the trailing foil. This is relevant for the cases with $\alpha_{T/4} > 30°$ as the wake from these cases contain not only an leading edge vortex but also a trailing edge vortex [94]. This is shown in Figure 6.8 where it displays the model error represented by $\overline{C_{p,RMS}}$ with respect to $\alpha_{T/4}$, separated by trends based on each foil parameter. For cases with $\alpha_{T/4} > 30°$, $\overline{C_{p,RMS}} > 0.3$.

In contrast, with a pitch amplitude equals to $55°$, error is approximately 0.1. The smaller prediction error is justified based on weaker vortex gusts and thus closer proximity between the reference and trailing foil power. At $\theta = 65°$ and $\alpha_{T/4} < 30°$, error is split in terms of the heave amplitude. A small heave amplitude provides an error close to 0.2 in comparison with 0.3 for $h_o > 1.00$. A potential solution to decrease this error is to increase the vortex window size to try encompassing more wake vortices that may interact with the foil at a higher heave amplitude.

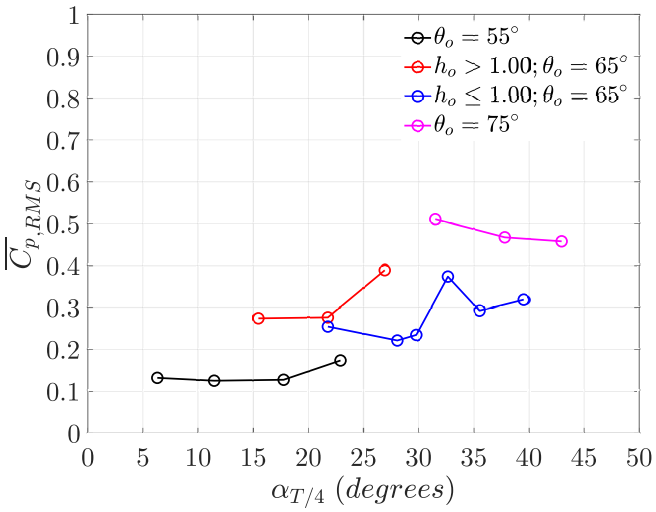

Figure 6.8: Error between the predicted trailing foil power coefficient and the obtained from the simulations with respect to the effective angle of attack $\alpha_{T/4}$. Trends based on each foil parameter are shown.

6.5 Conclusion

This chapter develops a power prediction model for oscillating-foil turbine arrays where the foil-arrangement is governed by the spacing between the two foils and the wake phase. The goal is to predict power from trailing foils using only single foil simulations, which are used to quantify the wake velocity and the trailing foil effective angle of attack.

The effective angle of attack is utilized to correlate the wake-foil interactions with the trailing foil power generation and it is quantified at two foils: trailing foil and reference foil. The reference foil considers an equivalent mean flow velocity from the configuration where wake disturbances are included in the analysis. The difference between the two power curves and the effective angle of attack from both foils represents the unsteady contributions to the power extraction.

To develop a correlation between these quantities, it is assumed that the difference of the effective angle of attack is proportional to the lift difference between reference and trailing foils. After using a fitting parameter based on the self-similarity decay of the power difference with respect to the effective angle of attack, a prediction of the trailing foil power is performed and compared with the simulations.

The results show the error between the prediction and simulation ranges from $0.1 - 0.3$ for cases below $\alpha_{T/4} < 30°$, and the model captures both power trends and magnitudes across wake phases. At higher relative angles of attack, the wake vortices are stronger and multiple vortices are interacting with the foil which makes the prediction more challenging. For the selected decay profile and vortex window size, the error increased to $0.3 - 0.5$. Nevertheless, for cases as high as $\alpha_{T/4} = 30°$, the model is able to estimate the power across various wake phases for relevant foil-array configurations for energy harvesting.

Since the model only requires quantifying the effective angle of attack from a trailing foil and power from a reference foil, a prediction can be made in other foil-array configurations like staggered arrangements and different kinematics applied to both foils. Therefore, the

ability to predict power without simulating a trailing foil is a useful tool in building an optimization algorithm for energy harvesting in turbine arrays.

7 Concluding remarks

Oscillating-foil turbines for energy harvesting from tides and rivers are explored in this thesis as they offer advantages such as operation in shallow waters, low tip speeds and more easily scalable in both width and arrays compared to traditional rotary turbines. Although flapping foils provide advantages, the flow and analysis around such turbines are considered complex due to the high non-linearity between foil kinematics and the vortices formed and shed from the foil. When foils are placed in array configurations, the parameter space increases and hence analyzing foil's performance becomes an even more challenging task.

With the goal of understanding the flow around flapping foils, the thesis first explores the Reynolds number dependence in chapter 3. 2D DNS simulations at $Re = 1000$ are compared against 3D LES simulations at $Re = 50,000$ and it is noticed that the higher Reynolds simulations only offer a slight increase in foil's efficiency. Therefore, the Reynolds number does not significantly impact the energy harvesting from such turbines and this is explained by the highly detached flow around flapping foils, which is caused by the typical high angles of attack, characteristic of foils operating in an energy harvesting regime.

Chapters 4 and 5 investigate the wake between two tandem foils in different perspectives. A wake analysis is first performed and a relationship between the mean wake velocity and the turbulent kinetic energy is obtained for a wide range of foil kinematics. With these two quantities, an updated trailing foil efficiency based on the wake rather than the freestream is developed and higher efficiency values are found, which emphasizes the importance of considering the unsteady flow effects in the wake when analyzing downstream foil's performance. After an in-depth wake analysis, the goal of identifying wake patterns among different foil kinematics is performed through classification and clustering models. The combination of both models gave rise to four wake patterns where each pattern is associated

with a range of foil kinematics. Through this connection between leading foil kinematics and the respective wakes, a prediction model for the trailing foil performance based on leading foil kinematics is described in chapter 6.

Chapter 6 describes a prediction methodology based on quantifying the effects of vortex gusts on the effective angle of attack and heave power on the trailing foil in a two-foil array. The unsteady contributions of the wake disturbances on the trailing foil are characterized as the difference of both heave power and angle of attack when compared to those from a reference foil state, defined here as a state where the oncoming flow velocity is set to be the mean wake velocity. It is found that when comparing the predicted power from the trailing foil with the output from the numerical simulation, similar trends are obtained. This model builds the foundation for an optimization algorithm for energy harvesting in foil-arrays since it only requires data from single-foil simulations.

Although this prediction model is performed using data from 2D simulations with uniform freestream, it is still relevant to arrays in 3D configurations and freestream turbulence. The major difference would be adding a power factor to the prediction caused by the tip effects, which are now considered in a 3D setup and can modify the pressure gradient around a foil as vorticity leaks at the foil tips. The freestream turbulence impacts the formation and strength of the vortices over the foil but since the model only requires measurements of the effective angle of attack, the impact of the freestream turbulence are incorporated into the model and no futher adjustments are required.

Bibliography

[1] Wind and Water Power Program, *Marine and Hydrokinetic Energy Projects*. U.S. Department of Energy-Office of Energy Efficiency and Renewable Energy, 2012. Technical Report DOE/EE-0710.

[2] A. Gorlov, *Development of the Helical Reaction Hydraulic Turbine*. U.S. Department of Energy, 1998. Technical Report DOE/EE/15669-T1.

[3] N. D. Laws and B. P. Epps, "Hydrokinetic energy conversion: Technology, research, and outlook," *Renewable and Sustainable Energy Reviews*, vol. 57, pp. 1245–1259, May 2016.

[4] M. Miller, *Fluid Dynamic Research and Prototype Development of the Leading Edge Oscillating Hydrofoil for Hydrokinetic Energy Harvesting*. (Ph.D. thesis), Brown University, 2019.

[5] X. Wu, X. Zhang, X. Tian, X. Li, and W. Lu, "A review on fluid dynamics of flapping foils," *Ocean Engineering*, vol. 195, p. 106712, 2020.

[6] W. McKinney and J. DeLaurier, "Wingmill: An oscillating-wing windmill," *J. Energy*, vol. 5, no. 2, pp. 109–115, 1981.

[7] J. Young, J. Lai, and M. Platzer, "A review of progress and challenges in flapping foil power generation," *Prog. Aerosp. Sci.*, vol. 67, no. 1, pp. 2–28, 2014.

[8] Q. Xiao and Q. Zhu, "A review on flow energy harvesters based on flapping foils," *J. Fluids Struct.*, vol. 46, pp. 174–191, 2014.

[9] N. D. Laws and B. P. Epps, "Hydrokinetic energy conversion: Technology, research, and outlook," *Renewable and Sustainable Energy Reviews*, vol. 57, May 2016.

[10] W. Liu, Q. Xiao, and F. Cheng, "A bio-inspired study on tidal energy extraction with flexible flapping wings," *Bioinspir. Biomim.*, vol. 8, no. 3, 2013.

[11] Y. Su, *Energy Harvesting and Aeroelastic Instabilities Using Prescribed and Elastically-Mounted Pitching and Heaving Hydrofoils*. (Ph.D. thesis), Brown University, 2019.

[12] B. J. Simpson, S. Licht, F. S. Hover, and M. S. Triantafyllou, "Energy extraction through flapping foils," in *ASME 27th International Conference on Offshore Mechanics and Arctic Engineering. American Society of Mechanical Engineers*, (Estoril, Portugal), pp. 389–395, 2008.

[13] D. Kim, B. Strom, S. Mandre, and K. S. Breuer, "Energy harvesting performance and flow structure of an oscillating hydrofoil with finite span," *J. Fluids Struct.*, vol. 70, pp. 314–326, 2017.

[14] Y. Su, M. Miller, S. Mandre, and K. Breuer, "Confinement effects on energy harvesting by a heaving and pitching hydrofoil," *J. Fluids Struct.*, vol. 84, pp. 233–242, 2019.

[15] T. Kinsey, G. Dumas, G. Lalande, J. Ruel, A. Méhut, P. Viarouge, J. Lemay, and Y. Jean, "Prototype testing of a hydrokinetic turbine based on oscillating hydrofoils," *Renew. Energy*, vol. 36, no. 6, pp. 1710–1718, 2011.

[16] J. L. Cardona, M. J. Miller, T. Derecktor, S. Winckler, K. Volkmann, A. Medina, S. Cowles, R. Lorick, K. S. Breuer, and S. Mandre, "Field testing of a 1 kw oscillating hydrofoil energy harvesting system," in *Marine Energy Technology Symposium*, (Washington D.C., USA), 2016.

[17] T. Kinsey and G. Dumas, "Parametric study of an oscillating airfoil in a power-extraction regime," *AIAA J.*, vol. 46, no. 6, pp. 1318–1330, 2008.

[18] Q. Zhu, "Optimal frequency for flow energy harvesting of a flapping foil," *J. Fluid Mech.*, vol. 675, pp. 495–517, 2011.

[19] J. Wu, Y. L. Chen, and N. Zhao, "Role of induced vortex interaction in a semi-active flapping foil based energy harvester," *Phys. Fluids*, vol. 27, no. 9, 2015.

[20] Y. Su and K. Breuer, "Resonant response and optimal energy harvesting of an elastically mounted pitching and heaving hydrofoil," *Phys. Rev. Fluids*, vol. 4, no. 6, 2019.

[21] Y. S. Baik, L. P. Bernal, K. Granlund, and M. V. Ol, "Unsteady force generation and vortex dynamics of pitching and plunging aerofoils," *J. Fluid Mech.*, vol. 709, pp. 37–68, 2012.

[22] L. Ding, L. Zhang, M. M. Bernitsas, and C.-C. Chang, "Numerical simulation and experimental validation for energy harvesting of single-cylinder vivace converter with passive turbulence control," *Renew. Energy J.*, vol. 85, pp. 1246–1259, 2015.

[23] F. Simeski, "Simulations of Hydrofoil Arrays with Applications in Energy Harvesting," (Bachelor's thesis), Brown University, 2017.

[24] K. D. Jones, K. Lindsey, and M. F. Platzer, "An investigation of the fluid-structure interaction in an oscillating-wing micro-hydropower generator," *WIT Transactions on the Built Environment*, vol. 71, pp. 73–82, 2003.

[25] Q. Zhu and Z. Peng, "Mode coupling and flow energy harvesting by a flapping foil," *Physics of Fluids*, vol. 21, p. 033601, Mar. 2009.

[26] J. Wu, Y. L. Qiu, C. Shu, and N. Zhao, "Pitching-motion-activated flapping foil near solid walls for power extraction: A numerical investigation," *Physics of Fluids*, vol. 26, no. 8, p. 083601, 2014.

[27] F. Karakas and I. Fenercioglu, "Effect of side-walls on flapping-wing power-generation: an experimental study," *Journal of Applied Fluid Mechanics*, vol. 9, pp. 2769–2779, 2016.

[28] Y. Su, M. Miller, S. Mandre, and K. Breuer, "Confinement effects on energy harvesting by a heaving and pitching hydrofoil," *Journal of Fluids and Structures*, vol. 84, pp. 233–242, 2019.

[29] T. Göçmen, P. V. D. Laan, P.-E. Réthoré, A. P. Diaz, G. C. Larsen, and S. Ott, "Wind turbine wake models developed at the technical university of Denmark: A review," *Renewable and Sustainable Energy Reviews*, vol. 60, pp. 752–769, 2016.

[30] R. Shakoor, M. Y. Hassan, A. Raheem, and Y.-K. Wu, "Wake effect modeling: A review of wind farm layout optimization using Jensen's model," *Renewable and Sustainable Energy Reviews*, vol. 58, pp. 1048–1059, 2016.

[31] M. Boudreau and G. Dumas, "Vortex dynamics in the wake of three generic types of freestream turbines," *Journal of Fluids Engineering*, vol. 140, no. 2, p. 021106, 2018.

[32] M. Platzer, M. Ashraf, J. Young, and J. Lai, "Development of a New Oscillating-Wing Wind and Hydropower Generator," in *47th AIAA Aerospace Sciences Meeting including The New Horizons Forum and Aerospace Exposition*, American Institute of Aeronautics and Astronautics, 2009.

[33] M. A. Ashraf, J. Young, J. C. S. Lai, and M. F. Platzer, "Numerical analysis of an oscillating-wing wind and hydropower generator," *AIAA J.*, vol. 49, no. 7, pp. 1374–1386, 2011.

[34] T. M. Broering and Y.-S. Lian, "The effect of phase angle and wing spacing on tandem flapping wings," *Acta Mechanica Sinica*, vol. 28, no. 6, pp. 1557–1571, 2012.

[35] T. M. Broering, Y.-S. Lian, and W. Henshaw, "Numerical Investigation of Energy Extraction in a Tandem Flapping Wing Configuration," *AIAA Journal*, vol. 50, no. 11, pp. 2295–2307, 2012.

[36] F. Karakas and I. Fenercioglu, "Effect of phase angle on tandem flapping-wing power generation," *International Journal of Energy Production and Management*, vol. 2, pp. 95–105, 2017.

[37] P. Ma, Y. Wang, Y. Xie, J. Han, G. Sun, and J. Zhang, "Effect of wake interaction on the response of two tandem oscillating hydrofoils," *Energy Science & Engineering*, vol. 7, no. 2, pp. 431–442, 2019.

[38] S. Ramananarivo, F. Fang, A. Oza, J. Zhang, and L. Ristroph, "Flow interactions lead to orderly formations of flapping wings in forward flight," *Physical Review Fluids*, vol. 1, p. 071201, 2016.

[39] J. W. Newbolt, J. Zhang, and L. Ristroph, "Flow interactions between uncoordinated flapping swimmers give rise to group cohesion," *Proceedings of the National Academy of Sciences*, vol. 116, pp. 2419–2424, 2019.

[40] C. H. K. Williamson and A. Roshko, "Vortex formation in the wake of an oscillating cylinder," *Journal of Fluids and Structures*, vol. 2, 1988.

[41] T. Schnipper, A. Andersen, and T. Bohr, "Vortex wakes of a flapping foil," *Journal of Fluid Mechanics*, vol. 633, Aug. 2009.

[42] M. M. Koochesfahani, "Vortical patterns in the wake of an oscillating airfoil," *AIAA Journal*, vol. 27, May 2012.

[43] J. C. S. Lai and M. F. Platzer, "Jet Characteristics of a Plunging Airfoil," *AIAA Journal*, vol. 37, 1999.

[44] B. L. R. Ribeiro, S. L. Frank, and J. A. Franck, "Vortex dynamics and Reynolds number effects of an oscillating hydrofoil in energy harvesting mode," *Journal of Fluids and Structures*, vol. 94, p. 102888, 2020.

[45] S. L. Brunton, B. R. Noack, and P. Koumoutsakos, "Machine Learning for Fluid Mechanics," *Annual Review of Fluid Mechanics*, vol. 52, 2020.

[46] S. Lee and D. You, "Data-driven prediction of unsteady flow over a circular cylinder using deep learning," *Journal of Fluid Mechanics*, vol. 879, 2019.

[47] S. Bhatnagar, Y. Afshar, S. Pan, K. Duraisamy, and S. Kaushik, "Prediction of aerodynamic flow fields using convolutional neural networks," *Computational Mechanics*, vol. 64, 2019.

[48] J. Hunt, A. Wray, and P. Moin, "Eddies, streams, and convergence zones in turbulent flows," in *Center for Turbulence Research: Proceeding of the Summer Program*, (Stanford), 1988. Report CTR-S88.

[49] J. Jeong and F. Hussain, "On the identification of a vortex," *Journal of Fluid Mechanics*, vol. 285, Feb. 1995.

[50] L. Deng, Y. Wang, Y. Liu, F. Wang, S. Li, and J. Liu, "A CNN-based vortex identification method," *Journal of Visualization*, vol. 22, 2019.

[51] A. G. Calvet, M. Dave, and J. A. Franck, "Unsupervised clustering and performance prediction of vortex wakes from bio-inspired propulsors," *Bioinspiration & Biomimetics*, vol. 16, 2021.

[52] B. Kashir, M. Ragone, A. Ramasubramanian, V. Yurkiv, and F. Mashayek, "Application of fully convolutional neural networks for feature extraction in fluid flow," *Journal of Visualization*, 2021.

[53] M. Morimoto, K. Fukami, K. Zhang, A. G. Nair, and K. Fukagata, "Convolutional neural networks for fluid flow analysis: toward effective metamodeling and low-dimensionalization," *arXiv preprint arXiv:2101.02535* [*physics*], 2021.

[54] S. Hochreiter and J. Schmidhuber, "Long Short-Term Memory," *Neural Computation*, vol. 9, 1997.

[55] R. Han, Y. Wang, Y. Zhang, and G. Chen, "A novel spatial-temporal prediction method for unsteady wake flows based on hybrid deep neural network," *Physics of Fluids*, vol. 31, Dec. 2019.

[56] T. Nakamura, K. Fukami, K. Hasegawa, Y. Nabae, and K. Fukagata, "Convolutional neural network and long short-term memory based reduced order surrogate for minimal turbulent channel flow," *Physics of Fluids*, vol. 33, 2021.

[57] J. Zhang and X. Zhao, "A novel dynamic wind farm wake model based on deep learning," *Applied Energy*, vol. 277, 2020.

[58] R. Issa, "Solution of the implicitly discretised fluid flow equations by operator-splitting," *Journal of Computational Physics*, vol. 62, no. 1, pp. 40–65, 1986.

[59] H. G. Weller, G. Tabor, H. Jasak, and C. Fureby, "A tensorial approach to computational continuum mechanics using object-oriented techniques," *Computers in Physics*, vol. 12, no. 6, pp. 620–631, 1998.

[60] A. A. Johnson and T. E. Tezduyar, "Mesh update strategies in parallel finite element computations of flow problems with moving boundaries and interfaces," *Computer Methods in Applied Mechanics and Engineering*, vol. 119, pp. 73–94, Nov. 1994.

[61] M. Dave, A. Spaulding, and J. A. Franck, "Variable thrust and high efficiency propulsion with oscillating foils at high Reynolds numbers," *Ocean Engineering*, vol. 214, p. 107833, 2020.

[62] C. Geuzaine and J.-F. Remacle, "Gmsh: A 3-D finite element mesh generator with built-in pre- and post-processing facilities," *International Journal for Numerical Methods in Engineering*, vol. 79, no. 11, pp. 1309–1331, 2009.

[63] Q. Xiao, W. Liao, S. Yang, and Y. Peng, "How motion trajectory affects energy extraction performance of a biomimic energy generator with an oscillating foil?," *Renew. Energy*, vol. 37, no. 1, pp. 61–75, 2012.

[64] T. Kinsey and G. Dumas, "Computational fluid dynamics analysis of a hydrokinetic turbine based on oscillating hydrofoils," *J. Fluids Eng.*, vol. 134, no. 2, 2012.

[65] M. S. Campobasso, A. Piskopakis, and M. Yan, "Analysis of an oscillating wing in a power-extraction regime based on the compressible reynolds-averaged navier-stokes equations and the k–ω SST turbulence model," in *ASME Turbo Expo: Turbine Technical Conference and Exposition. American Society of Mechanical Engineers*, (San Antonio, USA), 2013.

[66] J. A. Franck and T. Colonius, "A compressible large-Eddy simulation of separation control on a wall-mounted hump," *AIAA J.*, vol. 48, no. 6, pp. 1098–1107, 2010.

[67] D. Greenblatt, K. B. Paschal, C.-S. Yao, J. Harris, N. W. Schaeffler, and A. E. Washburn, "A separation control CFD validation test case, Part 1: baseline and steady suction," *AIAA J.*, vol. 2220, 2004.

[68] D. Rival, G. Hass, and C. Tropea, "Recovery of energy from leading- and trailing-edge vortices in tandem-airfoil configurations," *Journal of Aircraft*, vol. 48, no. 1, pp. 203–211, 2011.

[69] J. Xu, H. Sun, and S. Tan, "Wake vortex interaction effects on energy extraction performance of tandem oscillating hydrofoils," *Journal of Mechanical Science and Technology*, vol. 30, no. 9, pp. 4227–4237, 2016.

[70] A. Betz, *Windmills in the light of modern research*, vol. XV. National Advisory committee for aeronautics, 1928.

[71] B. G. Newman, "Multiple actuator-disc theory for wind turbines," *Journal of Wind Engineering and Industrial Aerodynamics*, vol. 24, no. 3, pp. 215–225, 1986.

[72] J. O. Dabiri, "Theoretical framework to surpass the Betz limit using unsteady fluid mechanics," *Physical Review Fluids*, vol. 5, no. 2, p. 022501, 2020.

[73] J. Young, F.-B. Tian, Z. Liu, J. C. S. Lai, N. Nadim, and A. D. Lucey, "Analysis of unsteady flow effects on the Betz limit for flapping foil power generation," *Journal of Fluid Mechanics*, vol. 902, p. A30, 2020.

[74] T. Kinsey and G. Dumas, "Optimal tandem configuration for oscillating-foils hydrokinetic turbine," *Journal of Fluids Engineering*, vol. 134, no. 3, p. 031103, 2012.

[75] B. Colvert, M. Alsalman, and E. Kanso, "Classifying vortex wakes using neural networks," *Bioinspiration & Biomimetics*, vol. 13, Feb. 2018.

[76] B. Pollard and P. Tallapragada, "Learning hydrodynamic signatures through proprioceptive sensing by bioinspired swimmers," *Bioinspiration & Biomimetics*, vol. 16, 2021.

[77] B. Li, Z. Yang, X. Zhang, G. He, B.-Q. Deng, and L. Shen, "Using machine learning to detect the turbulent region in flow past a circular cylinder," *Journal of Fluid Mechanics*, vol. 905, 2020.

[78] B. L. R. Ribeiro, Y. Su, Q. Guillaumin, K. S. Breuer, and J. A. Franck, "Wake-foil interactions and energy harvesting efficiency in tandem oscillating foils," *Phys. Rev. Fluids*, vol. 6, p. 074703, 2021.

[79] T. Kinsey and G. Dumas, "Optimal tandem configuration for oscillating-foils hydrokinetic turbine," *Journal of Fluids Engineering*, vol. 134, 2012.

[80] Y. S. Chong and Y. H. Tay, "Abnormal event detection in videos using spatiotemporal autoencoder," in *Advances in Neural Networks - ISNN 2017*, vol. 10262, Springer International Publishing, 2017.

[81] M. Abadi, A. Agarwal, P. Barham, E. Brevdo, Z. Chen, C. Citro, G. S. Corrado, A. Davis, J. Dean, M. Devin, S. Ghemawat, I. J. Goodfellow, A. Harp, G. Irving, M. Isard, Y. Jia, R. Józefowicz, L. Kaiser, M. Kudlur, J. Levenberg, D. Mané, R. Monga, S. Moore, D. G. Murray, C. Olah, M. Schuster, J. Shlens, B. Steiner, I. Sutskever, K. Talwar, P. A. Tucker, V. Vanhoucke, V. Vasudevan, F. B. Viégas, O. Vinyals, P. Warden, M. Wattenberg, M. Wicke, Y. Yu, and X. Zheng, "Tensorflow: Large-scale machine learning on heterogeneous distributed systems," *CoRR*, 2016. arXiv: abs/1603.04467.

[82] F. Chollet *et al.*, "Keras," 2015. Publisher: GitHub.

[83] D. P. Kingma and J. Ba, "Adam: A method for stochastic optimization," in *3rd International Conference on Learning Representations. ICLR 2015 - Conf. Track Proc*, dec 2015.

[84] L. Prechelt, "Automatic early stopping using cross validation: quantifying the criteria," *Neural Networks*, vol. 11, 1998.

[85] R. L. Thorndike, "Who belongs in the family?," *Psychometrika*, vol. 18, pp. 267–276, Dec. 1953.

[86] P. J. Rousseeuw, "Silhouettes: A graphical aid to the interpretation and validation of cluster analysis," *Journal of Computational and Applied Mathematics*, vol. 20, pp. 53–65, Nov. 1987.

[87] X. Wu, X. Zhang, X. Tian, X. Li, and W. Lu, "A review on fluid dynamics of flapping foils," *Ocean Engineering*, vol. 195, Jan. 2020.

[88] B. L. R. Ribeiro and J. A. Franck, "Contributions to Power Extraction in a Dual Oscillating Foil System," *American Institute of Aeronautics and Astronautics Aviation Forum*, June 2022.

[89] B. L. R. Ribeiro and J. A. Franck, "Vortex Dynamics and Reynolds Number Effects of an Oscillating Hydrofoil in Energy Harvesting Mode," *Journal of Fluids and Structures*, 2019.

[90] B. L. R. Ribeiro and J. A. Franck, "Machine Learning to Classify Vortex Wakes of Energy Harvesting Oscillating Foils," *AIAA Journal*, pp. 1–11, 2022.

[91] G. Xu and W. Xu, "Energy extraction of two flapping foils with tandem configurations and vortex interactions," *Engineering Analysis with Boundary Elements*, vol. 82, pp. 202–209, 2017.

[92] T. Kinsey, G. Dumas, G. Lalande, J. Ruel, A. Méhut, P. Viarouge, J. Lemay, and Y. Jean, "Prototype testing of a hydrokinetic turbine based on oscillating hydrofoils," *Renewable Energy*, vol. 36, June 2011.

[93] P. Oshkai, D. Iverson, W. Lee, and G. Dumas, "Reliability study of a fully-passive oscillating foil turbine operating in a periodically-perturbed inflow," *Journal of Fluids and Structures*, vol. 113, 2022.

[94] B. L. R. Ribeiro, Y. Su, Q. Guillaumin, K. S. Breuer, and J. A. Franck, "Wake-foil interactions and energy harvesting efficiency in tandem oscillating foils," *Phys. Rev. Fluids*, vol. 6, 2021.

[95] D. Peng and J. W. Gregory, "Vortex dynamics during blade-vortex interactions," *Physics of Fluids*, vol. 27, no. 5, p. 053104, 2015.

[96] C. J. Barnes and M. R. Visbal, "Counterclockwise Vortical-Gust/Airfoil Interactions at a Transitional Reynolds Number," *AIAA Journal*, vol. 56, no. 7, pp. 2540–2552, 2018.

[97] C. J. Barnes and M. R. Visbal, "Clockwise Vortical-Gust/Airfoil Interactions at a Transitional Reynolds Number," *AIAA Journal*, vol. 56, no. 10, pp. 3863–3874, 2018.

[98] H. Biler, G. Sedky, A. R. Jones, M. Saritas, and O. Cetiner, "Experimental Investigation of Transverse and Vortex Gust Encounters at Low Reynolds Numbers," *AIAA Journal*, vol. 59, no. 3, pp. 786–799, 2021.

[99] B. Turhan, Z. Wang, and I. Gursul, "Interaction of vortex streets with a downstream wing," *Physical Review Fluids*, vol. 7, no. 9, p. 094701, 2022.

[100] G. D. Xu, W. Y. Duan, and W. H. Xu, "The propulsion of two flapping foils with tandem configuration and vortex interactions," *Physics of Fluids*, vol. 29, no. 9, p. 097102, 2017.

[101] L. E. Muscutt, G. D. Weymouth, and B. Ganapathisubramani, "Performance augmentation mechanism of in-line tandem flapping foils," *Journal of Fluid Mechanics*, vol. 827, pp. 484–505, 2017.